Simulation of Flow in a Solid Fuel Ramjet Cavity

Charles R. Arnold

Thesis submitted to the Faculty of the
Virginia Polytechnic Institute and State University
in partial fulfillment of the requirements for the degree of

Master of Science
in
Aerospace Engineering

Luca Massa, Chair
Gregory Young
Christopher J. Roy

April 18, 2023
Blacksburg, Virginia

Keywords: Large Eddy Simulation, Flamelet, Acoustics, Solid Fueled Ramjet, Galerkin

Simulation of Flow in a Solid Fuel Ramjet Cavity

Charles R. Arnold

ABSTRACT

Cold flow inside a Solid Fueled Ramjet (SFRJ) is simulated using large eddy simulations (LES). A finite element method using a Discontinuous Galerkin bases has been implemented in the open-sourced multi-physics software SU2. Novel LES formulations of the fuel-gas boundary conditions and the heat release due to mixing are obtained using integration by parts over the discontinuous Galerkin bases. The Smagorisnki and wall-adapted sub-grid stress model for the scalar variance have been implemented and investigated in two-dimensions. Spectral Proper Orthogonal Decomposition is used to analyze CFD results to determine acoustic modes in the ramjet. Peak acoustic frequencies are compared between between numerical and experimental results. Comparisons are made between simulations performed with a 2D axisymmetric domain and full 3D domain.

Cold-flow LES simulations show that there are two dominant acoustic modes ($St \equiv f/f_0 = \{3, 18\}$) in the ramjet and their frequency appears to be invariant to the cavity configuration. The first peak corresponds to a longitudinal mode associated to the chamber fundamental oscillations (with length scale L_c). The second is characterized with radial fluctuations in the mixing chamber and features the maximum chamber radius of the ramjet as its scaling length. Mixed (radial and axial) modes in the intermediate frequency range reveal the effect of a slanted aft wall on the acoustics. Three-dimensional cold flow simulations predicted weak non-symmetric (azimuthal) modes.

Hot-flow simulations show a substantial increase in the mean chamber pressure with the

addition of the cavity, indicating that it enhances flame-holding in solid-fuel ramjets, in agreement with the experiments. The analysis of the ramjet acoustic modes shows the emergence of low frequency modes in the cavity cases, in agreement with the experiments. Using SPOD, these modes were associated with low frequency breathing of the recirculation region at the nozzle throat. Perturbations are localized in the throat region because of the Mach number pressure scaling. These modes do not seem to affect the pressure fluctuation and thus combustion in the chamber. Together with the emergence of low frequency vortical modes, the cavity supports a decrease in the high-wave number harmonics of the ramjet chamber acoustic mode. These fluctuations are supported by non-linear amplification of the fundamental mode, which is enhanced by the thermo-acoustic coupling.

Simulation of Flow in a Solid Fuel Ramjet Cavity

Charles R. Arnold

GENERAL AUDIENCE ABSTRACT

Novel propulsion designs, such as solid fuel ramjets, present the opportunity of optimizing cavity shapes using additive manufacturing and three-dimensional printing to improve fuel-air mixing and lowering the thermo-acoustic feedback. In this work a computational model for solid fuel ramjets is developed and applied to laboratory firing tests performed by Prof Young's group at the advanced propulsion laboratory at Virginia Tech. In order to capture the fine mixing scales a novel discretization of the reactive Navier-Stokes using discontinuous Galerkin bases is implemented in an open source CFD code popular with aerospace graduate students and researchers. Subgrid modelling is implemented to determine the effect of small scales on the PMMA combustion mechanism developed at Virginia Tech. Numerical methods are used to simulate the turbulent flow of air through an axisymmetric cavity.

I dedicate this thesis to my parents Madelynn and Bruce Arnold who have supported me in every step of my education, my mentor Ralph Amateis who has shared much spiritual and life wisdom with me over the years, and all my incredible friends who have been there for me in the good times and the bad.

Acknowledgments

I would like to express my deepest gratitude to Dr. Massa and Dr. Roy for sharing their knowledge in the world of numerical modeling and simulation of turbulence. Dr. Massa spent many late nights helping me to debug and optimize the many additions we made to the SU2 code. Many thanks also to Henry Pace who worked tirelessly with Spitfire and Cantera to collect the libraries used in the flamelet code. I am also grateful for Dr. Young and Dominic Gallego's many days of work gathering experimental data that made much of this work meaningful. This work was made possible by funding from the Office of Naval Research and Program Officer Dr. Eric Marineau.

Contents

List of Figures

List of Tables

Acronyms:

List of Abbreviations

AFFT Azimuthal Fast Fourier Transform

DG Discontinuous Galerkin

FEM Finite Element Method

SFRJ Solid Fueled Ramjet

SPOD Spectral Proper Orthogonal Decomposition

Chapter 1

Introduction

The main goal of this work is to improve the understanding of combustion and acoustics in solid fuel ramjets. To begin the path towards understanding the contributions of the burning walls, it must first be explained what a Solid Fuel Ramjet (SFRJ) is. A SFRJ is a simple propulsion system which ideally has no moving parts. Air (typically supersonic) enters the device through an inlet and is compressed via its own momentum to a low subsonic speed and high pressure. It then enters a combustion cavity where it reacts with a fuel stored as a solid. The hot gas is then expanded through a nozzle that ejects it at a far higher velocity than it entered the inlet at, thereby producing thrust. An example design for a SFRJ is depicted below in 6.10, with the inlet labeled as "1," the combustion chamber with grey fuel grain as "2.", and the nozzle as "3."

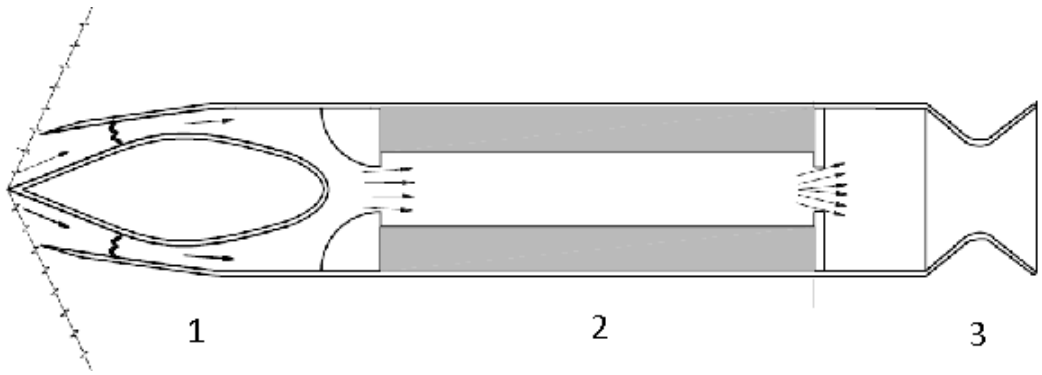

Figure 1.1: Schematic of basic SFRJ design. Figure adapted from "Propulsion control of a solid fuel ramjet using a robust adaptive neural controller"[1]

The SFRJ has the potential to offer a simple, compact, and storable propulsion system

without the need for a stored oxidizer. However, it faces engineering challenges in ensuring reliable flameholding and efficient combustion. This is due to the requirement that the fuel pyrolize, mix with the air, and complete the combustion process before being ejected out the nozzle. Meanwhile, the heat release must be such that the original surface is kept hot enough to continue the pyrolization process.

To avoid this issue, some designs replace the solid fuel grain with one or more gas generators that produce hot fuel-rich gas. This fuel-rich gas is injected into the airstream at a controlled rate where it is able to mix rapidly and finish combusting with the air. However, this design suffers from a weight and specific-impulse penalty from the oxidizer that must be contained in the gas generator. This also eliminates one of the safety advantages of the more traditional SFRJ design which is that a pure fuel grain combusts poorly or not at all without high-pressure airflow.

A 2020 paper in Doklady Physical Chemistry [2] analyzed the stability mechanisms for both of these types of ramjets for the purposes of creating a mathematical model for combustion stability in a particular ramjet design. The authors found that the most important factors for combustion stability are the temperature of combustion products within the flameholding region, the flow rate of products from this region, and the degree of turbulence within the solid fuel grain.

To allow reliable burning and efficient use of SFRJ fuel, there must be sufficient space inside the ramjet for the flow to mix and recirculate while the combustion process progresses. However, large cavities in the fuel grain reduce the amount of fuel that can be carried in a given volume, therefore it is important to minimize these. Additive manufacturing allows the creation of complex geometries for fuel grains which can allow recirculation and mixing to complete combustion while reducing dead space.

To determine appropriate fuel geometries and predict regression rates, a combination of numerical and experimental methods may be used. A 2017 article in Acta Astronautica investigated regression rates in a SFRJ and their correlations to geometry and air flow rates using RANS with a $k-\omega$ model with finite rate chemistry and found results to match to within 5-10% of experimental results. [3]

Recirculating and swirling flows can be useful for improving the combustion characteristics of fuel in a ramjet. A paper titled "Unsteady Simulation of Ignition of Turbulent Reactive Swirling Flow of Novel Design of Solid-Fuel Ramjet Motor"[4] analyzed the ignition and stabilization of combustion in a SFRJ design with and without swirling flow using a RANS (Reynolds Averaged Navier Stokes equations) solver with finite rate chemistry model. The numerical results, in agreement with experiment, showed that swirling flow improved mixing and residence time for combustion products, increased fuel regression rate, and reduced ignition time, all desirable for improving the performance of SFRJs.

Fuel grain geometry and the overall ramjet must also be designed to avoid or minimize combustion instabilities. Combustion instabilities can occur in high pressure combustion environments when acoustics couple with pressure sensitive combustion rates to create resonance in the combustion chamber. The effects of the resulting combustion and pressure fluctuation can range from rough running and efficiency losses to premature flameout or even violent destruction of the combustion chamber. [5]

Thermoacoustic combustion instabilities can be predicted numerically in a variety of ways, but generally the process involves the use of some form of unsteady computational fluid dynamics (CFD) simulation, typically using Unsteady Reynolds Averaged Navier Stokes (URANS) or Large Eddy Simulation (LES) with some method used to simulate or model combustion. The most general combustion capturing method is finite rate chemistry, which directly simulates the mixing and reaction of the various species involved in combustion

[6]. This method produces very detailed and accurate results, however the large number of reactions and species involved can make this prohibitive for 3D LES of a strongly turbulent flow. Alternatively, calculations may be simplified by using a model that captures the effects of combustion without tracking all of the species. This may be done by using a reduced-order finite rate chemistry model in which the number of species is reduced and related reactions are combined together. Another method is to take finite rate chemistry data is mapped to a space defined by a smaller number of variables. In this paper, a Flamelet Progress Variable (FPV) approach will be used, which uses tabulations of thermochemical properties as a function of local mixture fraction of fuel vs. air and reaction progress.[7]

One way to analyze acoustics in numerical simulations is through the use of a technique called Spectral Proper Orthogonal Decomposition, which separates acoustic signals in numerical results into different frequency modes, allowing the visualizations of acoustic structures in flows.[8] One 2022 paper by Li Weixuan, Zhao Dan, Zhang Linqing, and Chen Xiong investigated combustion instabilities in a SFRJ using a URANS solver for simulation and POD and Dynamic Mode Decomposition (DMD) (both relatives of SPOD) for analysis. [9]

In this thesis, a novel Discontinuous Galerkin (DG) method is used to apply the Large Eddy Simulation equations to A flamelet progress variable approach is developed for modeling of PMMA combustion and is implemented over the DG method in the open-source multiphysics solver SU2. Both hot and cold flows are run on a 2D axisymmetric grid and acoustic results are analyzed. For the hot flows, regression rate predictions are compared against those determined experimentally by Gallegos and Young [10].

Tests of computation time vs. number of computation nodes and processors are performed, and groundwork is laid for high-resolution 3D simulations of cold and hot flows to be performed and validated or invalidated against experimental results.

Chapter 2

Problem Formulation

In this chapter various aspects of the solvers and analysis methods used in numerical research of the ramjet will be listed. Further discussion of the numerical methods used in this research is included in subsequent sections highlighting portions of the two attached journal papers.

2.1 Governing Equations

The governing equations include mass, momentum, and energy conservation, plus the scalar continuity equations for all the additional combustion variables, i.e., Z the mixture fraction, C the progress variable, and Z'' the scalar variance. In the following equations the tilde superscript represents Favre-averaged (a form of density-weighted average) quantities and the bar superscript represents the Reynolds-averaged quantities. As standard with Einstein notation, summation is implied over repeated indices.

Continuity:

$$\frac{\partial \overline{\rho}}{\partial t} + \frac{\partial \overline{\rho}\widetilde{u_j}}{\partial x_j} = 0$$

Momentum:[7]

$$\frac{\partial \bar{\rho}\tilde{u}_i}{\partial t} + \frac{\partial \bar{\rho}\tilde{u}_i\tilde{u}_j}{\partial x_j} = -\frac{\partial \bar{p}}{\partial x_i} + 2\frac{\partial \bar{\mu}\tilde{S}_{ij}}{\partial x_j} + \frac{\partial \tau^r_{ij}}{\partial x_j}$$

$$\tilde{S}_{ij} = \frac{1}{2}(\frac{\partial \tilde{u}_i}{\partial x_j} + \frac{\partial \tilde{u}_j}{\partial x_i}) - \frac{1}{3}\delta_{ij}\frac{\partial \tilde{u}_k}{\partial x_k}$$

Mixture Fraction:

$$\frac{\partial \overline{\rho}\widetilde{Z}}{\partial x} + \frac{\partial \overline{\rho}\widetilde{u_j}\widetilde{Z}}{\partial x_j} = \frac{\partial}{\partial x_j}\left[\left(\overline{\rho}D + \frac{\mu_t}{Sc_t}\right)\frac{\partial \widetilde{Z}}{\partial x_j}\right]$$

Progress Variable:

$$\frac{\partial \overline{\rho}\widetilde{C}}{\partial t} + \frac{\partial \overline{\rho}\widetilde{u_j}\widetilde{C}}{\partial x_j} = \frac{\partial}{\partial x_j}\left[\left(\overline{\rho}D + \frac{\mu_t}{Sc_t}\right)\frac{\partial \widetilde{C}}{\partial x_j}\right] + \overline{\dot{\omega}}_c$$

Energy:

$$\begin{aligned}\frac{\partial \overline{\rho}\widetilde{E}}{\partial t} + \frac{\partial \overline{\rho}\widetilde{u_j}\widetilde{E}}{\partial x_j} = &\frac{\partial}{\partial x_j}\left[\left(\frac{\lambda}{c_p} + \frac{\mu_t}{\mathrm{Pr}_t}\right)\frac{\partial \widetilde{h}}{\partial x_j} + \sum_k\left(\overline{\rho}D_k - \frac{\lambda}{c_p}\right)\overline{h}_k\frac{\partial \widetilde{Y_k}}{\partial x_j}\right] \\ &+\frac{\partial}{\partial x_j}\left[-\widetilde{u}_j\overline{p} + \widetilde{u}_i\left(\overline{\tau}_{ij} - \overline{\rho}\widetilde{u_i''u_j''}\right)\right]\end{aligned}$$

where C is the progress variable, Z is the mixture fraction defined as $Z = \frac{\rho_f}{\rho_a+\rho_f}$, λ is the heat capacity of the air, D is the mass diffusivity, Sc_t is the turbulent Schmidt number, and μ is the dynamic viscosity. τ_{ij} is the residual turbulent stress. To account for the unresolved, small-scale eddies, stress is calculated using a sub-grid scale (SGS) model, discussed in section 5.1.

It should be noted that the mixture fraction evolution equation is devoid of chemical source terms by construction, since it is a linear combination of elemental mass fraction. However, its convection-diffusion transport equation involves a source term due to variation of the Lewis numbers among species and the Soret diffusion terms. Given that the Bilger mixture fraction is a linear combination of the species mass fractions $Z = \sum_i c_i Y_i$ and the diffusion flux of species i in the direction α are $J_{i\alpha}$, the right hand side of the convection-diffusion

transport equation for Z is

$$S \equiv -\frac{\partial}{\partial x_\alpha}\left(\rho D_{Z\alpha} \sum_i c_i \frac{\partial Y_i}{\partial x_\alpha} + \sum_i c_i \; J_{i\alpha} \right).$$

While it is impossible to zero-out the term S for any distribution of species mass fraction, it is possible to set the diffusivity such that

$$\rho D_{Z\alpha} \sum_i c_i \frac{\partial Y_i}{\partial x_\alpha} + \sum_i c_i \; J_{i\alpha} \; \equiv 0$$

for the flamelet one-dimensional solution. This procedure leads to the definition of the laminar diffusivity.

2.2 Weak Form

The procedure to obtain the weak formulation used in the finite element implementation of the Discontinuous Galerkin (DG) method is shown below for the scalar governing equations. The generic scalar conservation equation is

$$\frac{\partial \overline{\rho}\widetilde{\varphi}}{\partial t} + \frac{\partial \overline{\rho}\widetilde{u_j}\widetilde{\varphi}}{\partial x_j} = \frac{\partial}{\partial x_j}\left[\left(\overline{\rho} D + \frac{\mu_t}{Sc_t} \right) \frac{\partial \widetilde{\varphi}}{\partial x_j} \right] + \overline{\dot{\omega}}_\varphi$$

where $\overline{\dot{\omega}}_\varphi$ is the source term for the scalar. Integrating this equation and adding w as a weight function results in

$$\int_\Omega w \left\{ \frac{\partial \overline{\rho}\widetilde{\varphi}}{\partial t} + \frac{\partial \overline{\rho}\widetilde{u_j}\widetilde{\varphi}}{\partial x_j} \right\} \; d\Omega = \int_\Omega w \left\{ \frac{\partial}{\partial x_j}\left[\left(\overline{\rho} D + \frac{\mu_t}{Sc_t} \right) \frac{\partial \widetilde{\varphi}}{\partial x_j} \right] + \overline{\dot{\omega}}_\varphi \right\} \; d\Omega$$

Rewriting this using gradient and divergence instead of Einstein notation gives

$$\int_\Omega w \left\{ \frac{\partial \overline{\rho}\widetilde{\varphi}}{\partial t} + \nabla \bullet [\overline{\rho}\vec{u}\widetilde{\varphi}] \right\} \, d\Omega = \int_\Omega w \left\{ \overline{\dot{\omega}}_\varphi + \nabla \bullet \left[\left(\overline{\rho} D + \frac{\mu_t}{Sc_t} \right) \nabla \widetilde{\varphi} \right] \right\} \, d\Omega$$

Integration by parts and divergence theorem can then be applied to the divergence term.

$$\int_\Omega w \, \nabla \bullet [\overline{\rho}\vec{u}\widetilde{\varphi}] \, \, d\Omega = \int_\Gamma w \, [\overline{\rho}\vec{u}\widetilde{\varphi}] \bullet \vec{n} \, \, d\Gamma - \int_\Omega \nabla w \bullet [\overline{\rho}\vec{u}\widetilde{\varphi}] \, \, d\Omega$$

$$\int_\Omega w \, \nabla \bullet \left[\left(\overline{\rho} D + \frac{\mu_t}{Sc_t} \right) \nabla \widetilde{\varphi} \right] \, d\Omega = \int_\Gamma w \left[\left(\overline{\rho} D + \frac{\mu_t}{Sc_t} \right) \nabla \widetilde{\varphi} \right] \bullet \vec{n} \, \, d\Gamma - \int_\Omega \nabla w \bullet \left[\left(\overline{\rho} D + \frac{\mu_t}{Sc_t} \right) \nabla \widetilde{\varphi} \right] \, d\Omega$$

Finally the following equation set is obtained.

$$\begin{gathered} \int_\Omega w \frac{\partial \overline{\rho}\widetilde{\varphi}}{\partial t} \, d\Omega + \left\{ \int_\Gamma w \, [\overline{\rho}\vec{u}\widetilde{\varphi}] \bullet \vec{n} \, \, d\Gamma - \int_\Omega \nabla w \bullet [\overline{\rho}\vec{u}\widetilde{\varphi}] \, \, d\Omega \right\} = \\ \left\{ \int_\Gamma w \left[\left(\overline{\rho} D + \frac{\mu_t}{Sc_t} \right) \nabla \widetilde{\varphi} \right] \bullet \vec{n} \, \, d\Gamma - \int_\Omega \nabla w \bullet \left[\left(\overline{\rho} D + \frac{\mu_t}{Sc_t} \right) \nabla \widetilde{\varphi} \right] \, d\Omega \right\} \\ + \int_\Omega w \overline{\dot{\omega}}_\varphi \, d\Omega = 0 \end{gathered}$$

2.3 Discontinuous Galerkin Method

Computational Fluid Dynamics for the solid-fueled ramjet were run using the Large Eddy Simulation equations solved with a Discontinuous Galerkin Method.

Early during the research period, two primary sub-grid scale models were used, the Wale

and Smagorinsky models. Through testing, it was found that the Smagorinsky model[11] was less susceptible to divergence, therefore most results listed in this thesis were obtained using this model.

2.4 Inviscid Flux Terms

Calculations of the inviscid flux terms were implemented using the Roe Method. In the following section, "L" and "R" are used to refer to the left and right hand element solutions from the previous iteration. Pressure is calculated using the following equations

$$p = (\gamma - 1)((\rho e) - \frac{1}{2}(\overrightarrow{u} \cdot \overrightarrow{\rho u})) \tag{2.1}$$

Differences between values for the left and right solutions are calculated using the equations

$$\begin{Bmatrix} \Delta\rho \\ \overrightarrow{\Delta\rho u} \\ \Delta\rho e \end{Bmatrix} = \begin{Bmatrix} \rho_R - \rho_L \\ \overrightarrow{\rho u}_R - \overrightarrow{\rho u}_R \\ (\rho e)_R - (\rho e)_L \end{Bmatrix} \tag{2.2}$$

Enthalpy values are calculated as follows

$$h = (\rho e) + p \tag{2.3}$$

The average velocity is calculated from the left and right velocity solutions as

$$\overrightarrow{u}_{avg} = \frac{\sqrt{\rho_L}\overrightarrow{u}_L + \sqrt{\rho_R}\overrightarrow{u}_R}{\sqrt{\rho_L} + \sqrt{\rho_R}} \tag{2.4}$$

A value for kinetic energy based on this velocity is calculated as

$$\alpha_{avg} = \frac{1}{2}\|\overrightarrow{u}_{avg}\|^2 \tag{2.5}$$

$$a^2_{avg} = (\gamma - 1)|h_{avg} - \alpha_{avg}| \tag{2.6}$$

The average velocity of the fluid normal to the element face is given by

$$v_{n,avg} = \overrightarrow{u}_{avg} \cdot \overrightarrow{n} \tag{2.7}$$

The velocity of the grid normal to the element face is given by

$$u_{g,n} = \overrightarrow{u}_{g} \cdot \overrightarrow{n} \tag{2.8}$$

In typical burning conditions, $u_{g,n}$ represents the regression velocity of the fuel walls. In the present work the wall are kept fixed while solving for the detailed energy balance at the surface, which yields the instantaneous regression rate. This topic is explained in details in Chapter 4.

The average velocity of the fluid relative to the grid in the normal direction is calculated as

$$u_{n,avg} = v_{n,avg} - u_{g,n} \tag{2.9}$$

The magnitude of the eigenvalues are then calculated (note the absolute value brackets) as

$$\begin{Bmatrix} \lambda_1 \\ \lambda_2 \\ \lambda_3 \end{Bmatrix} = \begin{Bmatrix} |u_{n,avg} + a_{avg}| \\ |u_{n,avg} - a_{avg}| \\ |u_{n,avg}| \end{Bmatrix} \tag{2.10}$$

A series of abbreviation variables for common terms are defined as

$$B_1 = \frac{\lambda_1 + \lambda_2}{2} \tag{2.11}$$

$$B_2 = \frac{\lambda_1 - \lambda_2}{2} \tag{2.12}$$

$$B_3 = B_1 - \lambda_3 \tag{2.13}$$

$$B_4 = (\gamma - 1)(\alpha_{avg}\Delta\rho - \overrightarrow{u}_{avg} \cdot \overrightarrow{\Delta\rho u} + \Delta(\rho e)) \tag{2.14}$$

$$B_5 = \overrightarrow{n} \cdot \overrightarrow{\Delta\rho u} - v_{n_avg}\Delta\rho \tag{2.15}$$

$$B_6 = \frac{B_3 B_4}{a_{avg}^2} + \frac{B_2 B_5}{a_{avg}} \tag{2.16}$$

$$B_7 = \frac{B_2 B_4}{a_{avg}} + B_3 B_5 \tag{2.17}$$

The face-normal flow velocities relative to the element faces are then calculated

$$u_n = \overrightarrow{u} \cdot \overrightarrow{n} - u_{g,n}. \tag{2.18}$$

Finally, the fluxes are calculated as

$$f_\rho = \frac{A}{2}(u_{n,L}\rho_L u_{n,R}\rho_R + p_a \overrightarrow{n} - (\lambda_3 \overrightarrow{\Delta\rho u} + B_6 \overrightarrow{u}_{avg} + B_7 \overrightarrow{n})) \tag{2.19}$$

$$\overrightarrow{f}_{(\rho u)} = \frac{A}{2}(u_{n,L}\overrightarrow{\rho u}_L + u_{n,R}\overrightarrow{\rho u}_R + p_a \overrightarrow{n} - (\lambda_3 \overrightarrow{\Delta\rho u} + B_6 \overrightarrow{u}_a vg + B_7 \overrightarrow{n})) \tag{2.20}$$

$$f_{(\rho e)} = \frac{A}{2}((\rho e)_L u_{n,L} + (\rho e)_R u_{n,R} + p_L v_{n,L} + p_R v_{n,R} - (\lambda_3 \Delta(\rho e) + B_6 h_{avg} + B_7 v_{n,avg})) \quad (2.21)$$

where p_a is the sum of pressures from the left and right element solutions.

Code implementing these equations as well as those for viscous fluxes can be found in Appendix B.

Chapter 3

Analysis of Ramjet Cavity Pressure Losses

This chapter presents an analysis of entropy losses in the combustion chamber under cold flow conditions by monitoring the total pressure throughout the ramjet. This analysis was an important preliminary step since the reservoir total conditions ($P_{tot} = 1.308 \times 10^6$ Pa (189.7 psia) and $T_{tot} = 554$ K) and exhaustion to atmospheric pressure result in supersonic flow at the injector and subsequent overexpanded conditions within the cavity. Due to the high Mach No. flows and the series of area changes within the ramjet, substantial total pressure losses occur between the inlet and mixing chamber PCB locations. Therefore, a careful evaluation of the boundary conditions was necessary to ensure appropriate setup of numerical simulations. Known experimental conditions are reported in 3.2. The equations for quasi-one-dimensional flow used in this analysis are reported in 3.0.2.

Mass Flow Rate	0.211 kg/s	Assumed steady state, constant
Upstream orifice All areas		
Total Temperature	548 K	May need to assume a profile
Exit Nozzle	Atm pressure or choked	If choked, prob. under-expanded

Table 3.2: Certain and nearly certain conditions

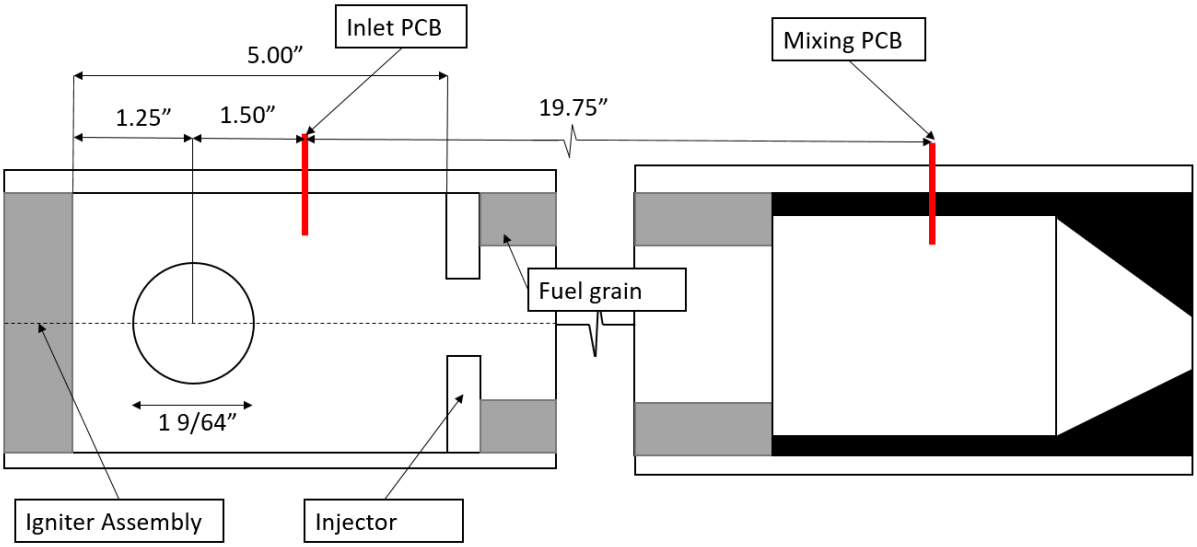

Figure 3.1: Schematic of the pressure probe locations used to determine the boundary conditions for the LES simulations.

A constant total pressure at the nozzle exit does not match the subsonic flow which was initially described, and results in a mass flow rate considerably greater than the experimental values. Therefore, we have considered the dimensions of an orifice far upstream, which the experimental team thought could be limiting the flow. Applying choked flow conditions (see calculations under ”Calc2” in Table 3.3) shows that sonic flow conditions through that orifice would still provide a higher mass flow rate than we had been given. To help further understand the flow conditions, we considered the locations of and data from the pressure transducers located in the ramjet. The data provided at the two gauge locations shown in Figure 3.1 is displayed in Figure 3.2.

The pressure value in the inlet chamber appeared unexpectedly low compared to the upstream total pressure of 1.308×10^6 Pa (189.7 psia). This prompted an early review of computational results. Under assumptions of adiabatic flow and mass conservation, the flow properties at this location were calculated. The indicated Mach number in the inlet cham-

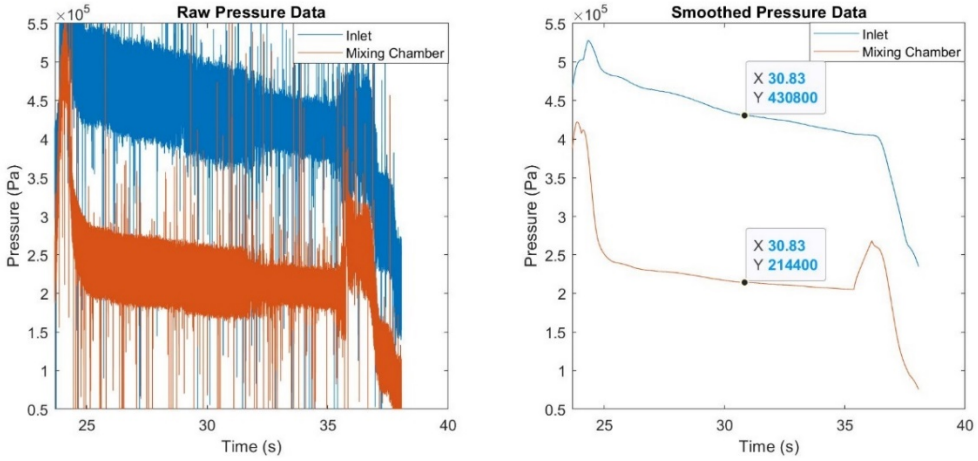

Figure 3.2: Raw and smoothed pressure time-series data, with example instantaneous pressure values.

ber is very low, resulting in the total pressure at the inlet chamber transducer being nearly identical to the static pressure, as seen in 3.3. Consequently, a large portion of the total pressure (approximately 8.6 bar or 125 psi) is lost between the upstream orifice and the inlet chamber just upstream of the injector. This is likely a result of shocks caused by the under-expanded low following the first contraction (see 3.1), as discussed further in the LES simulation sections. At the time of performing these calculations, this raised a question as to whether useful boundary conditions could be established at the ramjet inlet or the plumbing system upstream of the ramjet would need to be simulated as well.

Adiabatic flow calculations were continued for important points in the rest of the ramjet using both the given mass flow rate (see Table 3.3 Calc1) and the mass flow rate calculated from the orifice choking (see Table 3.3 Calc2). Calc3 and Calc4 showed consistent total pressure up until near the nozzle, but Calc1 and Calc2 had a different behavior.

Upon entrance to the mixing chamber, another significant reduction in total pressure occurs, which can be inferred since the static pressure is halved relative to that at the inlet chamber, despite the fact that the flow areas of the inlet and mixing chambers are identical and the flow

remains subsonic in the mixing chamber, having narrowly avoided choking at the injector. Calculations indicate that in the mixing chamber the total pressure is approximately 2.2 bar (31.9 psia), which represents a loss of about 83% (10.9 bar or 158 psi) from the original total pressure at the upstream orifice.

Before this point, both Calc1 and Calc2 calculations are valid, but comparison of the area of the injector to that required to choke the flow reveals that the injector area is too small to permit the flow based on Calc2's assumptions to pass. Therefore, the numbers in that column are no longer valid. Calc1 calculations remain valid under the assumption that the upstream orifice remains unchoked.

For the purpose of these calculations, it can be expected that the flow at the exit of the converging nozzle is to be subsonic. This condition along with atmospheric static pressure enables the calculation of total pressure at that location, which is estimated to be 1.5 bar (21.8 psia).

3.0.1 Further Boundary Conditions Analysis

Additional calculations were made by assuming the given mass flow rate is correct, assuming total temperature is constant through the ramjet, and calculating (initial) total pressure from choking at the upstream orifice. Calculating initial total pressure this way results in a significantly lower value than the one given: just 7.93 bar (115 psia) instead of 13.1 bar (190 psia). This lower total pressure allows *theoretically* no pressure loss up until the end of the mixing chamber. However, at the nozzle, the model is seen to break down.

For Calc3, the flow is assumed to lose no total pressure, and accelerate only as much as is dictated by the change in total area. This results the flow being subsonic at the exit and well above atmospheric pressure at the exit, which clearly is a non-physical result. For Calc4,

var	Calc1	Calc2	Calc3	Calc4
{'mdot (kg/s)' }	0.211	0.3481	0.211	0.211
{'P0 Orifice (bar)' }	13.08	13.08	7.93	7.93
{'T0 Orifice (K)' }	554	554	554	554
{'Orifice Mach No.' }	0.3825	1	1	1
{'P0 Inlet Chb (bar)' }	4.443	4.453	7.93	7.93
{'P0 lost Inlet Chb (%)'}	66.04	65.97	0	0
{'Inlet Chb Mach No.' }	0.04181	0.06896	0.0234	0.0234
{'Inj A/A*' }	1.031	0.626	1.839	1.839
{'P0 Mix Chb (bar)' }	2.187	2.206	7.93	7.93
{'P0 lost Mix Chb (%)' }	83.28	83.14	0	0
{'Mix Chb Mach No.' }	0.08522	0.1404	0.0234	0.0234
{'P0 Noz Tht (bar)' }	1.506	2.435	7.93	1.435
{'P Noz Tht (bar)' }	1.013	1.013	7.869	0.7581
{'Noz Tht Mach No.' }	0.7745	1.193	0.105	1

Table 3.3: Results of the quasi-1D analysis (Calc1 and Calc2 with experimental static pressure from Figure 3.2, Calc3 and Calc4 described in Section 3.0.1)

the flow is assumed to be choked at the exit and total and static pressure are calculated to maintain the inlet flow-rate. This results in the exit pressure being significantly below atmospheric. In certain situations, a nozzle exit pressure difference similar this can be maintained, but the nozzle usually must be carefully designed for it and have an exit Mach No. significantly greater than 1 (ex: RS-25). It is also unlikely that all total pressure losses occur in the nozzle alone.

In conclusion the analysis of the pressure losses in the combustion chamber leads to the four possible scenarios illustrated in Table 3.3. We have chosen the conditions of Calc 1 for the present analysis. As a verification of the approach, we monitor the mass flow rate the LES simulations described below and obtain an accurate mass flow rate vis-a-vis the mass flow rate reported in Table 3.2.

3.0.2 Equations for Quasi-Onedimensional Flow in the Solid Fuel Ramjet

Variables in the following equations are defined as such that $\dot{m}$ = mass flow rate, A = cross-sectional area. u = flow velocity, M = Mach No., γ = ratio of specific heats, R_s is the specific gas constant, T and T_0 are the static and total temperatures respectively, and similar for P with pressure and ρ with density.

$$\dot{m} = Au\rho, \quad u = M\sqrt{\gamma R_s T}, \quad \rho = \frac{P}{R_s T}, \quad \frac{T_0}{T} = 1 + \frac{\gamma - 1}{2}M^2$$

By combining the above classic ideal gas equations together, the following equation is obtained that gives mass flow rate in terms of the cross-sectional area, static pressure, Mach number, ratio of specific heats, specific gas constant, and total temperature.

$$\dot{m} = APM\sqrt{\frac{\gamma}{R_s T_0}\left(1 + \frac{\gamma - 1}{2}M^2\right)}$$

With one equation and one unknown (M), it is possibleto solve for Mach number either directly with numerical methods or analytically by rearranging the equation to be a quadratic function of M^2 and applying the quadratic formula (discarding the imaginary Mach No. solution). This allows calculation of Mach No. (and in turn, total pressure) at locations where area, mass flow rate, total temperature, and static pressure are known.

$$0 = \frac{\gamma - 1}{2}\left(M^2\right)^2 + \left(M^2\right) - \frac{R_s T_0}{\gamma}\left(\frac{\dot{m}}{AP}\right)^2$$

$$M^2 = \frac{-1 + \sqrt{1 + 2R_s T_0 \frac{\gamma-1}{\gamma} \left(\frac{\dot{m}}{AP}\right)^2}}{\gamma - 1}$$

The mass flow rate at a choked orifice where the cross-section area and total properties are known is given by

$$\dot{m} = AP_0 \sqrt{\frac{\gamma}{R_s T_0} \left(\frac{2}{\gamma+1}\right)^{\frac{\gamma+1}{\gamma-1}}}$$

Finally, the Mach No. can be solved for numerically at any point where the mass flow rate, cross-sectional area, total pressure, and total temperature are known.

$$0 = \dot{m} - AP_0 M \sqrt{\frac{\gamma}{R_s T_0} \left(1 + \frac{\gamma-1}{2} M^2\right)^{\frac{\gamma+1}{1-\gamma}}}$$

Chapter 4

Regression Rate and Flame Structure in Solid Fuel Ramjet Combustion

In this chapter I describe the first investigation I performed using the LES code I described in the previous chapters, which focused on the effect of cavity shape on the regression rate in solid fuel ramjets. The results of this investigation have been submitted to the Journal of propulsion and Power which has been recently accepted for publication. The highlights of this research are the verification and validation of the numerical code which are summarized below. A much more detailed description of the comparison of Ramjet regression rates against the experiments is described in the attached paper.

4.1 Highlights

A verification of the discretization error of the governing conservation equations along with a validation of the constitutive models, including its relevant combustion parameters are discussed.

4.1.1 Verification

An analysis of numerical errors, including grid sensitivity, is conducted in accordance with AIAA policy. AIAA policy requires log-log plot of how some error measure decreases as the grid is refined (or equivalently, coarsened) and a comparison of the achieved order of convergence with the nominal convergence rate of your chosen numerical method.

The test case of a circle in a low Mach number cross flow is adapted from Chauhan and Massa [12] for the verification of the asymptotic order of convergence of the newly developed discontinuous Galerkin combustion solver. For such verification study, the Reynolds number was set to the value of 666 and the Mach number to the 0.05, using the freestream velocity, density, and the diameter as reference variables. The Sutherland's formula and the perfect gas assumption was used to evaluate the other parameters in the free stream. Four computational meshes with increasing spacing were generated imposing a uniform distribution of 10-nodes triangle elements with edge size h equal to $\Delta,\ 2\Delta,\ 4\Delta, 8\Delta, \text{and} 16\Delta$, where $\Delta \equiv D_{\text{cyl}}/100$ and D_{cyl} is the diameter of the cylinder. The meshes were generated using the GMSH tool developed by Geuzaine and Remacle [13], with the adaptation option turned off and both the maximum and minimum mesh sizes set to the same value. The finest mesh was also replicated with 15-nodes triangles, which support a spatial error asymptotically decreasing with the mesh spacing to the power five, in order to be used as reference solution for the evaluation of the error. Starting from uniform initial condition both reactive ad unreactive simulations are advanced of a non-dimensional time of 2000 before starting the verification analysis. The reactive solution was evaluated using a burning non-regressing fuel cylinder with the interface conditions described in in the attached paper and air free-stream with total temperature and pressure equal to 548 K and 1 atm, respectively. Because the Damkholer numbers depend on the dimensional value of the diameter, a dimensional length of 1/20 of an inch (0.00127 m) was assigned to the diameter in order to match the finest

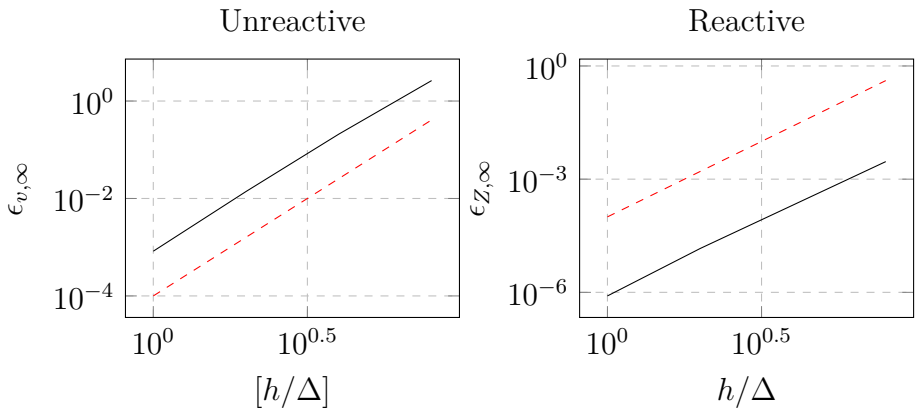

Figure 4.1: Convergence verification study using a fuel cylinder in air cross flow. Legend: — Actual; - - - Expected.

mesh size used in the numerical calculations of Ramjet combustion, $\Delta^* = 1/2000$ in or 1.27×10^{-5} m. The simulations were performed with the Discontinuous Galerkin method developed in this research and the fourth order classical Runge Kutta method. Using a CFL number equal to 0.3, which is the same as that used in the ramjet simulations, the order of accuracy the method is four as the mesh spacing is decreased towards zero. The fifth-order solution used as reference for the error calculations was evaluated with a CFL number of 0.1. Results of the verification analysis are shown in Figure 4.1 in terms of the L_∞ norm of the error. Here, the solid black line shows the actual error values and the dashed red line represents expected convergence results based on the nominal order of convergence of the scheme. The error for the unreactive simulation has been computed using the vertical velocity, because such variable is not affected by the inflow boundary conditions, which can introduce numerical error layers. The error for the reactive simulations has been calculated using the mass fraction Z. The verification results show that a fourth order method has been obtained for both cases.

A comparison of the level of details provided by fourth order numerical DG discretization and the second order equivalent using the same element structure is shown in Figure 4.2.

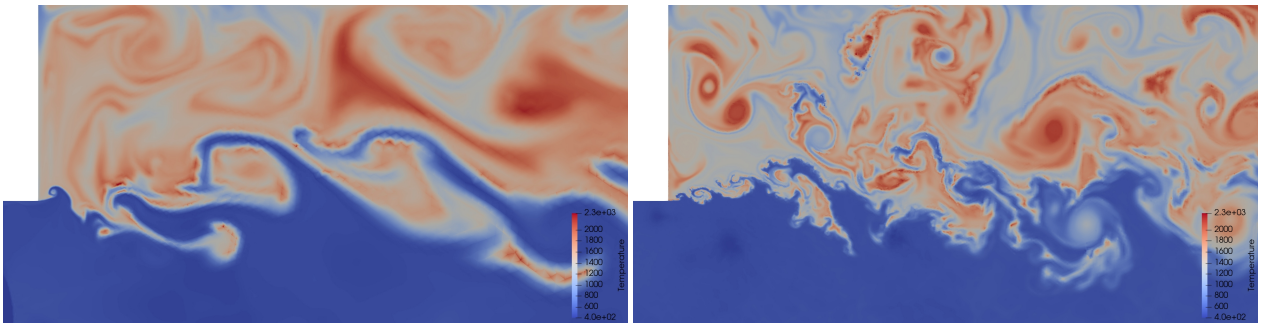

(a) Second order (b) Fourth order

Figure 4.2: Comparison of 2nd and fourth order discontinuous Galerkin simulation with LES code developed in this Thesis.

In this figure the reader can notice the much improved level of details that fourth order simulations provide without changing element number and structure.

4.1.2 Validation

This validation study aims at assessing the error of the combustion constitutive models by comparison against counterflow diffusion flames experiment over PMMA fuels carried out in the APPL combustion lab at Virginia Tech under the supervision of Professor Young. Results are shown in Figure 4.3 and compare the numerical predictions against lab-scale experiments. This investigation find an acceptable agreement for the new PMMA combustion model tested in this thesis.

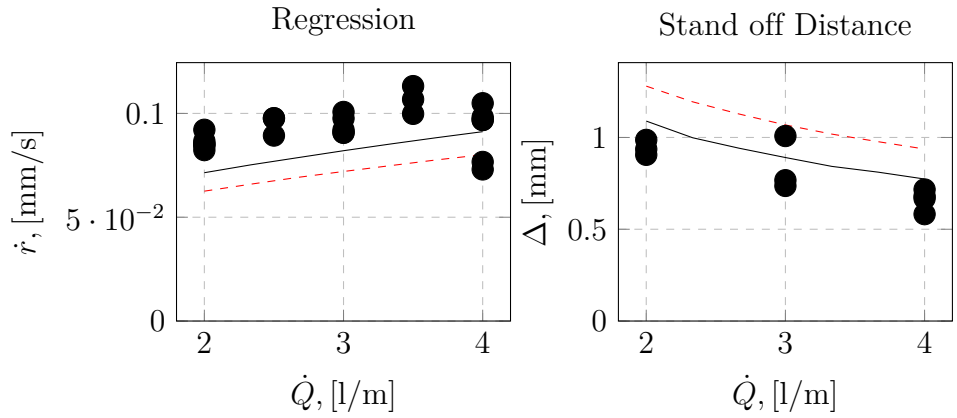

Figure 4.3: Validation of mechanism comparing the regression rate and flame standoff distance versus experiments. Legend: — Modified; - - - Original, • Measurements.

Regression and Flame Structure in Cavity Flameholding Solid Fuel Ramjet Fuel Grains

Dominic Gallegos *, Henry Pace†, Charles Arnold‡, Luca Massa§, and Gregory Young¶
Virginia Polytechnic Institute and State University, Blacksburg, Virginia 24060

Introducing cavity flameholders into a solid fuel ramjet fuel grain demonstrated increased fuel loading with sustained combustion in previously unfavorable geometries. Volumetric fuel loading improvements of up to 26% were demonstrated to sustain combustion. Regression patterns of cavity fuel grains are presented and show that the effect of introducing a cavity is to change the location of maximum regression and the reattachment point. The addition of a cavity flameholder does not appear to have a significant effect on combustion efficiency. However, it is noteworthy that longer cavities increased chamber pressure above what was observed for a center-perforated fuel grains as a result of the increased mass addition and higher equivalence ratio associated with the higher regression rate. LES computations were performed using a fourth order discontinuous Galerkin method solver with a novel flamelet and progress variable formulation. The predictions agree well with the experiments and point to the increased heat transfer for longer cavities as the main flame-holder mechanism. The larger heat feedback is supported by the formation of a stronger recirculation region, which leads to increased coherent fluctuations due to the transition between local and global instabilities.

Nomenclature

A	=	cross-sectional area
d	=	diameter
r	=	radius
h_{step}	=	step height
L_{caivty}	=	length of cavity flameholder
n	=	number of species
N	=	number of scalars

*Graduate Student, Aerospace and Ocean Engineering, 215 Randolph Hall, AIAA student member
†Graduate Student, Aerospace and Ocean Engineering, 215 Randolph Hall, AIAA student member
‡Graduate Student, Aerospace and Ocean Engineering, 215 Randolph Hall, AIAA student member
§Associate Professor, Aerospace and Ocean Engineering, 215 Randolph Hall, AIAA senior member
¶Associate Professor, Aerospace and Ocean Engineering, 215 Randolph Hall, AIAA senior member, corresponding author: gyoung1199@vt.edu

$\dot{r}$ = regression rate

T_g = gas temperature

q = heat flux

G_a = air mass flux

p = pressure

T = temperature

x/L = non-dimensional length

C^* = characteristic exhaust velocity

Subscripts

$_p$ = fuel grain port

$_{in}$ = inlet

$_t$ = throat

I. Introduction

Solid fuel ramjets (SFRJs) offer advantages over other means of propulsion utilizing ambient air through supersonic ram compression as the oxidizer that combusts with a solid fuel grain. As a result, the need to carry oxidizer and the turbomachinery/storage devices associated with liquid-fuel combustion propulsion is eliminated. To obtain stagnation temperatures and pressures to sustain combustion, solid and liquid fuel ramjets operate most efficiently while supersonic (≈Mach 2-6 for hydrocarbon fuels)[1]. As such, the traditional SFRJ is utilized in a booster-sustainer configuration wherein an alternate propulsive device (traditional solid rocket or ballistic device) carries the SFRJ to a supersonic velocity which can then ignite and sustain supersonic flight.

Practical implementation of SFRJs reveals a challenge in carrying an adequate fuel load while still providing the requisite geometry to sustain stable combustion. Solid fuel ramjets must maintain an adequate step height in the fuel grain (d_p/d_{in}) such that a low-velocity recirculation zone can be established, holding the flame and sustaining combustion. In a standard center-perforated fuel grain, this geometric region is created using a port diameter larger than the inlet diameter creating an effective step. However, this limits the amount of fuel that can be loaded into the combustor; as constant difference in diameters typically extend down the length of the fuel grain. Preceding research has focused on defining the critical area ratios between the relevant components in the SFRJ, namely the injector area (A_{in}), the fuel grain port area (A_p) and the nozzle throat area (A_t). Flammability limits have been well established for common hydrocarbon fuels such as polymethyl-methacryalte (PMMA), hydroxyl-terminated poly butadiene, and polyetheylene [2–7]. The common conclusion resulting from the prior studies is that sustained combustion is more favorable with increasing port-to-throat and port-to-inlet area ratios. Additionally, higher inlet temperatures are able to

support combustion at smaller area ratios and by further increasing the inlet temperature the criterion for autoignition of the fuel is met and the required step height is zero.

The primary considerations for flameholding is allowing enough residence time for the pyrolyized fuel to mix and combust within the recirulation zone prior to traveling downstream and providing the heat feedback to the surface to sustain combustion along the length of the fuel grain. In addition to changing the inlet, port, and nozzle diameters to affect the residence time, inlet swirlers have been investigated and shown to decrease the axial velocity component of the inlet. This has the effect of increasing the residence time within the recirculation zone in addition to promoting increased mixing of the inlet air and pyrolyzed fuel [8]. Experimental and numerical investigations of swirling inlets have demonstrated a decreased ignition time and improvements in average regression rates within a SFRJ [9, 10]. Though not in the context of flameholding, novel fuel port geometries have been investigated in the context of improving overall performance. In hybrid rockets, several alternate geometries were investigated and shown to increase combustion efficiency by promoting mixing within the fuel port [11].

The implementation of alternate fuel geometries in SFRJs for the purpose of improving flameholding or combustion efficiency has received little attention. However, solid fuel supersonic combustion ramjets (SFSJs) have demonstrated that sustained combustion at flight relevant conditions is only achievable using a cavity style flame holder [12]; that is an increased diameter portion immediately following a backwards facing step at the inlet. During the initial ignition phase the geometry provides a subsonic flow within the cavity flameholder such that the residence time of the pyrolyzed fuel is of the order of the chemical reaction timescale. The practical limitations and the motivation of determining the flammability limits for the SFSJ follow the same motivation as presented in this study, larger flameholder diameters promote flammability but limit the maximum fuel loading possible.

A traditional SFRJ flowfield is presented in figure 1. The flow separates after the injector plate and forms a shear layer separating the recriculation zone and the remainder of the flow. Within the recirculation zone, air from the inlet mixes with pyrolized fuel, combusts and is then carried downstream transferring thermal energy to the remainder of the fuel grain. The separated shear layer reattaches downstream of the step and at this location exhibits the highest regression rate for traditional center perforated fuel grains. Downstream of the reattachment point, a boundary layer develops and within it, a diffusion flame is established between the fuel rich region near the surface of the pyrolyzing fuel grain and the oxidizer-rich region of the air flow. Downstream of the fuel grain SFRJs are typically configured with a mixing chamber to increase the residence time of the fuel-air mixture and achieve satisfactory combustion efficiencies.

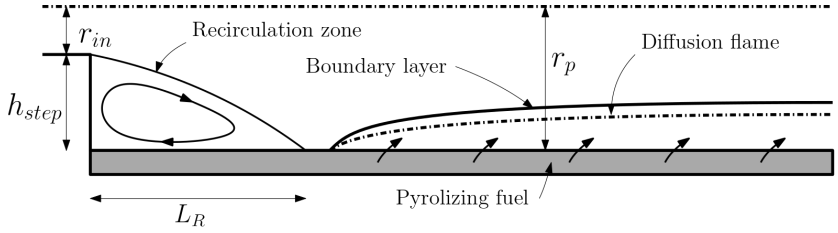

Fig. 1 Flowfield for a traditional, center-perforated SFRJ.

II. Experimental Setup

Figure 2 presents a schematic of the SFRJ test rig. High pressure air (≈1.3 MPa) was supplied to a 192kW electric heater, capable of heating the air to stagnation temperatures up to 923 K. Air was directed through an exhaust pipe during the heat-up phase or through the combustor for firing via two pneumatically actuated valves. Mass flow control was achieved via a choked flow orifice upstream of the combustor. The combustor comprises three sections (figure 3): the inlet section, the fuel grain, and the mixing chamber. The inlet section consists of two opposed air inlets and the igniter assembly, utilizing solid propellant and an electric match to ignite the fuel. The igniter assembly used approximately 7g of propellant per firing comprising 20% R45-IPDI binder, 70% ammonium perchlorate, and 10% aluminum. The inlet and fuel sections are separated by an injector plate with a smaller diameter hole than the fuel grain, creating the necessary step for flameholding. The fuel section utilizes fuels with nominal outside diameters of 90mm and 70mm and lengths up to 317mm long. For the cavity fuel grains investigated in this study, port diameters of 36mm, 37mm, 38mm and cavity diameters of 44mm and 48mm were investigated. In addition, port diameters ranging from 38mm to 61mm were investigated to establish the initial flammability limits. The mixing chamber allows increased residence time for the pyrolized fuel mixture, increasing the combustion efficiency. The products are then exhausted through the nozzle and out of the combustor. The fuel grains were epoxied into phenolic tubes for easy loading and unloading into the combustor. During the initial characterization of the combustor, both cast and 3D printed polymethylmethacrylate (PMMA) fuel grains were used. Printed PMMA fuel grains were prepared using a Raise3D Pro2 Plus FDM 3D printer using a 1mm nozzle. Cast fuel grains were prepared using commercially available PMMA rod and were drilled to the requisite diameter. To aid in ignition of the cast grains, the fuel was coated with a black spray paint and gunpowder mixture. This process was maintained through the firings of the cavity grains for consistency.

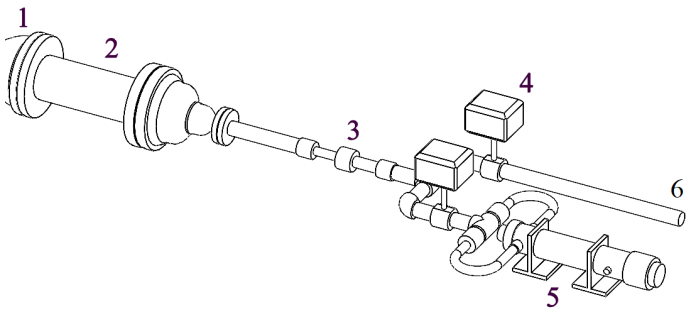

Fig. 2 Virginia Tech SFRJ: 1) Facility supplied, high pressure air 2) Electric air heater 3) Flow control orifice 4) Pneumatic flow control valves 5) SFRJ combustor 6) Exhaust pipeline

Instrumentation consisted of: static pressure transducers (Setra 206) at the orifice, inlet chamber and mixing chamber; K-type thermocouples at the orifice and inlet; and video to provide visual observation. To determine dominant frequency data for the cavities during combustion, a dynamic pressure transducer (PCB 113B26) was installed in the mixing chamber at the same axial location as the static pressure transducer. A typical test profile proceeds as follows: air flows through the exhaust until the heater reaches a steady, pre-selected temperature; the air control valves subsequently toggle position to begin flowing air through the combustor; the electric match/solid propellant is ignited to start the fuel combustion; steady combustion proceeds for 10-15 seconds; followed by a nitrogen purge to halt combustion. Figure 4 highlights a representative temperature and pressure history for a PMMA grain with a 44mm port diameter.

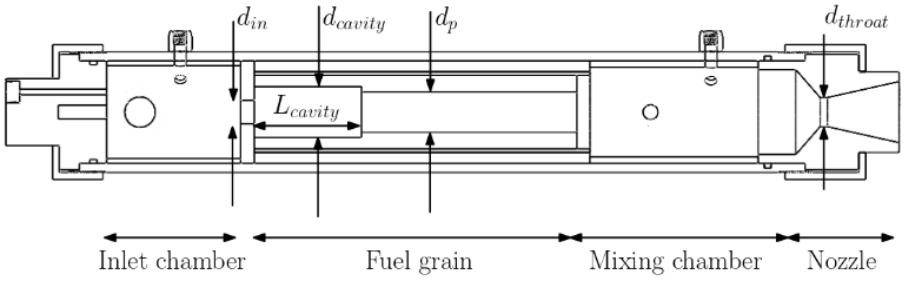

Fig. 3 Diagram of combustor sections and relevant dimensions.

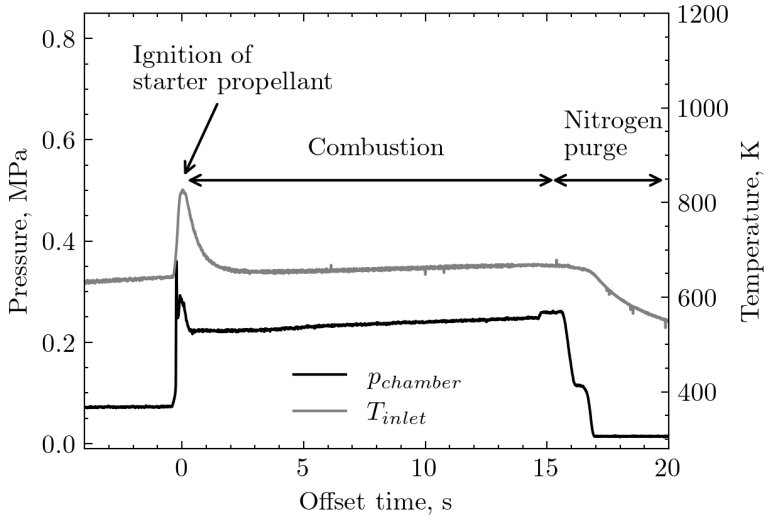

Fig. 4 Typical pressure and temperature history for a test.

III. Numerical Setup

Simulations of the ramjet propulsion system were performed using an in-house discontinuous Galerkin (DG) compressible Navier Stokes solver with flamelet and progress variable combustion. We have tested two subgrid scale models in the LES equations, the Smagorinsky and Wall Adapting Local Eddy Viscosity (WALE) formulations. The WALE model led to larger fluctuation in cold flow tests and a comparison against acoustic measurements suggested to select the Smagorinsky dynamic model for the computations reported here [13]. Compressibility is important because the throat and exit plane are choked. To reduce computational complexity, a 2D axisymmetric geometry was used for the results in this paper. Since the 2D axisymmetric geometry could not accommodate the opposing side inlet ports present in the experiment, flow was allowed to enter axially from the igniter face. To determine the magnitude of 3D effects, a 3D geometry with the opposing inlet ports was also tested. The magnitude of the non-axisymmetric azimuthal modes was found to be negligible and progressively decreasing with the mode number [13]. Overall, four different geometries were tested: a single 152mm cavity 3D geometry, 152mm and 51mm cavity axisymmetric 2D geometries, and finally a no-cavity axisymmetric 2D geometry.

Total conditions of 0.47 MPa and 548K were imposed at the inlet, and the exit was specified as an exhaust with atmospheric back-pressure. For improved accuracy at a given resolution, 3rd order finite element grids were used, constructed using the python API of GMSH [14], leading to a fourth-order accurate DG solution. For each 2D geometry three meshes with progressively smaller spacing were analyzed. The corresponding element numbers are 31,497, 90,450, and 141,155, respectively. All elements are 10 node triangles, Triangle-10. The smallest mesh edges for the coarse, medium, and fine grids are in order, 0.1016 mm, 0.0508 mm, and 0.02 mm. The smallest length scale of the mean flow affecting ramjet combustion is anticipated to be that of the PMMA-air diffusion flame, which the experiments

have shown to be approximately 1 mm. All computations discussed here were obtained with the finest grid.

A. Governing Equations

A novel discontinuous Galerkin Navier Stokes solver has been implemented to handle complex regressing geometries with coupled heat conduction. The solver is built on top of the SU2 framework [15].

The main drawback of flamelet and progress variable models in high-order discontinuous Galerkin methods is that unphysical pressure oscillations [16] can lead to elevate temperatures because temperature-induced dissociation is not included in flamelet linear mixing models. This is particularly important in ramjets where the throat is near chocked conditions and the supported shear layer over the recirculation region is in the compressible regime. Spurious pressure oscillations alter the acoustic response of the ramjet and prevent from obtaining the correct asymptotic order of convergence.

Momentum and mass continuity are identical to the unreactive case of Pierce and Moin [17] and are written in the mass filtered form:

$$\frac{\partial \bar{\rho}}{\partial t} + \boldsymbol{\nabla} \cdot \bar{\rho} \boldsymbol{u} = 0, \tag{1}$$

$$\frac{\partial \bar{\rho} \boldsymbol{u}}{\partial t} + \boldsymbol{\nabla} \cdot (\bar{\rho} \boldsymbol{u} \otimes \boldsymbol{u}) + \boldsymbol{\nabla} \bar{p} - \boldsymbol{\nabla} \cdot \bar{\sigma} = 0. \tag{2}$$

The energy equation is discretized starting from a conservative formulation in terms of the sensible energy and enthalpy written under the assumption of thermally perfect gases [18],

$$E_s \equiv \sum_{k=1}^{n_s} Y_k \int_0^T c_{v,k}\left(\tau\right) d\tau + \frac{1}{2} \boldsymbol{u} \cdot \boldsymbol{u}. \tag{3}$$

The thermal equation state for the mixture is written in terms of the mass fractions Y and the molar masses W using the ideal gas and Dalton laws

$$p = \rho R T \sum_{k=1}^{n_s} \frac{Y_k}{W_k}, \tag{4}$$

where $R = 8.3145$ J/mole − K is the universal gas constant.

LES averaging of the energy equation yields

$$\frac{\partial \bar{\rho} E_s}{\partial t} + \boldsymbol{\nabla} \cdot \left(\left(\bar{\rho} E_s + \bar{p}\right) \boldsymbol{u} - \left(\bar{\lambda} + \lambda_t\right) \boldsymbol{\nabla} T + \bar{\rho} \sum_{k=1}^{n_s} Y_k V_k h_{s,k} \right) - \boldsymbol{\nabla} \cdot \left(\bar{\sigma} \cdot \boldsymbol{u}\right) - \bar{\rho} \dot{\omega}_T = 0, \tag{5}$$

where the dissipative stress tensor has components $\bar{\sigma}_{ij} = 2\bar{\mu} S_{ij} + \tau_{ij}$, where $\overline{\overline{\boldsymbol{S}}} = 1/2 \left(\boldsymbol{\nabla} u + \boldsymbol{\nabla} u^T\right) - 1/3 \boldsymbol{\nabla} \cdot \boldsymbol{u} \overline{\overline{\boldsymbol{I}}}$. The subgrid scale tensor is evaluated using an eddy viscosity approach

$$\overline{\overline{\boldsymbol{\tau}}} = 2\mu_t \overline{\overline{\boldsymbol{S}}} - 1/3 \bar{\rho} q_t^2 \overline{\overline{\boldsymbol{I}}}. \tag{6}$$

The parameters of the eddy viscosity model (μ_t and q_t) are evaluated using either Smagorinsky's or WALE approaches. All variables are Favre-averaged with the exception of those marked with a bar overhead, to which Reynolds averaging is applied [19]. The heat release term in eq (5) is the product of the net volumetric production rates $\dot{\omega}_k$ and the heats of formation,

$$\dot{\omega}_T \equiv -\sum_{k=1}^{n_s} \dot{\omega}_k \Delta H^0_{fk}. \tag{7}$$

All variables dependent on the chemical state are evaluated using mixture rules where the chemical state is parameterized by scalars transported by the flow $\Psi_i,\ i = 1, \ldots, N_s$. They are: the (Bilger) mixture fraction $\Psi_1 = Z$ [20], the progress variable $\Psi_2 = Y_{CO_2}$, and the scalar dissipation $\Psi_3 = Z''$. The variance is approximated by the LES scaling law $\bar{\rho} Z'' \approx C_V \bar{\rho} \boldsymbol{\nabla} Z \cdot \boldsymbol{\nabla} Z$, with $C_V = 0.5$ [21]. The pressure is not included in the set of independent scalars as suggested, for example, by Nguyen and Sirignano [22] because we find it to be non-important to the evaluation of the cavity burning rates. The rationale is that the PDF is defined per unit density and the steady counterflow flame features an approximately linear variation of the mass rate of CO_2 production with the density. The main thermoacoustic feedback contribution in the present non-premixed flame is the heat released by the increased mixing due to the interaction of the pressure with the shear layer.

The differential equations for the evolution of the scalars are

$$\frac{\partial \bar{\rho} \Psi_i}{\partial t} + \boldsymbol{\nabla} \cdot (\bar{\rho} \boldsymbol{u} \Psi_i) - \boldsymbol{\nabla} \cdot \left(\left(\bar{\rho} D_{\Psi_i} + D_t \right) \boldsymbol{\nabla} \Psi_i \right) - \bar{\rho} \dot{\omega}_i = 0, \tag{8}$$

where the turbulent mass diffusivity coefficients are approximated with a constant Schmidt number $\bar{\rho} D_t = \mu_t / Sc_t$, $Sc_t = 1$.

In the flamelet and progress variable approaches there are twos ources of heating of the gas phase, which are expressed here as $\dot{\omega}_T = \dot{\omega}_P + \dot{\omega}_Z$. The first contribution is due to the progress and it is given here in terms of the net mass production rate of CO_2 $\dot{\omega}_{CO_2}$ in the flamelet solution.

$$\dot{\omega}_P = -\frac{RT_0}{\rho} \dot{\omega}_{CO_2} \sum_{k=1}^{n_s} \left(\frac{h_k}{RT_0} - 1 \right) \frac{\partial Y_k}{\partial \Psi_2} \Big/ \frac{\partial Y_{CO_2}}{\partial \Psi_2}. \tag{9}$$

The second contribution, the heat release due to a change in mixture fraction, is recasted in terms of the second derivative of the scalars. Then using integration by part we obtain the following source for the volumetric residual of the DG weak form

$$\dot{\omega}_Z = -\sum_{i=1}^{N_s} \left(D_t + D_{\Psi_i} \right) \left\{ \sum_{k=1}^{n_s} RT_0 \left(\frac{h_k}{RT_0} - 1 \right) \frac{\partial^2 Y_k}{\partial {\Psi_i}^2} \right\} \nabla \Psi_i \cdot \nabla \Psi_i, \tag{10}$$

All equations were converted to the weak integral form before discretizing them on the FEM mesh. The scalar conservation equation, for example, eq (8) is written below

$$\int_\Omega w \left\{ \frac{\partial \overline{\rho}\Psi_i}{\partial t} - \overline{\dot{\omega}}_b \right\} \, d\Omega + \int_\Gamma w \, [\overline{\rho}\vec{u}\Psi_i] \cdot \vec{n} \, d\Gamma - \int_\Omega \nabla w \cdot [\overline{\rho}\vec{u}\Psi_i] \, d\Omega$$
$$- \int_\Gamma w \left[\left(\overline{\rho} D + \frac{\mu_t}{Sc_t} \right) \nabla \Psi_i \right] \cdot \vec{n} \, d\Gamma + \int_\Omega \nabla w \cdot \left[\left(\overline{\rho} D + \frac{\mu_t}{Sc_t} \right) \nabla \Psi_i \right] \, d\Omega = 0, \quad (11)$$

where Ω is the volume of a domain (element), Γ is its surface (faces), w is a weighting function b is a general scalar, $\dot{\omega}_b$ is its source rate, D is the diffusivity of the scalar, μ_t is the eddy viscosity, and Sc_t is the turbulent Schmidt number. All terms in this equation are present for progress variable since it is a non-conserved variable. However, as a conserved variable, mixture fraction has a source rate of zero.

Numerical model parameters, such as the viscosity μ and the thermal conductivity λ, are evaluated using mixture rules, thus are functions of the scalar variables. The mixture average transport Wilke's formula [23] has been implemented. The thermal conductivity is evaluated using the following average that considers combination of parallel and serial heat transfers through layers of gas particles [24]

$$\bar{\lambda} = \frac{1}{2} \left(\sum_{k=1}^{n_s} X_k \lambda_k + \frac{1}{\sum_k X_k / \lambda_k} \right). \quad (12)$$

B. Combustion Model

The chemical mechanism was based on a 89 species and 627 reactions scheme appearing in previously published work [25], with several changes to the transport properties based on newly obtained results in computational chemistry as well as the added MMA condensed species. The flamelet and passive scalars models were implemented in a framework that facilitates the solution of multi-physics and multi-fidelity problems by interpolating the source terms for energy and mass exchange at the boundaries between solid and fluid zones.

This mechanism was implemented in Cantera [26] with few variations from the original formulation mainly regarding adjustments to the kinetic and transport properties of C3-C5 species as reflected by data published on the NIST and new rates estimated in the NUI mechanism [27]. The addition of new reactions was based on the sensitivity of kinetics parameters as found in counterflow experiments [28]. The entire mechanism is provided as supplementary material to this submission.

A mapping from a one dimensional, laminar counterflow diffusion flame into a manifold that can be used by the unsteady turbulent combustion simulation of a ramjet is performed using methodology similar to that presented by Pierce and Moin [17] and Oevermann [29]. A visual aid for the temperature as a thermochemical property of the independent variables can be seen in figure 5.

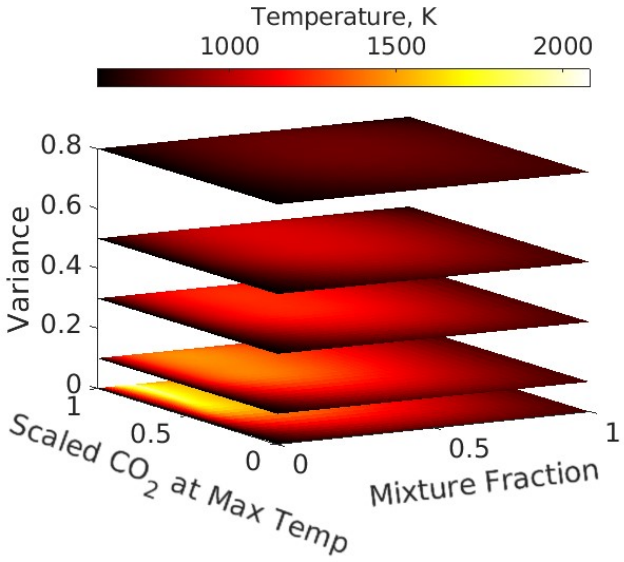

Fig. 5 Temperature distribution inside flamelet generated manifold for MMA

1. Solid-Gas Interface Conditions

The solid phase thermal decomposition of PMMA is calculated as a first order decomposition reaction [30] by solving the multiphase flow in the solid using a one-dimensional approach that includes bubble formation, evaporation, thermal decomposition, and momentum transfer between the liquid and gaseous phases in a foam layer [28]. The foam layer solution at void fraction equal to one is used to formulate the boundary conditions at the fuel surface in the LES simulations. Conservation of both the convective and diffusive fluxes at such interface and the assumption that species diffusion is not important in the foam layer [31], lead to expressing the regression rate and energy flux at the interface in terms of the conductive heat flux $q \equiv k\partial T/\partial n$ evaluated at the boundaries of the simulation domain. The wall regression model is clearly non-linear due to the variation of the surface temperature with the regression rate. The relationship between heat flux, regression rate, and surface temperature at the foam-gas interface is plotted in figure 6.

C. Verification

An analysis of the numerical errors is performed using a laminar test case because the introduction of mesh dependent modeling terms in LES prevents obtaining the asymptotic convergence rates. The test case of a cylinder in a low Mach number cross flow is adapted from Chauhan and Massa [32] for the verification of the asymptotic order of convergence of the newly developed discontinuous Galerkin combustion solver. For such verification study, the Reynolds number was set to the value of 666 and the Mach number to 0.05, using the freestream velocity, density, and the diameter as reference variables. The Sutherland's formula and the perfect gas assumption were used to evaluate the other parameters of the free stream. Four computational meshes with increasing spacing were generated imposing a uniform distribution

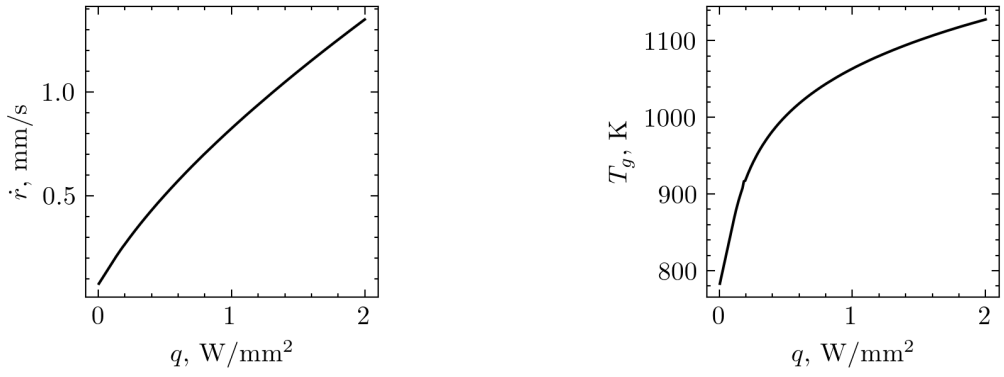

Fig. 6 Foam layer solid decomposition model: (a) fuel regression, (b) gas temperature.

of 10-nodes triangle elements with edge size h equal to $\Delta,\ 2\Delta,\ 4\Delta$, and 8Δ, where $\Delta \equiv D_{\text{cyl}}/50$ and D_{cyl} is the diameter of the cylinder. The meshes were generated using the GMSH tool developed by Geuzaine and Remacle [14], with the adaptation option turned off and both the maximum and minimum mesh sizes set to the same value. The finest mesh was also replicated with 15-nodes triangles, which support a spatial error asymptotically decreasing with the mesh spacing to the power fifth power. This simulation provided the reference solution for the evaluation of the error. Starting from uniform initial condition both reactive ad unreactive simulations are advanced of a non-dimensional time of 5 before starting the verification analysis. The reactive solution was evaluated using a burning non-regressing fuel cylinder with the interface conditions described in Section III.B.1 and air free-stream with total pressure and temperature and pressure equal to 548 K and 1 atm, respectively. Because the Damkholer numbers depend on the dimensional value of the diameter, a dimensional length of 1/20 of an inch (0.00127 m) was assigned to the diameter in order to match (approximately) the finest mesh size used in the numerical calculations of Ramjet combustion. The finest dimensional spacing used in this verification study is $\Delta^* = 1/1000$ in or 0.0254 mm. The simulations were performed with the discontinuous Galerkin method developed in this research and the fourth order classical Runge Kutta method. Using a CFL number equal to 0.3, which is the same as that used in the ramjet simulations, the convergence rate of the flow solver as the mesh spacing is decreased towards zero is four. The fifth-order solution used as reference for the error calculations was evaluated with a CFL number of 0.1. Results of the verification analysis are shown in figure 7 in terms of the L_∞ norm of the error (see Bonfiglioli and Paciorri [33] for the proper definition of the norm). Here, the solid black line shows the actual error values and the dashed red line represents expected convergence results based on the nominal order of convergence of the scheme. The error for the unreactive simulation has been computed using the vertical velocity, because such variable is not affected by the inflow boundary conditions, which was found to introduce numerical error layers when using uniformly spaced grids. The error for the reactive simulations has been calculated using the mass fraction Z. The verification results show that a fourth order method has been obtained for both cases.

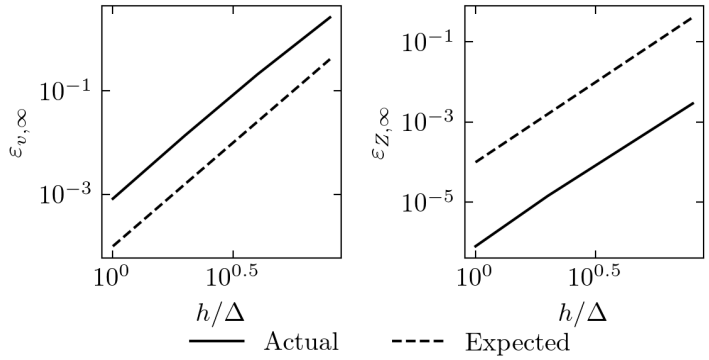

Fig. 7 Convergence verification study using a fuel cylinder in air cross flow.

IV. Results and Discussion

A. Experimental Results

1. Flammability Limits

The area ratios utilized in prior work [6] were used as a starting point to determine appropriate port-to-throat (A_p/A_t) and port-to-inlet (A_p/A_{in}) area ratios. Schulte demonstrated that different combustor sizes lead to different critical area ratios that will sustain combustion [2]. Therefore, the flammability limits should be determined as applied to the present configuration. A "go, no-go" criteria was applied via observation of sustained combustion following the combustion of the ignition material and a distinct pressure rise in the combustor. The selected air mass flow rate was approximately 250 g/s, allowing the maximum range of inlet air temperatures due to operational limits of the heater. Fuel grains with cavity flameholders were investigated at the 250 g/s flowrate, to establish initial flammability limits, a variety of geometries and temperatures were tested. Limited characterization of flammability limits at nominal flowrates of 160 g/s and 310 g/s were also conducted as shown in figure 8. It is noteworthy that the data point (A_p/A_t, A_p/A_{in}) = (1.6,1.8) for the printed fuel grains did not sustain combustion and will be used as the baseline for the investigation of cavity flameholders.

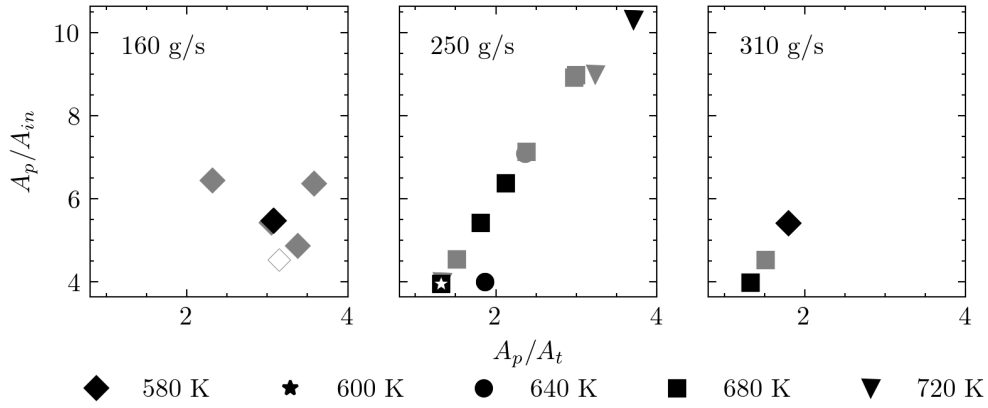

Fig. 8 Area ratio flammability limits. Filled symbols indicate sustained combustion configurations, black symbols indicate 3D printed fuel grains, gray symbols indicate cast fuel grains, symbol shape denotes temperature according to the figure legend.

The cavities investigated in this study are listed in table 1. The inlet diameter, nozzle throat diameter, and air mass flow rate were held constant within the cavity flameholder tests. The dimensions were selected according to the aformentioned flammability limits. The cavity diameter was defined using a port diameter that would sustain combustion, whereas the cavity fuel grain port diameter would not sustain combustion without the inclusion of the flameholder. The initial cavity dimensions were decreased within practical limits, attempting to determine the limit in which the addition of a cavity will not sustain combustion. For center-perforated fuel grain, a flammability limit was identified such that a grain with a port diameter of 38mm at the test conditions would not sustain combustion. Of the cavities investigated, all were able to sustain combustion despite decreasing the port diameter of the cavity grains below 38mm. The fuel grain containing the smallest cavity of those investigated (44-36-25) increased the volumetric fuel loading by 26% compared to the fuel grain with the smallest port that would sustain combustion.

Table 1 Summary of cavity grains investigated.

Grain Designation	Cavity diameter, mm	Port diameter, mm	Cavity length, mm
*Deep*cavity grains*			
48-38-152	48	38	152
48-38-102	48	38	102
48-38-51	48	38	51
48-38-38	48	38	38
48-38-25	48	38	25
48-38-13	48	38	13
Shallow cavity grains			
44-38-152	44	38	152
44-38-102	44	38	102
44-38-51	44	38	51
44-38-38	44	38	38
44-38-25	44	38	25
Small bore cavity grains			
44-37-25	44	37	25
44-36-25	44	36	25

2. Fuel Regression

Initial firings of the 3D printed PMMA grains showed significant variability and higher regression rates than the cast fuel grains. The initial grains, with measured densities around 80% of the theoretical density were used only for flammability studies. Upon improving the print densities to approximately 92% of the theoretical maximum density the regression rates are in better agreement with the cast grains used in the study (figure 9).

*The terms *deep* and *shallow* are used in a qualitative sense and do not correspond to the critical L/D ratios for defining shallow or deep cavities such as often done in cavity flow studies.

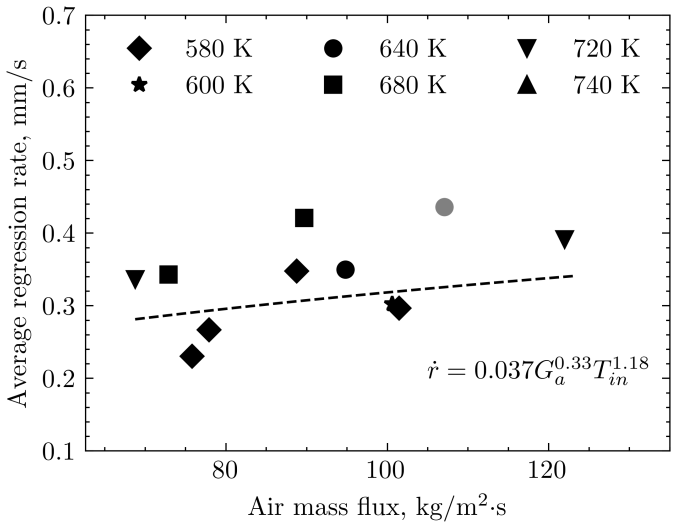

Fig. 9 Regression rates for cast PMMA grains. Improved density printed PMMA grain (grey marker) shown for comparison.

To analyze regression rate, the cavity grains of interest were first bisected and imaged to identify the regressed edges. Using the burn time for each test, a regression pattern at the time of the nitrogen purge can be determined. Figures 10 and 11 depict the regression patterns after a 12 second (±0.06 seconds) firing. The dashed profile in each figure represents the geometry before firing and the solid is the regressed surface pattern. The presented regression patterns are an average of the upper and lower surface regression distributions.

Figure 10 shows the regression patterns for the deep cavity grains. For the center-perforated fuel grain, the point of maximum regression is approximately at the reattachment point ($0.28 < x/L < 0.43$) in agreement with the work of [2]. By introducing a cavity, the point of maximum regression (and thus the reattachment point) shifts according to the length of the cavity. As expected for the case where the reattachment point is beyond the cavity length (48-38-25), the point of maximum regression does not coincide with the trailing edge cavity corner. The regression rate in the cavity itself for short cavity lengths is observed as small compared to the rest of the grain. Similar trends are observed in figure 11, which shows the regression profiles for the shallow cavity fuel grains. For both sets of grains, the addition of the cavity at the forward end of the grain appears to increase the regression in the aft, small diameter portion of the grain when compared to the center perforated fuel grain with a diameter equal to that of the cavity.

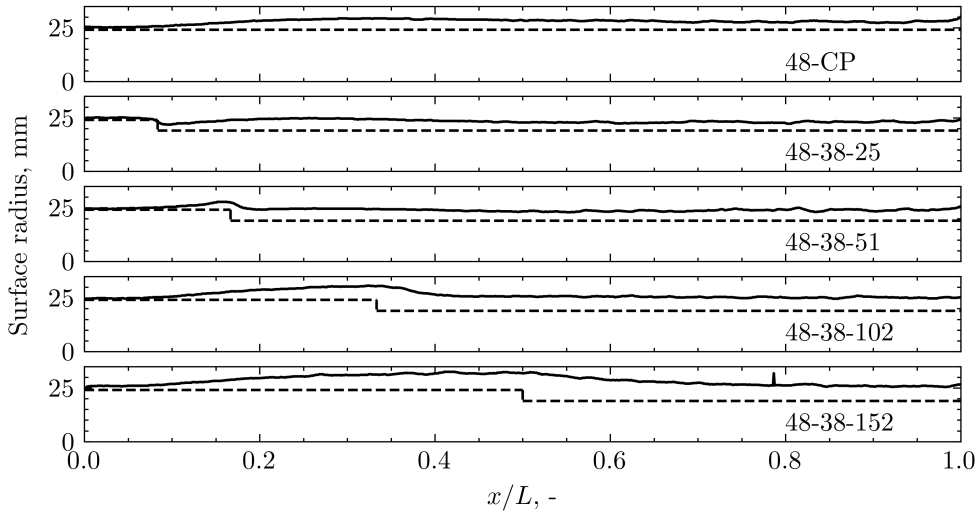

Fig. 10 Surface regression for 48mm diameter cavity fuel grains, flow is from left to right.

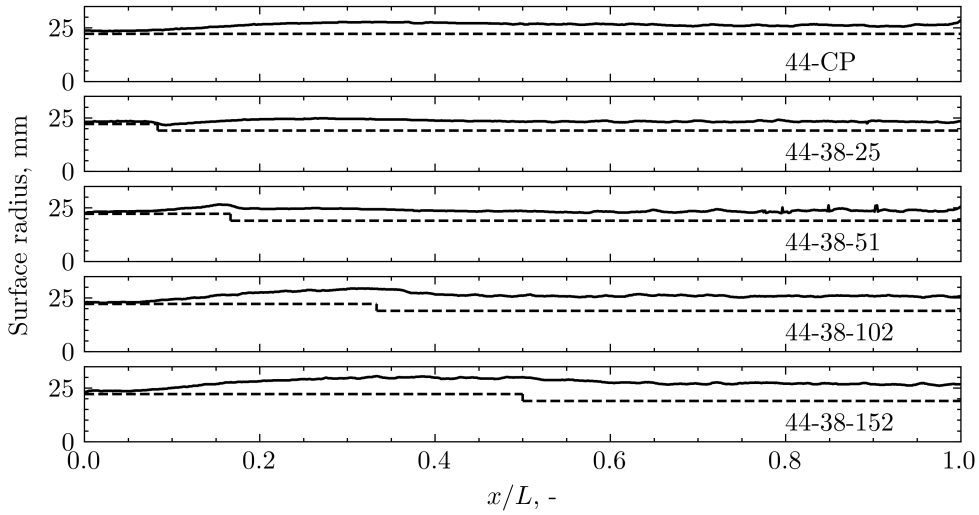

Fig. 11 Surface regression for 44mm diameter cavity fuel grains, flow is from left to right.

Regression rate data is typically presented as a spatially and temporally averaged value taking into account the burn time, mass loss, and average burning surface area through a firing. This is found to be primarily a function of air mass flux. Figure 12 presents the variation in average regression rates for each region within a cavity grain, the error bars represent the standard deviation of regression rate in the respective region. As shown in figures 10 and 11, the average regression rate within the cavity region is significantly lower than the port region of the fuel grain. Within the cavity region, the average regression rate appears to increase with increasing cavity length. The regression pattern for all of the geometries has a region of decreased regression immediately after the injector, as the cavity region is lengthened, this relatively constant length region becomes proportionally less of the cavity region and thus the average over the cavity

increases. As the cavity length increases, particularly as the cavity trailing edge approaches the reattachment point, the high regression region increases the average over the length of the cavity. Similar to the behavior in the cavity, the average regression in the port region also increases with cavity length.

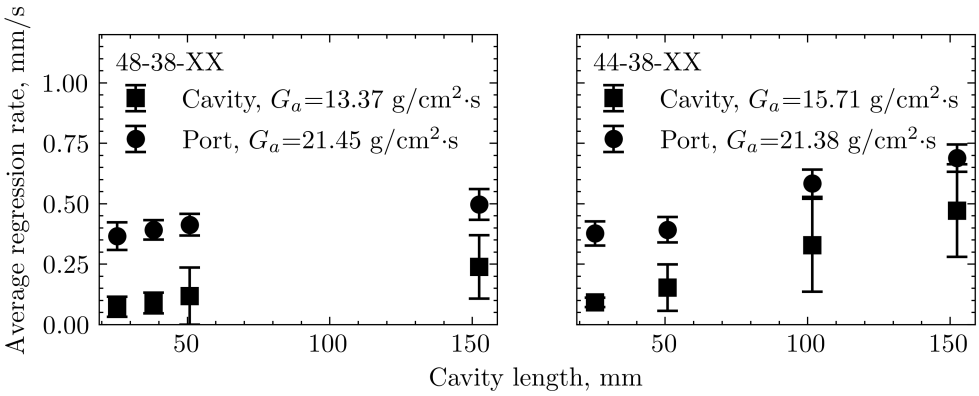

Fig. 12 Cavity and port average regression data as a function of cavity length.

3. Performance Characteristics

The characteristic exhaust velocity, C^*, was compared to the theoretical value as calculated from the chemical equilibrium code CEA [34, 35] using the average chamber pressure, air-to-fuel ratio and inlet temperature as seen in the firing. The variation of C^* for different fuel geometries is shown in figure 13 (error bars indicate propagation of error resultant from measurement uncertainties). C^* efficiency appears to be relatively insensitive to changes in cavity length. Chamber pressure is seen to increase approximately linearly with increases in cavity length. The chamber pressure with the longest cavity is seen to be above the chamber pressure for center perforated grain with a port diameter equal to the cavity diameter. The increase in regression rate in the port section of the cavity fuel grain contributes to a higher fuel mass flow rate. The higher fuel mass flow rate increase the equivalence ratio of the presently fuel-lean system towards the stoichiometric value (for the 48mm case the introduction of a 152mm cavity increases the equivalence ratio from 0.90 to 0.93). The combination of increased mass addition and higher flame temperature constitutes a rise in chamber pressure from the increased regression rate.

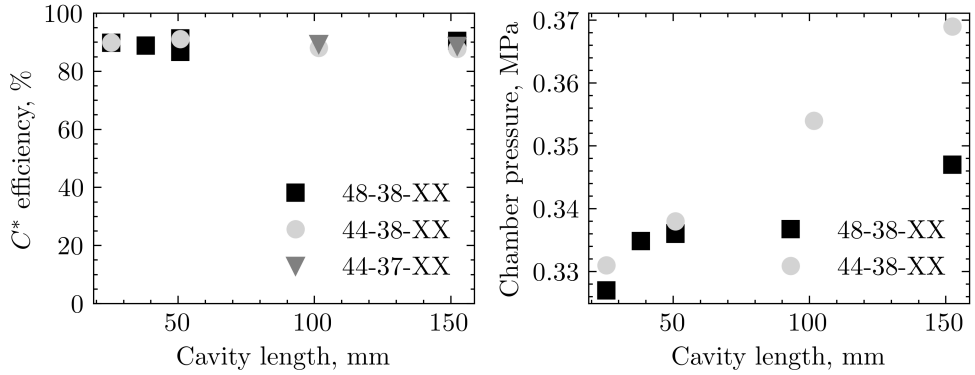

Fig. 13 Combustion efficiency and chamber pressure for various cavity configurations.

B. Numerical Results

Regression and Heat Flux

The regression rates are evaluated on the undeformed configuration by averaging the LES results over a period of time of 0.02 s.

Computed LES regression rates are compared to the measurements in figure 14 for the three shallow cavities. Significant unsteadiness occurs in the cavity and the coherent scales generated by the hydrodynamic instability are responsible for the majority of the heat flux to the fuel in the cavity. Convergence of the solution was analyzed by repeating the computations for the 152 mm shallow cavity over meshes with three element densities. Finer grid simulations lead to consistently reduced deviations from the experiments. The agreement between the model and the experiments is good for all three cases under investigation. The largest disagreement is at low values of x/L, where the computed heat flux increases much more rapidly than the measured analog. This is due to the inaccuracy of the Smagorinsky turbulence model in the transitional region [32].

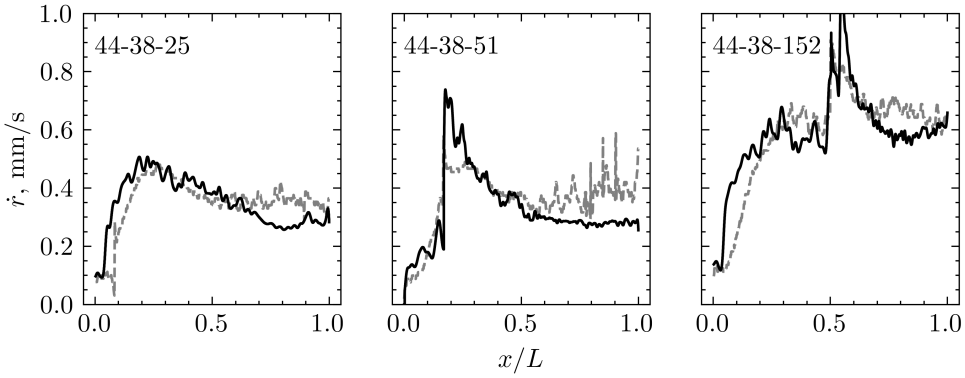

Fig. 14 Comparison of LES regression rates (solid) versus the experiments (dashed).

The computed heat flux to the fuel is shown in figure 15 for the three shallow geometries.

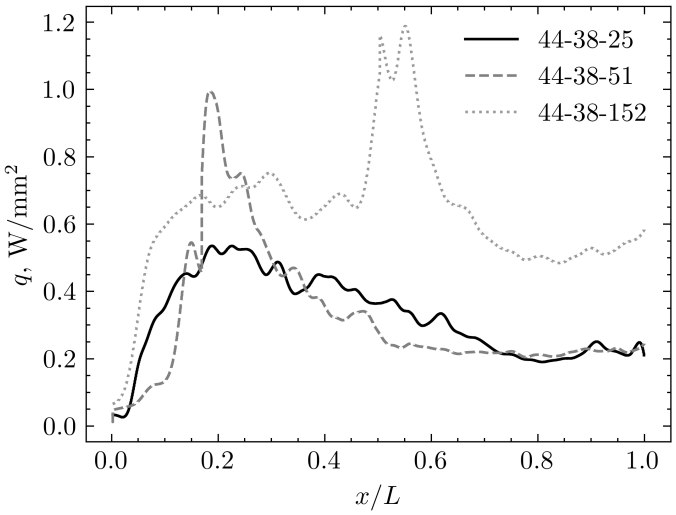

Fig. 15 Comparison of LES heat flux (feedback to the fuel) for the shallow geometries.

There are two major features highlighted by this figure. First, the addition of the cavity significantly increases the heat transfer to the solid. Second, the cavity corner introduces a strong peak in the heat flux similar to what was noticed in solid fuel scramjet simulations [36].

The spatially integrated values of the heat flux to the fuel wall are 11.8 kW, 12.2 kW, and 26.0 kW for the no cavity, 51 mm cavity, and the 152 mm cavity, respectively. Therefore, the present calculations identify a substantial increase in the heat feedback for long cavities and a modest increase for the short analogs. When combined with the experimental observation of a marginal increase in the combustion efficiency, this result points out that the cavity major effect is to modify the heat transfer not the chemical reactions. This feature will be analyzed in more details in the following section.

1. Temperature and Mixture Fraction Fields

The mixture fraction and temperature are shown in figure 16 and figure 17, showing the presence of a substantial hydrodynamic instability and a recirculation region with fuel accumulation in the upstream part of the cavity. Eddys with unmixed fluid are convected towards the fuel surface in the shear layer, where they react producing a significant and localized increase in the heat transfer. The presence of recirculating flow in the cavity makes the flowfield more complex from that in the schematic of figure 1. Pressure traces [13] demonstrate the presence of discrete harmonic tones of the cavity acoustic frequency, leading us to the conclusion that the cavity supports a global rather than local hydrodynamic instability. The contributions of the cavity hydrodynamics on the mean temperature field are significant and shown in figure 18. The no-cavity case supports the development of a diffusion flame in the boundary layer beyond the reattachment point and a correspondingly weak increase in the mean temperature field along the axis of the ramjet. The cavity cases feature a much faster increase of the temperature in the cavity due to the extension of the hot gas recirculation beyond the reattachment point. This effect is much larger in the long cavity. In this case the edge conditions

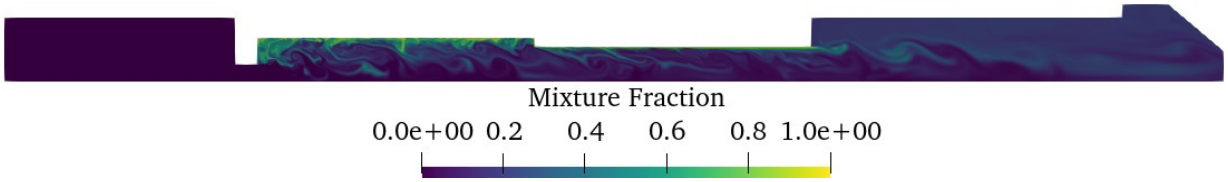

Fig. 16 Mixture fraction field at an instant in time for the ramjet simulation.

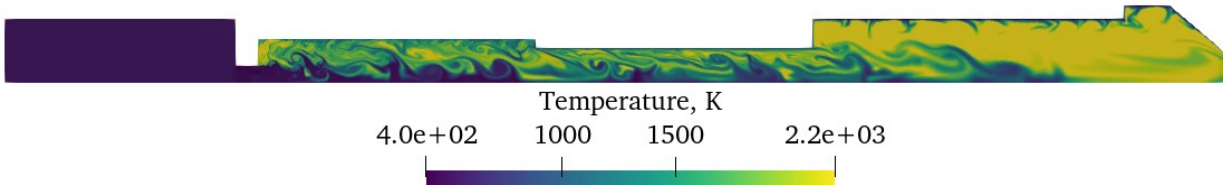

Fig. 17 Temperature field at an instant in time for the ramjet simulation.

of the boundary layer on the fuel walls outside of the cavity are determined by the hot gas that has recirculated in the cavity, which explains the much larger regression and heat flux for $x/L > 1/2$ described in figure 14 and figure 15.

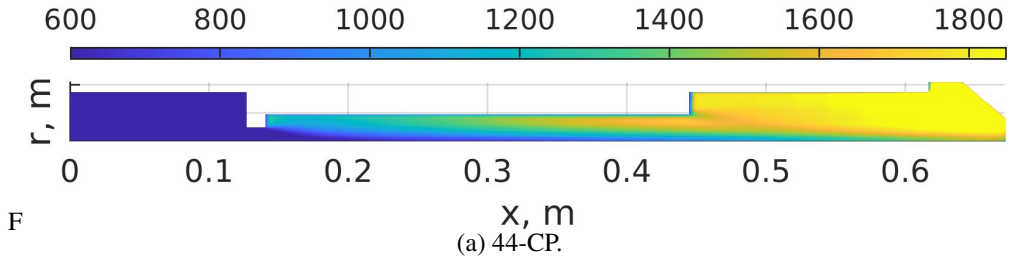

F

(a) 44-CP.

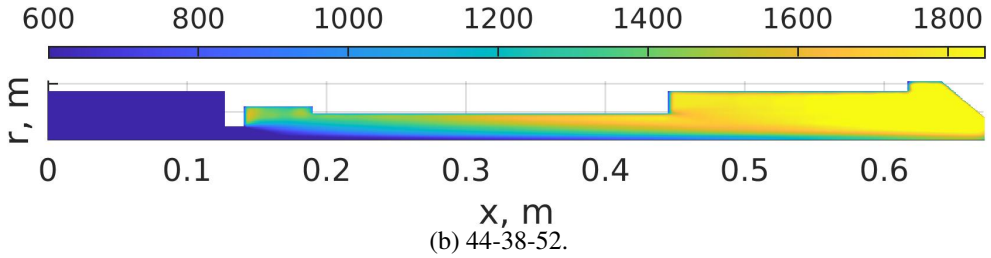

(b) 44-38-52.

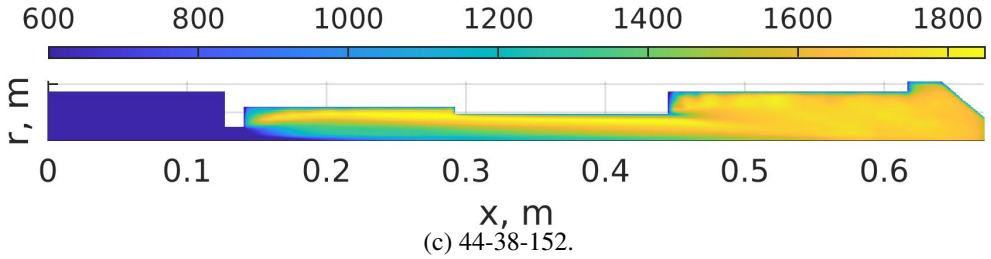

(c) 44-38-152.

Fig. 18 Calculated time-averaged temperature field in the ramjet.

V. Conclusion

Introduction of a cavity flameholder into solid fuel ramjet fuel grains improved the flameholding limits of the combustor, by allowing sustained combustion at increased fuel loading. Presented regression patterns demonstrate that the presence of the cavity flameholder affects the reattachment points downstream location and location of maximum regression. The analysis revealed that the average regression rate in the port region of the fuel grain was seen to have significantly higher regression than that of the cavity. Despite insensitivities to changes in combustion efficiency, chamber pressure was observed to increase with increasing cavity length. Increasing the cavity length to half the length of a representative center perforated grain allows a higher in chamber pressure above that which would be seen with the center perforated fuel grain.

Numerical investigations of the flameholding fuel grains demonstrated that the introduction of a cavity flame holder increased the heat feedback in the reciruculation region and contributed to global hydrodynamic instabilities in the combustor. Calculated regression patterns agree well with experimental results and the resulting computed heat flux support the conclusion of increased heat transfer as the dominant mechanism of increased flameholding.

Acknowledgements

We gratefully acknowledge the support of the Office of Naval Research and Program Officer Dr. Chad Stoltz under Grant Number: N00014-20-1-2316 and Program Officer Dr. Eric Marineau under Grant No. N00014-21-1-2299.

References

[1] Hill, P., and Peterson, C., *Mechanics and Thermodynamics of Propulsion*, 2nd ed., Pearson, Reading, Massachusetts, 1992.

[2] Schulte, G., "Fuel Regression and Flame Stabilization Studies of Solid-Fuel Ramjets," *Journal of Propulsion and Power*, Vol. 2, No. 4, 1986, pp. 301–304. https://doi.org/10.2514/3.22886.

[3] Zvuloni, R., Gany, A., and Levy, Y., "Geometric Effects on the Combustion in Solid Fuel Ramjets," *Journal of Propulsion and Power*, Vol. 5, No. 1, 1989, pp. 32–37. https://doi.org/10.2514/3.23111.

[4] Zvuloni, R., Levy, Y., and Gany, A., "Investigation of a Small Solid Fuel Ramjet Combustor," *Journal of Propulsion and Power*, Vol. 5, No. 3, 1989, pp. 269–275. https://doi.org/10.2514/3.23148.

[5] Korting, P. A. O. G., van der Geld, C. W. M., Wijchers, T., and Schoyer, H. F. R., "Combustion of Polymethylmethacrylate in a Solid Fuel Ramjet," *Journal of Propulsion and Power*, Vol. 6, No. 3, 1990, pp. 263–270. https://doi.org/10.2514/3.25429.

[6] Netzer, A., and Gany, A., "Burning and Flameholding Characteristics of a Miniature Solid Fuel Ramjet Combustor," *Journal of Propulsion and Power*, Vol. 7, No. 3, 1991, pp. 357–363. https://doi.org/10.2514/3.23334.

[7] Wooldridge, R. C., and Netzer, D. W., "Ignition and Flammability Characteristics of Solid Fuel Ramjets," *Journal of Propulsion and Power*, Vol. 7, No. 5, 1991, pp. 846–848. https://doi.org/10.2514/3.23400.

[8] Buckley, P., Craig, R., and Obleski, B., "The Effect of Swirl on a Ramjet Dump Combustor," AIAA Paper 79-7042, Orlando, Florida, 1979. https://doi.org/10.2514/6.1979-7042.

[9] Musa, O., Xiong, C., and Changsheng, Z., "Experimental and Numerical Investigation on the Ignition and Combustion Stability in Solid Fuel Ramjet with Swirling Flow," *Acta Astronautica*, Vol. 137, 2017, pp. 157–167. https://doi.org/10.1016/j.actaastro.2017.04.021.

[10] Musa, O., Weixuan, L., Xiong, C., Lunkun, G., and Wenhe, L., "Experimental Investigation on the Effect of Swirling Flow on Combustion Characteristics and Performance of Solid Fuel Ramjet," *Acta Astronautica*, Vol. 148, 2018, pp. 163–174. https://doi.org/10.1016/j.actaastro.2018.04.055.

[11] Connell, T., Young, G., Beckett, K., and Gonzalez, D. R., "Enhanced Solid Fuel Regression in a Hybrid Rocket Employing Additively Manufactured Fuels Exhibiting Novel Grain Port Geometries," AIAA Paper 2019-2015, San Diego, California, 2019. https://doi.org/10.2514/6.2019-2015.

[12] Ben-Yakar, A., Natan, B., and Gany, A., "Investigation of a Solid Fuel Scramjet Combustor," *Journal of Propulsion and Power*, Vol. 14, No. 4, 1998, pp. 447–455. https://doi.org/10.2514/2.5321.

[13] Pace, H., Arnold, C., Gallegos, D., Young, G., and Massa, L., "Acoustics in Flameholding Solid Fuel Ramjet Fuel Grains," *AIAA Journal (not yet published).*, 2023.

[14] Geuzaine, C., and Remacle, J.-F., "Gmsh: A 3-D Finite Element Mesh Generator with Built-in Pre-and Post-Processing Facilities," *International Journal for Numerical Methods in Engineering*, Vol. 79, No. 11, 2009, pp. 1309–1331. https://doi.org/10.1002/nme.2579.

[15] Economon, M., Palacios, F., Copeland, S. R., Lukaczyk, T., and Alonso, J. J., "SU2: An Open-Source Suite for Multiphysics Simulation and Design," *AIAA Journal*, Vol. 54, No. 3, 2016, pp. 828–846. https://doi.org/10.2514/1.J053813.

[16] Johnson, R. F., and Kercher, A. D., "A Conservative Discontinuous Galerkin Discretization for the Chemically Reacting Navier-Stokes Equations," *Journal of Computational Physics*, Vol. 423, 2020, p. 109826. https://doi.org/10.1016/j.jcp.2020.109826.

[17] Pierce, C. D., and Moin, P., "Progress-Variable Approach for Large-Eddy Simulation of Non-Premixed Turbulent Combustion," *Journal of Fluid Mechanics*, Vol. 504, 2004, pp. 73–97. https://doi.org/10.1017/S0022112004008213.

[18] Poinsot, T., and Veynante, D., *Theoretical and Numerical Combustion*, RT Edwards, Inc., Philadelphia, Pennsylvania, 2005.

[19] Bilger, R., "A Note on Favre Averaging in Variable Density Flows," *Combustion Science and Technology*, Vol. 11, No. 5-6, 1975, pp. 215–217. https://doi.org/10.1080/00102207508946700.

[20] Bilger, R., Stårner, S., and Kee, R., "On Reduced Mechanisms for Methane-Air Combustion in Nonpremixed Flames," *Combustion and Flame*, Vol. 80, No. 2, 1990, pp. 135–149. https://doi.org/10.1016/0010-2180(90)90122-8.

[21] Pierce, C. D., and Moin, P., "A Dynamic Model for Subgrid-Scale Variance and Dissipation Rate of a Conserved Scalar," *Physics of Fluids*, Vol. 10, No. 12, 1998, pp. 3041–3044. https://doi.org/doi.org/10.1063/1.869832.

[22] Nguyen, T. M., and Sirignano, W. A., "Spontaneous and Triggered Longitudinal Combustion Instability in a Single-Injector Liquid-Rocket Combustor," *AIAA Journal*, Vol. 57, No. 12, 2019, pp. 5351–5364. https://doi.org/doi.org/10.2514/1.J057743.

[23] Kee, R. J., Coltrin, M. E., and Glarborg, P., *Chemically Reacting Flow: Theory and Practice*, John Wiley & Sons, Hoboken, New Jersey, 2005.

[24] Chen, M., Buckmaster, J., Jackson, T., and Massa, L., "Homogenization Issues and the Combustion of Heterogeneous Solid Propellants," *Proceedings of the Combustion Institute*, Vol. 29, No. 2, 2002, pp. 2923–2929. https://doi.org/10.1016/S1540-7489(02)80357-1.

[25] Dakshnamurthy, S., Knyazkov, D. A., Dmitriev, A. M., Korobeinichev, O. P., Nilsson, E. J., Konnov, A. A., and Narayanaswamy, K., "Experimental Study and a Short Kinetic Model for High-Temperature Oxidation of Methyl Methacrylate," *Combustion Science and Technology*, Vol. 191, No. 10, 2019, pp. 1789–1814. https://doi.org/10.1080/00102202.2018.1535492.

[26] Goodwin, D. G., Moffat, H. K., Schoegl, I., Speth, R. L., and Weber, B. W., "Cantera: An Object-Oriented Software Toolkit for Chemical Kinetics, Thermodynamics, and Transport Processes," , 2022. URL http://www.cantera.org.

[27] Sun, W., Zhao, Q., Curran, H. J., Deng, F., Zhao, N., Zheng, H., Kang, S., Zhou, X., Kang, Y., Deng, Y., Huang, Z., and Zhang, Y., "Further Insights into the Core Mechanism of H2/CO/NOx Reaction System," *Combustion and Flame*, Vol. 245, 2022, p. 112308. https://doi.org/10.1016/j.combustflame.2022.112308.

[28] Pace, H., Jessup, A., Gallegos, D., Young, G., and Massa, L., "Counterflow Combustion and Regression of PMMA Model Fuel," AIAA Paper 2022-3996, Chicago, Illinois & Virtual, 2022. https://doi.org/10.2514/6.2022-3996.

[29] Oevermann, M., "Numerical Investigation of Turbulent Hydrogen Combustion in a SCRAMJET using Flamelet Modeling," *Aerospace Science and Technology*, Vol. 4, No. 7, 2000, pp. 463–480. https://doi.org/10.1016/S1270-9638(00)01070-1.

[30] Arisawa, H., and Brill, T., "Kinetics and Mechanisms of Flash Pyrolysis of Poly(methyl methacrylate) (PMMA)," *Combustion and Flame*, Vol. 109, No. 3, 1997, pp. 415–426. https://doi.org/10.1016/S0010-2180(96)00190-3.

[31] Beckstead, M. W., Puduppakkam, K., Thakre, P., and Yang, V., "Modeling of Combustion and Ignition of Solid-Propellant Ingredients," *Progress in Energy and Combustion Science*, Vol. 33, No. 6, 2007, pp. 497–551. https://doi.org/10.1016/j.pecs.2007.02.003.

[32] Chauhan, M., and Massa, L., "Large-Eddy Simulation of Supersonic Jet Noise with Discontinuous Galerkin Methods," *AIAA Journal*, Vol. 60, No. 3, 2022, pp. 1451–1470. https://doi.org/10.2514/1.J060424.

[33] Bonfiglioli, A., and Paciorri, R., "Convergence Analysis of Shock-Capturing and Shock-Fitting Solutions on Unstructured Grids," *AIAA Journal*, Vol. 52, No. 7, 2014, pp. 1404–1416. https://doi.org/10.2514/1.J052567.

[34] Gordon, S., and McBride, B., "Computer Program for Calculation of Complex Chemical Equilibrium Compositions and Applications. Part 1: Analysis," Tech. Rep. NASA-RP-1311, Lewis Research Center, Cleveland, Ohio, Oct. 1994.

[35] McBride, B., and Gordon, S., "Computer Program for Calculation of Complex Chemical Equilibrium Compositions and Applications; Part II: Users Manual and Program Decription," Tech. Rep. NASA-RP-1311, Lewis Research Center, Cleveland, Ohio, Jun. 1996.

[36] Chi, H.-w., Wei, Z.-j., Wang, L.-h., Li, B., and Wu, Z.-w., "Numerical Investigation of Self-Ignition Characteristics of Solid-Fuel Scramjet Combustor," *Journal of Propulsion and Power*, Vol. 31, No. 4, 2015, pp. 1019–1032. https://doi.org/10.2514/1.B35301.

Chapter 5

Acoustic Modes in Solid Fuel Ramjets

In this chapter I describe the main techniques to extract the acoustic modes from the Ramjet LES simulations described in the previous chapters. The main results are included in a paper I submitted to the AIAA Journal, which is currently under view. The highlights of my research are described here in more details. The full paper is reported in what follows.

5.0.1 Inlet Conditions

While the 3D simulations include the side ports for the air feed into the ramjet, the axisymmetric simulations use an inflow plane with prescribed total pressure and temperature. To ensure that the assigned inlet total conditions were valid, mass flow rate was recorded at the inlet and exit of the cavity and plotted as a simulation progressed. The average inlet and outlet flow rate values were seen to converge to slightly over 0.2 kg/s, which agrees well with the specified mass flow rate in the experiment (0.215 kg/s).

5.0.2 Spectral Proper Orthogonal Decomposition

SPOD is a method for taking computational or experimental datasets and extracting flow patterns or modes that are coherent in space and time. These modes are eigenvectors of the tensor of cross-spectral density (CSD) at each frequency. SPOD assumes that the dataset is statistically stationary, such that the mean and variance of values do not vary with time.

An efficient algorithm proposed by [14] and [15] is used in this research and detailed below in section 5.0.2. Results and analysis are listed in the attached paper

SPOD formulation

The CSD matrix S used for calculating SPOD modes is estimated from LES. Welch's periodogram (pWelch) is used to estimate and assemble a set of realizations of the Fourier transform in time of the data from a series of N_t snapshots by splitting this into N_{blk} blocks, each composed of N_{FFT} snapshots and overlapping with preceding and later snapshots by N_{ovlp}. This relationship is decribed by

$$N_{blk} = \frac{N_t - N_{ovlp}}{N_{FFT} - N_{ovlp}} \tag{5.1}$$

5.0.3 SPOD Application

At the location of the mixing chamber tap, the power spectral density (PSD) was calculated to allow comparison of acoustic signals. To determine the origins of the acoustic signals observed in the PSD plots, Spectral Proper Orthogonal Decomposition (SPOD) is used. SPOD extracts coherent structures (modes) in a flow that are coherent in space and time. Each mode is an eigenvector λ of a Cross-Spectral-Density (CSD) at each frequency [16]. Unlike the original SPOD code, the SPOD code used in this report scales the modes by the time window over which they were calculated, allowing the modes to be defined in terms of their signal power instead of their cumulative energy. The signal used for SPOD is p/p_0 where p is the local pressure in the cavity and p_0 is the inlet stagnation pressure.

The SPOD code used in this project was implemented in MATLAB by Oliver Schmidt and can be found on GitHub and the Mathworks websites.[17]. As the original code only

works on n-dimensional structured grids with constant frequency snapshots, interpolation and domain-sectioning functions are added to reformat the unstructured and irregularly sampled simulation data. Pressure data from the unstructured ramjet meshes were interpolated spatially to a structured 811×51 point grid, and temporally to regular intervals over a period of 50 ms. Pressure data was normalized by the inlet stagnation pressure, and then SPOD was performed. The most energetic modes were recorded and plotted below.

5.0.4 Turbulence Models

Turbulence models are required to close the non-linear terms in the Favre filtered Navier-Stokes equations. These terms typically include Reynolds stress on the momentum equation and sub-grid fluctuations of the mixture fraction in the chemistry source terms. The latter contributions are modelled using a PDF-based filtering approach in phase space, which is described next.

Models of Turbulent Source Terms in Phase Space

In order to account for subgrid fluctuations within the ramjet simulation, a probability distribution function was used inside the LES code. This was extracted from the flamelet libraries using the open source code SpitFire [18]. Clipped Gaussian (CG) and beta (β) PDFs were explored. Their effect inside the full ramjet simulations are discussed below. An example of a Clipped Gaussian distribution is shown in Figure 5.1 for the readers benefit.

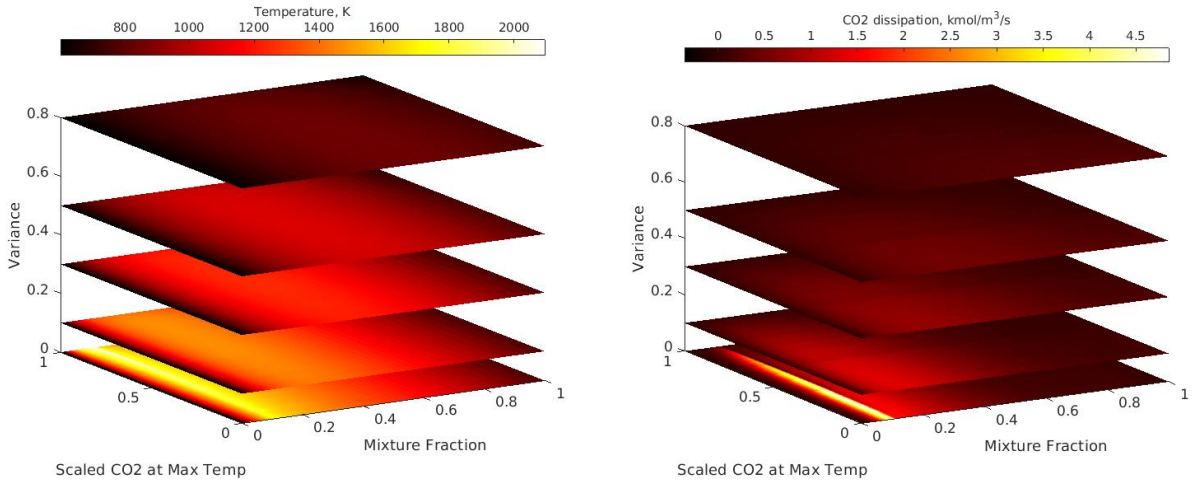

(a) Temperature as a function of (Z, χ, P) (b) Scalar dissipation as a function of (Z, χ, P)

Figure 5.1: Turbulent library storage of temperature and CO_2 dissipation

5.1 LES Subgrid models

Subgrid-Scale Modeling of the Momentum Transfer

A Large Eddy Simulation (LES) is a type of turbulence computation in which mid and large scale eddies are simulated while the effects of the smallest, sub grid-scale (SGS), eddies are approximated with a model. For practical LES, an efficient, accurate, and numerically stable SGS model is required to account for the effects of the unresolved small-scale turbulence on the larger scale flow. SGS models for LES usually operate in a range of scales that are marginally resolved by discretization schemes. In this research, we primarily compared the Smagorinksy and Wall Adapting Local Eddy Viscosity (WALE) SGS models in their application for simulation of the ramjet.

Different sub-grid models are used to determine the best approach to resolve the coherent structures created by the ramjet cavity shear-layer in the near-field. In this research, comparison of three different SGS models, i.e., Implicit LES (ILES), Smagorinsky and WALE models and investigated their accuracy when used with a Discontinuous Galerkin discretiza-

tion to analyze the effect of thermal non-uniformity on supersonic noise generation. The formulations of the Smagorinsky and WALE are discussed in detail below.

Smagorinsky model

The Smagorinsky model assumes that the SGS stresses follow a gradient-diffusion process similar to that found for molecular motion. This basic model is successful for two primary reasons [19], first, this model yields sufficient diffusion and dissipation to stabilize the numerical computations and second, the low order statistics of large-scale eddies are usually insensitive to SGS motions. Here, τ_{ij} is given by

$$\tau_{ij} = 2\nu_T S_{ij}, \text{ where } S_{ij} = \frac{1}{2}\left(\frac{\partial \overline{u_i}}{\partial x_j} + \frac{\partial \overline{u_j}}{\partial x_i}\right) \tag{5.2}$$

where S_{ij} is called the "resolved strain rate," and ν_T is the Smagorinsky eddy viscosity which is given by,

$$\nu_T = (C_S\Delta)^2\sqrt{S_{ij}S_{ij}} \tag{5.3}$$

and C_S is they coefficient and grid scale, $\Delta = (\Delta x \Delta y \Delta z)^{1/3}$. Since the standard Smagorinsky model does not satisfy the requirement that eddy viscosity for inhomogenous turbulent flow should become small in laminar and transitional regions, a new dynamic Smagorinsky model is used that solves this problem by implementing a dynamic procedure that incorporates explicit filtering operations, ensemble averaging in homogeneous directions, and an ad-hoc clipping to prevent an unstable (negative) eddy viscosity [20]. In SU2 platform, LES runs with the Smagorinsky model with and without wall functions where $C_S = 0.1$ in the above equation 5.3.

Wall Adaptive Model Equations (WALE)

The WALE model [21] [22] has a similar level of complexity to the Smagorinsky model, however it is constructed in such a manner that it has comparatively little dissipation in the transitional and near-wall regions. The WALE model is based on the fundamental realizability inequality for theoretical subgrid dissipation. As noted by Vreman [21], this model tends to be more accurate than the Smagorinsky model and comes quite close to the standard dynamic model. The equation for eddy viscosity in the WALE model is given by

$$\nu_e = C\sqrt{B_\beta/\alpha_{ij}\alpha_{ij}} \tag{5.4}$$

where

$$\alpha_{ij} = \frac{\partial \overline{u_j}}{\partial x_i}, \beta_{ij} = \Delta_m^2 \alpha_{mi}\alpha_{mj}, B_\beta = \beta 11\beta_{22} - \beta_{12}^2 + \beta 11\beta_{33} - \beta_{13}^2 + \beta 22\beta_{33} - \beta_{23}^2 \tag{5.5}$$

where c is the Vreman constant, equal to 0.07, and α represents the 3x3 matrix of derivatives (Jacobian) of the filtered velocity $\overline{u}$.

5.1.1 Field Analysis

The large peaks in burn rate and heat flux correspond with the beginning of major changes in the standard deviation of the burn rate, as shown in the burn rate plots included in the attached paper submission. These locations identify the furthest upstream point of the boundary layer re-attachment region. The mixture fraction and temperature are shown in

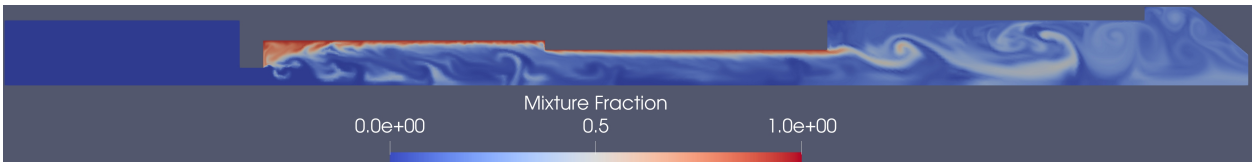

Figure 5.2: Mixture fraction field at an instant in time for the ramjet simulation with V_β model.

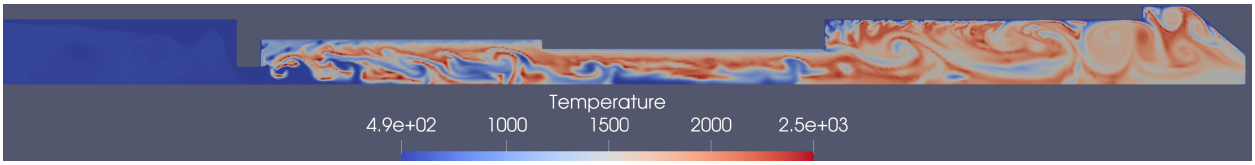

Figure 5.3: Temperature field at an instant in time for the ramjet simulation with V_β model.

Figure 5.2 and Figure 5.3, showing the presence of a recirculation region with fuel accumulation in the upstream part of the cavity. Eddies with unmixed fluid are convected towards the fuel surface in the shear layer, where they react producing a significant localized increase in the heat flux. The time-mean of the temperature and the mixture fraction are further shown in Figure 5.4 and Figure 5.5, respectively. The temperature plot clearly shows the presence of a thin region of high temperature supported by mixing caused by the hydrodynamic instability of the jet shear layer. This high temperature gas is responsible for the sharp increase in fuel regression rates noticed in both simulations and experiments.

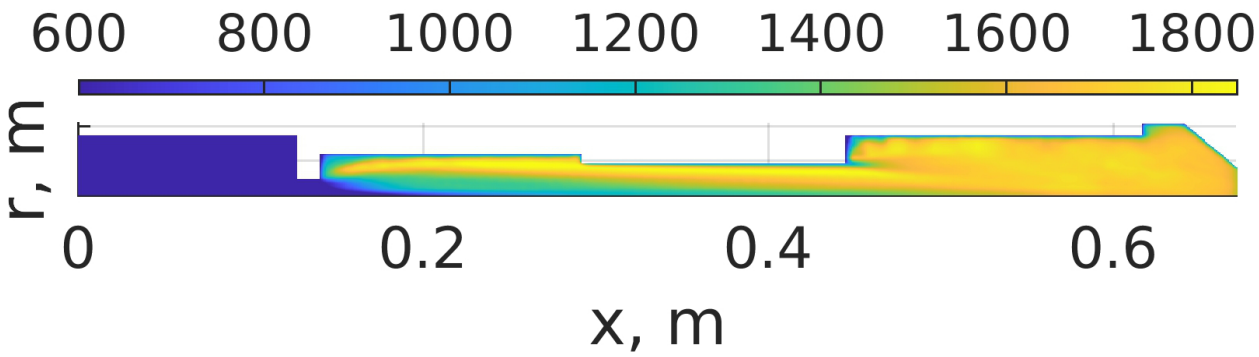

Figure 5.4: Mean temperature field for the ramjet simulation with V_β model.

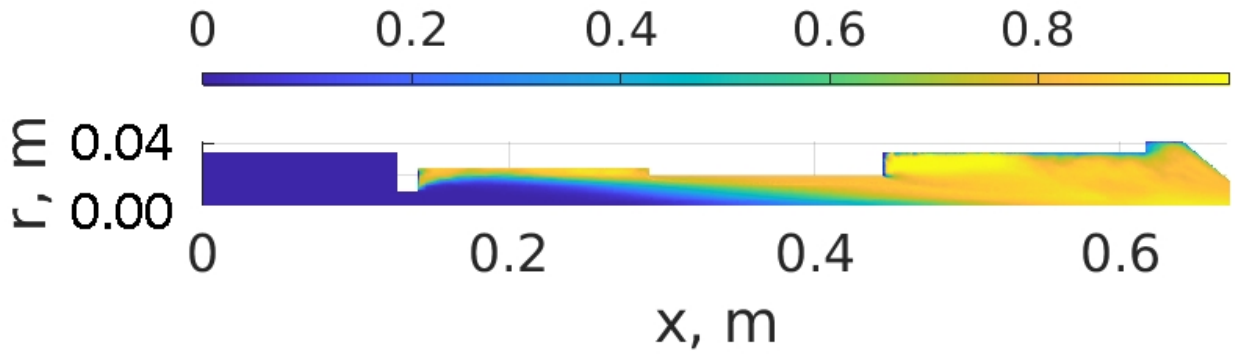

Figure 5.5: Mean mixture fraction field for the ramjet simulation with V_β model.

5.1.2 Acoustics

Both the Smagorinsky and WALE subgrid scale models were able to approximately reproduce the dominant acoustic frequencies found in the ramjet experimental data, with peaks observed at multiples of 10 of the cavity fundamental frequency (see 5.6). However, numerical dissipation was a problem for both, resulting in the peaks in the Power Spectral Density (PSD) plots becoming smoothed out, as seen in 5.6. The WALE model had lower dissipation, however it was also more susceptible to numerical instability due to the shocks at the injector in the cold flow analysis. As a result, less data was collected with the WALE model than with the Smagorinsky model. The addition of the flamelet model appeared to shift SPOD modes to higher frequencies. This can be attributed to the increased temperature within the combustion chamber, which in turn increases the speed of sound. No significant thermoacoustic feedback effects were observed in the 2D simulations. However, consideration must be made for the possibility 3D effects being important.

5.1.3 Three-dimensional Effects

A three-dimensional view of the quarter-space grid used in the RANS is shown in Figure 5.8, which clearly shows the intake ports in the left.

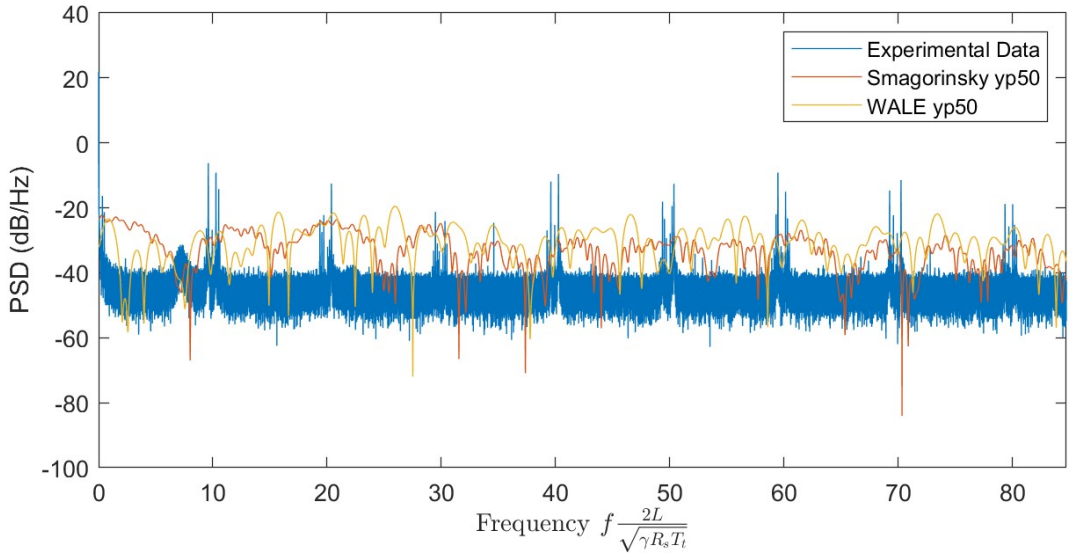

Figure 5.6: Comparison of acoustic frequencies for cold and hot flows

5.9 shows momentum in different planes of the 3D simulation, with the 2D simulation overlaid on the upper half of the X-Y plane view.

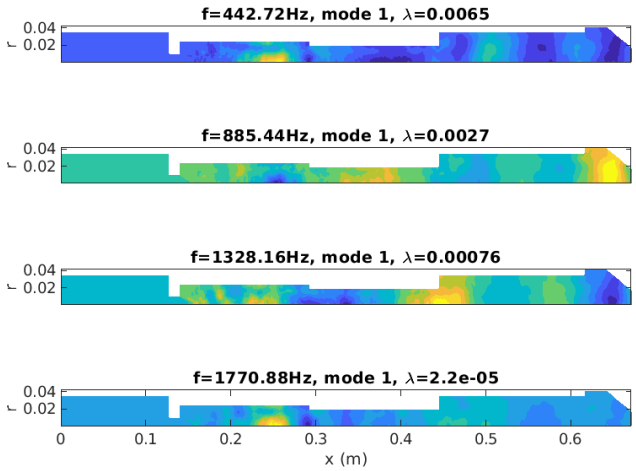

(a) Cold Flow Smagorinsky

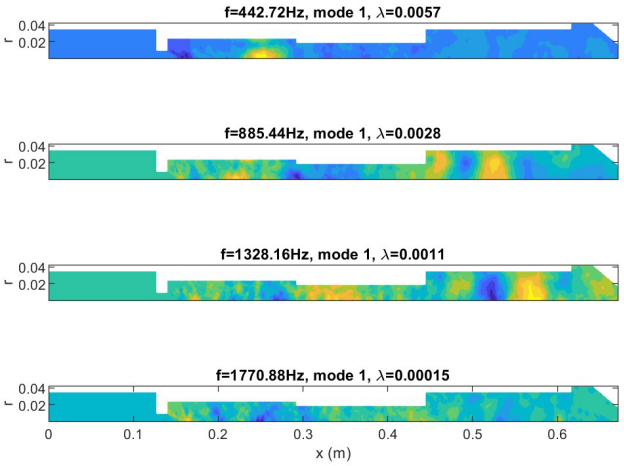

(b) Cold Flow WALE

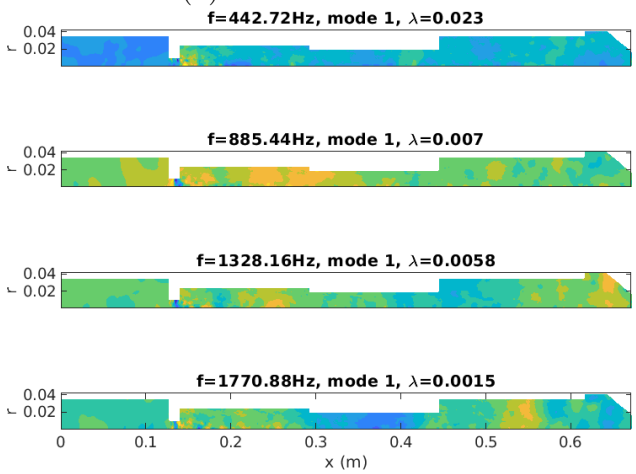

(c) Hot Flow Smagorinsky

Figure 5.7: SPOD modes for cold and hot flow simulations

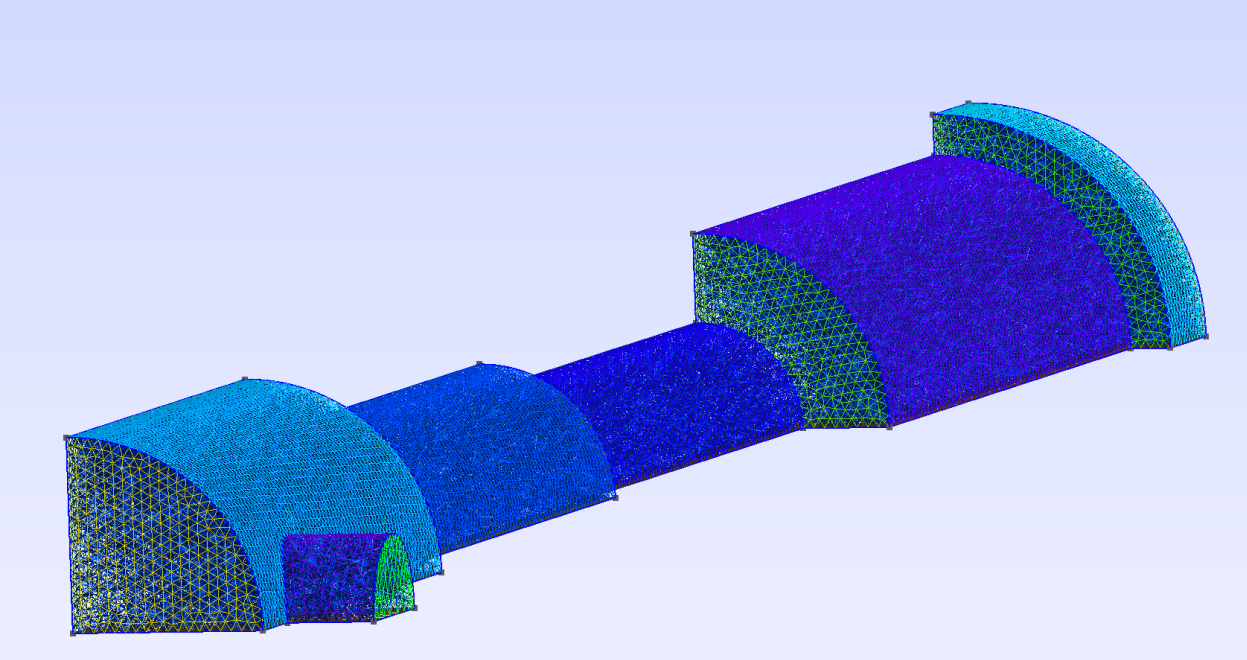

Figure 5.8: Three dimensional grid

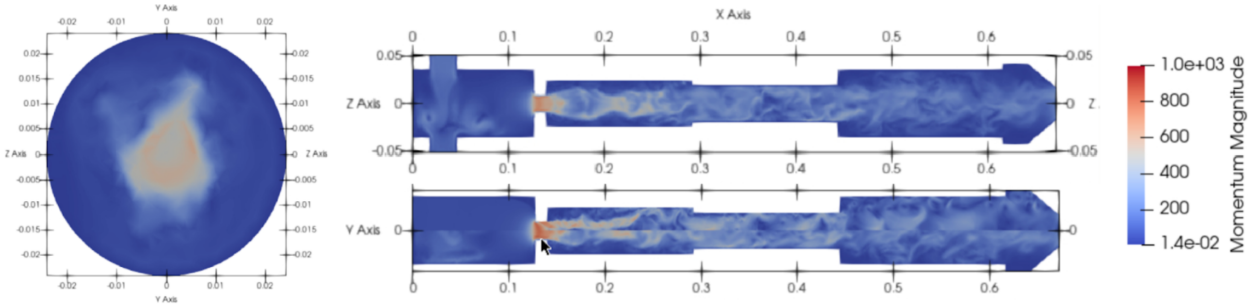

Figure 5.9: Momentum $\frac{kg}{m^2 s}$ for 3D and 2D Simulations

Acoustics in Flameholding Solid Fuel Ramjet Fuel Grains

Henry Pace * , Charles Arnold † , Dominic Gallegos ‡ , Greg Young§ and Luca Massa¶
Virginia Polytechnic Institute, Blacksburg, Virginia 24061-0203

Experiments are conducted to determine how acoustic perturbations affect the performance and flame-holding of solid fuel ramjets with non-standard combustion chambers. The focus is on the effect of wall cavities carved in the fuel grain using additive manufacturing. An improved understanding of how the wall geometry contributes to the establishment of acoustic modes is sought. A novel combustion mechanism was developed using a counterflow burner to study the combustion and regression of solid model fuel polymethyl methacrylate (PMMA). The diffusion flame between the fuel and oxidizer was studied numerically using a solid fuel decomposition and melt layer model to simulate convection and pyrolysis of the material. This model was validated using new experimental data as well as previously published works. The foam layer parameters are critical to the success of the validation, showing that the increased residence time of the gas in the bubbles facilitates the fuel breakdown. Fourth order computational simulations of ramjet combustion without regressing fuel walls using a novel discontinuous Galerkin approach are performed with a fully conjugate solution for the thermal wave in the solid. Turbulent transport strongly affects the heat feedback to the walls and low frequency vortical modes (e.g., with a vortical wavemaker) associated with a recirculation region at the injector upstream wall are linked to an increase in chamber pressure and fuel mass flux.

Nomenclature

a	=	local speed of sound $\mathrm{m\,s^{-1}}$
d	=	distance between counterflow inlets m
r_b	=	burn rate $\mathrm{mm\,s^{-1}}$
μ and μ_t	=	mean molecular and turbulent (eddy) dynamic viscosity Pa s
ν and ν_t	=	mean molecular and turbulent kinematic viscosity $\mathrm{m^2/s}$
$\tilde{\nu}$	=	SA work-variable $\mathrm{m^2/s}$
ρ	=	density $\mathrm{kg\,m^{-3}}$

*PhD Student, Kevin T. Crofton Dept. of Aerospace & Ocean Engineering, 460 Old Turner St., Student Member AIAA
†PhD Student, Kevin T. Crofton Dept. of Aerospace & Ocean Engineering, 460 Old Turner St., Student Member AIAA
‡PhD Student, Kevin T. Crofton Dept. of Aerospace & Ocean Engineering, 460 Old Turner St., Student Member AIAA
§Associate Professor, Kevin T. Crofton Dept. of Aerospace & Ocean Engineering, 460 Old Turner St., Senior Member AIAA
¶Associate Professor, Kevin T. Crofton Dept. of Aerospace & Ocean Engineering, 460 Old Turner St., Senior Member AIAA

$\dot{\omega}$	=	chemical source term $\mathrm{kg\,s^{-1}\,m^{-3}}$
$\dot{m}$	=	mass flow rate $\mathrm{kg\,s^{-1}}$
T	=	temperature k
t	=	time s
λ	=	thermal conductivity $\mathrm{W/mk}$
ϕ_f	=	void fraction
$\dot{w}_i$	=	mass production rate of species i
$\dot{m}''_{net}$	=	mass flux
A	=	cross-sectional area of fuel
A_g	=	cross-sectional area composed of gaseous species in foam
A_{sp}	=	specific surface area
n	=	number density of gas bubbles in foam
p	=	pressure
$p_{v,eq}$	=	pressure of vapor at equilibrium condition
s	=	gaseous MMA sticking coefficient
R_u	=	universal gas constant
W_i	=	molecular weight of species i
X_i	=	molar fraction of species i

Subscripts

0	=	Reference Conditions (0 K)
c	=	Condensed (liquid) Phase
f	=	Foam Phase
flamelet	=	Flamelet Variable
g	=	Gas Phase
s	=	Sensible
t	=	turbulent

I. Introduction

Ramjets and scramjets are widely utilized in high speed flight due to their superior fuel efficiency in comparison to turbojets or turbofans at the same speed. An issue that arises in these high speed propulsion systems is flame holding. Typical ramjet geometries with center-perforated grains support flame-holding by featuring a step between the

combustion chamber and the inflow nozzle (injector) so that the ratio of grain-to-inlet radius r_p/r_i is greater than one. This setup supports a re-circulation zone able to increase the residence time of the products of the fuel gasification [1]. The fuel residence time is greatly affected by the geometry of the step due to the size and extension of the re-circulation zone [2–4].

A drawback of the centered-perforated geometry with a step is that the volume of the fuel is decreased proportionally to the step height leading to a lower ballistic range. This drawback can be mitigated by limiting the extension of the step along the axial direction, thus introducing a cavity [5]. Such a non-standard geometry introduces new flow features and in particular acoustic modes that are deemed to help flame-holding [6]. The investigation of the acoustic and vortical modes induced by the cavity in solid fuel ramjets is the first of the two main topical areas of the present work.

The second topic of this work centers on the development of a combustion model for the pyrolysis of multiphase polymeric solid fuels and its integration with high order LES simulations that have aero-acoustic level of resolution [7]. The combustion of polymer model fuels is of interest to various propulsion systems such as hybrid rockets, solid fuel ramjets, and solid fuel scramjets [8, 9]. Air-breathing propulsion systems supported by the combustion of pyrolyzing fuel walls have several advantages when compared to rocket propulsion, including an enhanced stability of the deflagration, higher payload, and drastically increased specific impulse. The present contribution focuses on the burning of polymethyl methacrylate (PMMA) through a computational approach validated against laminar counterflow experiments and the implementation of this chemical mechanism into larger cavity turbulent simulations. Lautenberger and Fernandez-Pello [10] discuss various pyrolysis modeling strategies and emphasize the importance of creating enough simplifications that the number of variables is kept manageable while not compromising the generality of the model or neglecting important physics behind the problem. In the combustion of polymers, heat volatilization ΔH_v is of utmost importance if the model is to accurately predict the regression rate, yet its value depends nonlinearly on the heating rate suggesting a more complex process than a reaction sheet [11]. Therefore, using a simplified latent heat of vaporization model to describe the boundary condition at the pyrolizing surface can be challenging [12]. A novel 1D model for both the gas and solid phase kinetics was created and validated against counterflow burner experiments. Counterflow burners typically consist of two inlets that eject fuel and oxidizer axially at each other thus creating an expanding flame zone between them known as a diffusion flame. This counterflow setup has been modified in the present research to investigate the solid fuel pyrolysis and diffusion flames supported by a stagnation-flow flame over a regressing solid fuel. Previous research involving polymeric solid fuels in counterflow conditions has been conducted on PMMA with a nitrogen- air mixture by Seshadri and Williams [13], and hydroxyl-terminated polybutadiene with nitrous oxide by Nardozzo et al. [14]. The present investigation builds upon such existing measurements, but also conducts new experiments to support the modelling.

This paper is organized as follows: Section II details the experiments, Section III describes the numerical approach, Section IV discusses the main results, and Section V summarizes the conclusions.

II. Experimental Procedures

Two sets of numerical experiments were performed to investigate the effect of cavities in solid-fuel ramjets. First, counter-flow flame experiments were conducted to investigate regression rates under laminar quasi-onedimensional conditions. Second, ramjet firings were both the regression rates and pressure values were recorded. The experiments are described in more details by Young et al. [15] and Gallegos and Young [5].

A. Counterflow Experiments

A modified counterflow burner previously described by Young et al. [15], was used to characterize the diffusion flame between PMMA and hot air. House air is metered through an Omega FMA1820A-C flow meter and heated to a prescribed temperature with an Omega AHP-3742 inline duct heater. During the heating process, a metal plate is placed between the exit of the incoming air and the PMMA pellet. Once the desired temperature is reached, the plate is removed and the sample is ignited with a butane torch. A 10mm x 10mm right circular cylindrical PMMA pellet was held in a fixed location via a nichrome wire and a spring loaded linear variable displacement transducer (LVDT) which also measured regression rate by tracking the location of the bottom surface of the fuel pellet. The separation distance between the fuel pellet and heater exit was held fixed at 10 mm. A Vision Research Phantom VEO 710 high speed camera was used to image the location of the diffusion flame with respect to the fuel pellet surface as shown in figure 2. In the image melting is visible on the surface of the fuel which created a foam layer. This layer was not restricted by the nichrome wire, so the true distance between the oxidizer inlet and fuel was the difference between the 10 mm gap and the foam layer thickness. Because of this, all numerical simulations were run using a variable gap distance adjusted based on the calculated foam thickness.

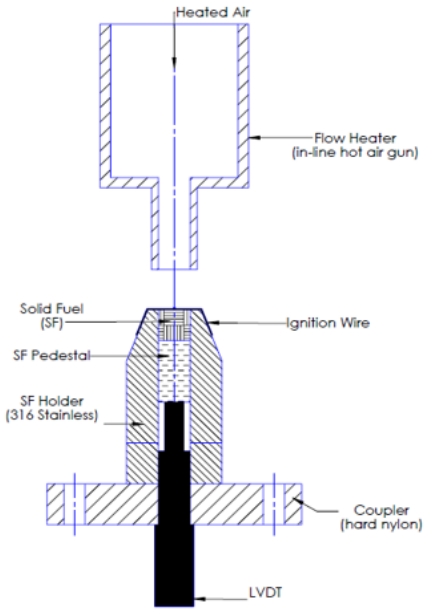

Fig. 1 Counterflow Burner Schematic Diagram [15]

Two-color pyrometry was applied to the images collected with the high speed camera following the methodology described by Densmore [16]. A MATLAB code was used to demosaic the Bayer filter of the camera sensor, provide the red, green, and blue values of each pixel, and determine the temperature of each pixel based on the red/green color ratio of the pixel. The camera was calibrated using a GE Lamp No. 1196 as an approximate black body. The lamp is a tungsten filament bulb for which the temperature of the filament can be determined as a function of its resistance. The bulb is recorded at different temperatures and the color data is used to generate a calibration curve for the camera relating temperature and the red-green color ratio.

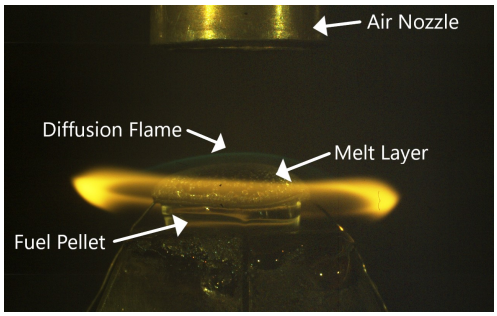

Fig. 2 High Speed Image of PMMA/Air Diffusion Flame

B. Ramjet Experiments

Figure 3 presents a diagram of the SFRJ test rig. High pressure air (1.3 MPa) was supplied to a 192kW electric heater, capable of heating the air to stagnation temperatures up to 873 K. Air was directed through an exhaust pipe

during the heat-up phase or through the combustor for firing via two pneumatically actuated valves. Mass flow control was achieved via a choked flow orifice upstream of the combustor. The combustor was comprised of three sections the inlet section, the fuel grain, and the mixing chamber. The inlet section consisted of two opposed air inlets and the igniter assembly, utilizing solid propellant and an electric match to ignite the fuel. The igniter assembly used approximately 7g of propellant per firing and comprised 20% R45-IPDI binder, 70% ammonium perchlorate, and 10% aluminum by weight. The inlet and fuel sections were separated by an injector plate with a smaller diameter hole than the fuel grain, creating the necessary step for flameholding. The fuel section utilized fuels with nominal outside diameters of 90mm and 70mm and lengths up to 317mm long. For the cavity fuel grains investigated in this study, port diameters of 36mm, 37mm, 38mm and cavity diameters of 44mm and 48mm were investigated. In addition, port diameters ranging from 38mm to 61mm were investigated to establish the initial flammability limits. The aft mixing chamber allowed increased residence time for the pyrolized fuel mixture, increasing the combustion efficiency. The products were then exhausted through the nozzle and out of the combustor. The fuel grains were epoxied into phenolic tubes for cartridge loading and unloading into the combustor. During the initial characterization of the combustor, both cast and 3D printed polymethylmethacrylate (PMMA) fuel grains were used. Printed PMMA fuel grains were prepared using a Raise3D Pro2 Plus FDM 3D printer using a 1mm nozzle. Cast fuel grains were prepared using commercially available PMMA rod and were drilled to the requisite diameter. To aid in ignition of the cast grains, the fuel was coated with a black spray paint and gunpowder mixture. This process was maintained through the firings of the cavity grains for consistency.

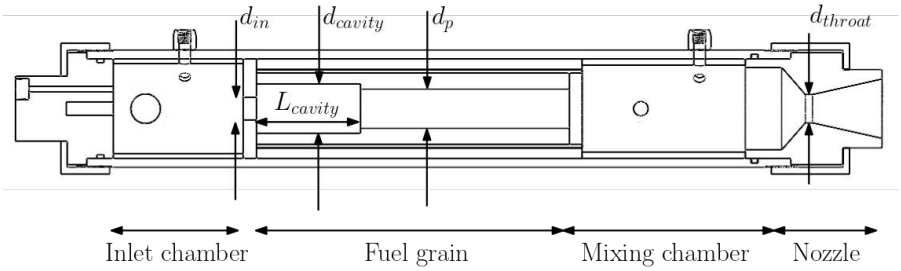

Fig. 3 Diagram of combustor sections and relevant dimensions.

Instrumentation consisted of: static pressure transducers (Setra 206) at the orifice, inlet chamber and mixing chamber; K-type thermocouples at the orifice and inlet; and video to provide visual observation. To determine dominant frequency data for the cavities during combustion, a dynamic pressure transducer (PCB 113B26) was installed in the mixing chamber at the same axial location as the static pressure transducer. A typical test profile proceeded as follows: air flowed through the exhaust pipe until the heater reached a steady, pre-selected temperature; the air control valves subsequently toggled position to begin flowing air through the combustor; the electric match/solid propellant was then ignited to start the fuel combustion; steady combustion proceeded for 10-15 seconds; followed by a nitrogen purge to halt combustion.

III. Numerical Approach

A. Gas Phase Chemical Mechanism

The chemical mechanism was based on 89 species and 629 reactions scheme appearing in previously published work [17], with several changes to the transport properties based on newly obtained results in computational chemistry as well as the added MMA condensed species. The flamelet and passive scalars models were implemented in a framework that facilitates the solution of multi-physics and multi-fidelity problems by interpolating the source terms for energy and mass exchange at the boundaries between physics zones.

This mechanism was implemented in Cantera [18] with few variation from the original formulation mainly regarding adjustments to the transport properties and the kinetic rates of C3-C5 species as reflected by published data. The NASA-7 transport model parameters have been reevaluated to better fit the data range without discontinuities, which prevented the Newton method from converging in the evaluation of the response of the fuel pyrolysis to changes in strain rate. Such response is used to approximate the flamelet tabulated rates beyond the maximum strain conditions.

Self-similar counter-flow diffusion flames were obtained at steady state and in one-dimension using a Newton method algorithm with adaptive mesh refinement. The species at the fuel inlet were interpolated from previously run foam simulations at a given heat flux and were mainly comprised of gaseous MMA ($C_5H_8O_6$). The oxidizer inlet ejected air comprising O_2 with molar fraction 0.21 and N_2 with fraction 0.79. The computational domain in which the flow was simulated is demonstrated in figure 4.

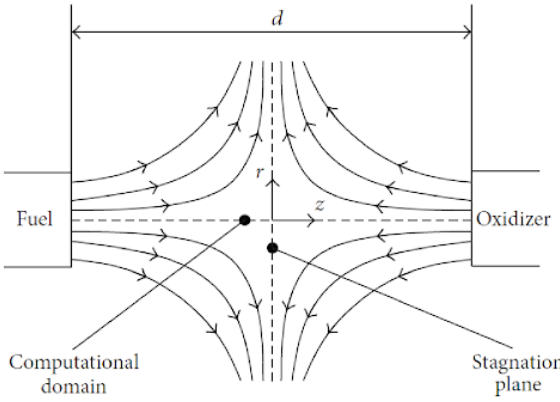

Fig. 4 Computational Space of Counterflow Simulation

Several species concentrations were plotted for the reader's benefit in figure 5. The z axis in this case stretched between the oxidizer (right) and fuel (left) inlets and referred to the distance in millimeters from the maximum flame temperature. Note that many species were present in the $-2mm < z < 1mm$ region near the flame; however, they did not exist in large quantities and are thus not shown.

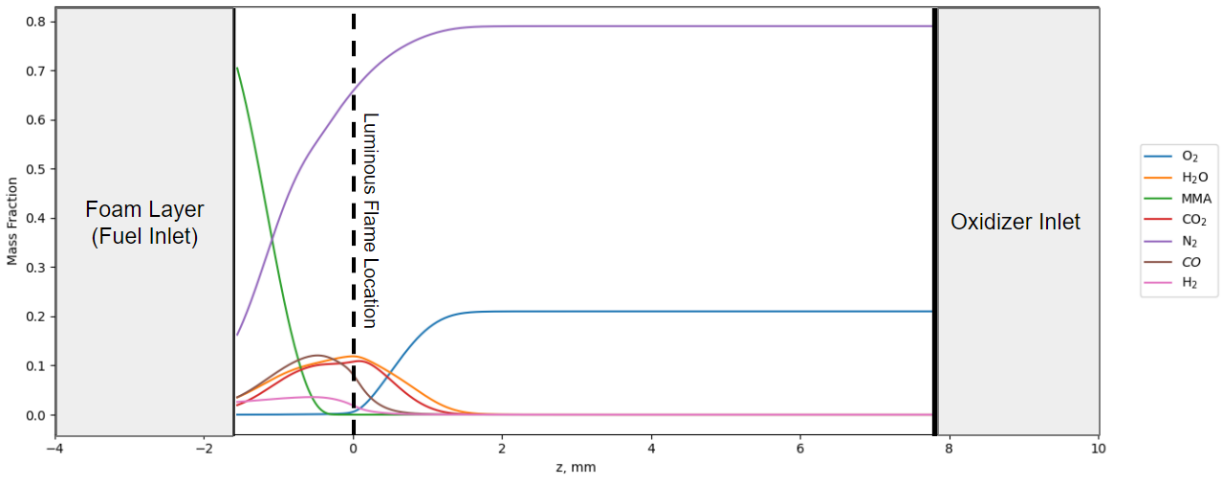

Fig. 5 Computed species mole fractions at oxidizer inlet conditions of 573 K and 0.432 $kg/(s * m^2)$

1. Flame Temperature and Mechanism Adjustments

Figure 6 provides an example of the results of our 2D two color pyrometry experiments used to measure the flame temperature, defined as the maximum temperature of the visible flame.

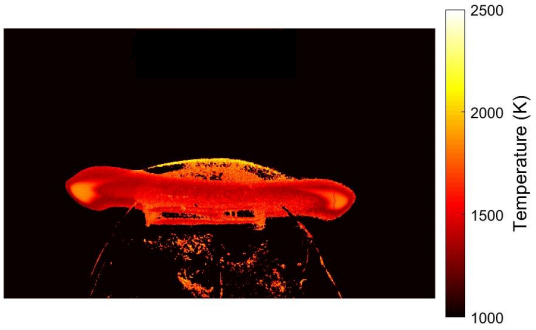

Fig. 6 2D Two Color Temperature Map of PMMA/Air Diffusion Flame

The original formulation of the mechanism, yields the flame temperature reported in the fourth column of Table 1. This was deemed too low because the lack of heat losses in the computations is expected to yield a higher flame value when compared to the experiments. In particular, for low air mass flux, the adiabatic flame temperature was not recovered. This observation also explains the low regression rates and high standoff distances obtained with the original model, which will be discussed later on in Section III.III.B.III.B.2. Because the original kinetic rates of the MMA decomposition pathways had been reduced in the work of Dakshnamurthy et al. [17] citing a lack of reliable experimental data or the loss of reaction pathways in the skeletal mechanism, a sensitivity analysis of the PMMA fuel regression rate on the kinetic coefficients of C3-C5 species was performed. New rates were taken from data published

by the National Institute of Standards (NIST) and the NUI mechanism [19]. The addition of new reactions was also based on sensitivity of the of counterflow experiments to the kinetics parameters, which included variations of the decomposition rates in the foam. A comparison between the original and modified mechanism flame temperatures is shown in Table 1. The modified mechanism leads to improved predictions of flame temperature especially at low air mass flux. The entire mechanism is provided as supplementary material to this submission.

Table 1 Diffusion Flame Temperature at Various Air Mass Flux Rates and Air Temperatures

Air Conditions		Diffusion Flame Temperature (K)		
Mass Flux	Temperature	Experimental	Original	Modified
[kg/m^{2}s]	[K]	[K]	[K]	[K]
0.432	573	2181	2034	2272
0.473	523	2238	2010	2266
0.576	573	2188	2019	2249
0.631	523	2134	1993	2233

The coupled flame and foam model was compared against previously published work [20] in Fig 7. One can see that the fuel surface temperature matches very well in both cases, and the maximum temperature is sightly higher in the simulations, but still shows good resemblance.

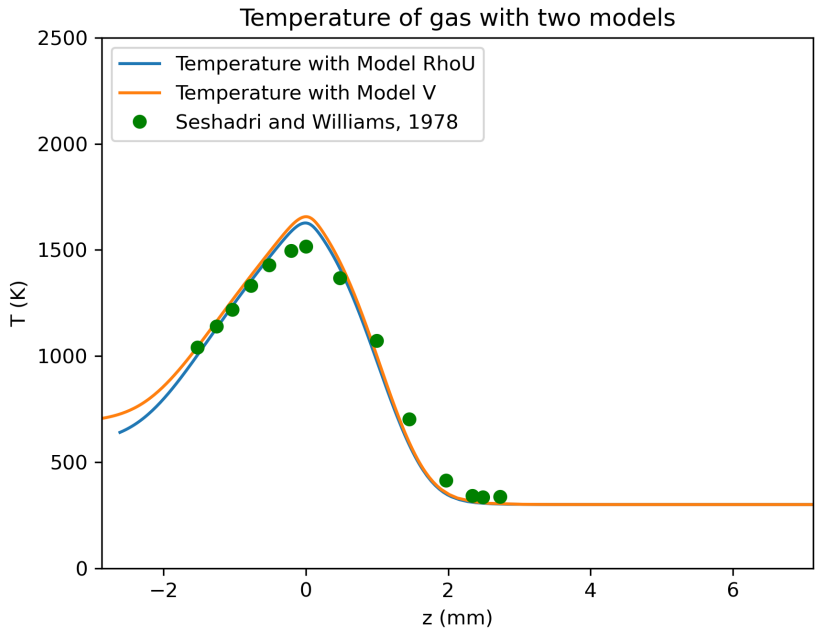

Fig. 7 Gas temperature vs location for two different foam models

B. Solid Decomposition Model

Past experimental results show that thermal decomposition of PMMA produces mainly Methyl methacrylate (MMA, $C_5H_8O_2$) 90% and carbon dioxide 10% [21]. The volumetric fraction of these two compounds does not vary significantly in the range of surface temperatures relevant to ramjet combustion 400 – 600°C, although it does vary weakly with pressure [22].

Because the experiments under discussion revealed that the foam thickness is comparable to the flame standoff distance a foam model is implemented between the gas and solid phases of the fuel. This model is based on the work of [23] and utilizes a void fraction, ϕ_f, ratio inside the foam. This is the area ratio of gaseous bubbles to condensed, liquid MMA; therefore, it ranges from zero at the solid/foam interface to 1 at the foam/gas surface. The value of ϕ_f is defined as

$$\phi_f = \frac{A_g}{A} \tag{1}$$

where A is the cross-sectional are of the fuel, and A_g denotes the area inside the cross section consisting of gaseous species.

The presence of bubbles inside the foam layer allow for evaporation and decomposition before the MMA reaches the gas interface. The net evaporation rate, $\dot{w}_{evap}$, is a function of the specific surface area, A_{sp}, and the mass flux, $\dot{m}_{net}$ as shown below:

$$\dot{w}_{evap} = A_{sp}\dot{m}''_{net}. \tag{2}$$

The mass flux and specific surface area are found using the following equations:

$$A_{sp} = (36\pi n)^{1/3}\phi_f^{2/3}, \phi_f < 1/2 \tag{3}$$

$$A_{sp} = (36\pi n)^{1/3}(1-\phi_f)^{2/3}, \phi_f > 1/2 \tag{4}$$

$$\dot{m}''_{net} = s\frac{1}{4}\sqrt{\frac{8R_uT}{\pi W_{MMA}}}\frac{pW_{MMA}}{R_uT}\left(\frac{p_{v,eq}}{p} - X_{\mathrm{MMA}}\right) \tag{5}$$

The sticking coefficient is the probability of a molecule sticking to a surface after collision and is usually a function of temperature, but a fixed value was used in this study. The number density, n, is defined as the number of bubbles of any size per cubic meter of the foam. Because little empirical data could be found for bubble number density of MMA at the temperatures observed in this work, several values were simulated in order to gain a more comprehensive idea of the value's effects. The total mass loss by the solid phase is obtained by adding the thermal decomposition rate $\dot{m}'$ to the net evaporation rate. Thermal decomposition is necessary to start the process of fuel gasification, since the initial volume fraction at the glass transition temperature is assumed zero and the rates in eq (3) are null. The latter is obtained assuming a linear pyrolysis model [24]. The rates of Korobeinichev et al. [25] are used,

$$K(T) = k_0 \exp\left(-E_0/(RT)\right), \tag{6}$$

$$\dot{m}' = \rho_v K(T), \tag{7}$$

where $\rho_v = \rho_c\left(1-\phi_f\right)$ is the density of the multiphase foam and $\rho_c = 1190\ \frac{\mathrm{kg}}{\mathrm{m}^3}$ is the density of the molten polymer at the glass transition temperature [26]. The parameters of the thermal decomposition relation are $k_0 = 10^{12.3}\ \mathrm{s}^{-1}$ and $E_0 = 171.4\ \mathrm{kJ/mol}$ [25]. The evaporation model is strongly coupled to the gas phase chemistry in the bubbles because of the last term in eq (5), which quickly saturates $\frac{p_{v,eq}}{p} \to 1$ and is zero if X_{MMA} does not decrease from the initial evaporation value of one. The following expression for the vapor pressure of MMA in terms of the local bubble temperature T is adopted in this study [27],

$$\log_{10}\left(\frac{p_{v,eq}}{1\ \mathrm{bar}}\right) = 5.3 - \frac{1945.56\ \mathrm{K}}{T - 7.569\ \mathrm{K}}. \tag{8}$$

The conservation equations inside the foam are written in the following form in which the liquid (condensed phase) phase is assumed of constant composition and the mass diffusion in the multiphase foam bubbles is neglected. The

equations differ slightly from what was reported elsewhere [23].

$$\frac{\partial}{\partial x}(\phi_f(\rho_g u_g) + (1-\phi_f)(\rho_c u_c)) = 0 \tag{9}$$

$$\frac{\partial \phi}{\partial t} + u_c \frac{\partial \phi}{\partial x} = (1-\phi)\frac{\partial u_c}{\partial x} - \frac{\dot{w}_c}{\rho_c Y_c} \tag{10}$$

$$\phi \frac{\partial Y_{g,k}}{\partial t} + \phi u_g \frac{\partial Y_{g,k}}{\partial x} = \frac{\left(\dot{w}_c Y_{g,k} + \dot{w}_{g,k}\phi_g - \delta_{g,MMA}\dot{w}_c\right)}{\rho_g} \tag{11}$$

$$\rho c_f = (1-\phi)\rho_c c_c + \phi \rho_g c_g \tag{12}$$

$$\rho u_f c_f = (1-\phi)\rho_c u_c c_c + \phi \rho_g u_g c_g \tag{13}$$

$$\lambda_f = \frac{(1-\phi)\rho_c u_c \lambda_c + \phi \rho_g u_g \lambda_g}{(1-\phi)\rho_c u_c + \phi \rho_g u_g} \tag{14}$$

$$\rho_f c_f \frac{\partial T}{\partial t} + \rho_f u_f c_f \frac{\partial T}{\partial x} = \frac{\partial}{\partial x}\left(\frac{\lambda_f \partial T}{\partial x}\right) - \phi \sum_j \dot{w}_{g,j} h_{g,j} - \dot{w}_c (h_{MMA,l} - h_{MMA,g}) \tag{15}$$

where u is the velocity and the subscripts $_{g,c}$ denote the gaseous and condensed species, respectively, and δ is the Kronecker delta. Two different momentum models were explored inside the foam layer. Model 1 assumed no momentum transfer between the bubbles and condensed region when solving the conservation equations inside the foam, so bubbles were modeled as passing through the liquid without viscous effects. This model will be referred to as the "RhoU" model because the mass flux at each node in the simulation was solved such that $(\rho \times u)_g = (\rho \times u)_c$ at each node point in the simulation. In this first model the condensed species velocity is assumed constant in space and equal to the value at the melting point, which is evaluated by simple mass conservation balance with the solid material mass flow rate. Thus the partial derivative of the condensed velocity u_c is neglected in eq (10). While this model is intuitive, combustion in the multiphase is unsignificant, and the foam additions does not affect the regression rate significantly. The second model, referred to as the "V" model, assumes a bubble driven flow in which the condensed, liquid MMA was forced to move with the speed of the bubbles. The conservation equation in this model used $u_g = u_c$ such that the mass flux of gas and condensed species was not equivalent at every point in the foam layer. The main feature of the latter model is the reduction in the speed of the bubbles in the foam layer near the solid-liquid interface.

Plots of ϕ_f, liquid MMA velocity, temperature, and MMA concentration inside the foam layer are included in figure 8 in order to help the reader better understand the transition zone between the solid and gaseous fuel regions. One can see that the "V" model produces a slightly thicker foam layer in comparison to the "RhoU" model. Even though it can

be seen that condensed species pass through the foam more quickly in 8b, this forces the bubbles to slow down thus allowing the gaseous MMA more time to decompose in comparison to the "RhoU" case where the bubbles can pass unimpeded. It can be seen in figure 8c the foam is able to reach higher temperatures even at the same heat flux to the surface. This further contributes to the decomposition of MMA in the foam layer. The results of the bubble velocity and temperature effects can be seen in 8d where the mass fraction of MMA in the foam layer decreases much more rapidly in the "V" model.

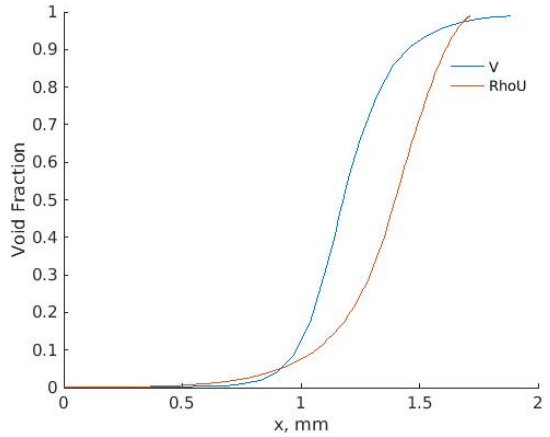

(a) ϕ_f in Foam Layer

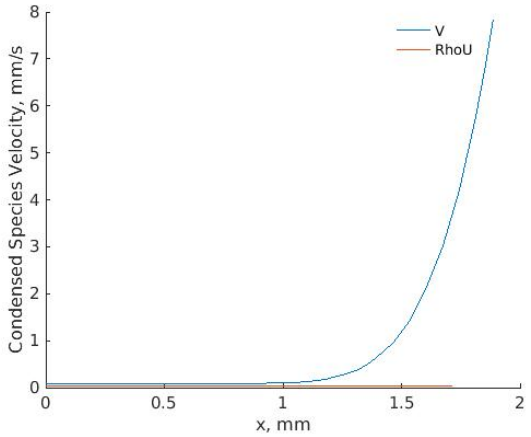

(b) U_c in Foam Layer

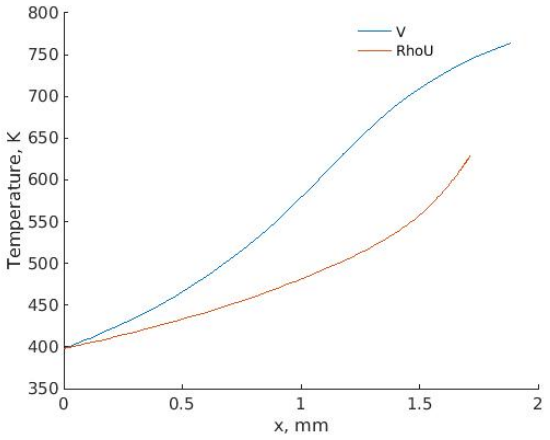

(c) Temperature in Foam Layer

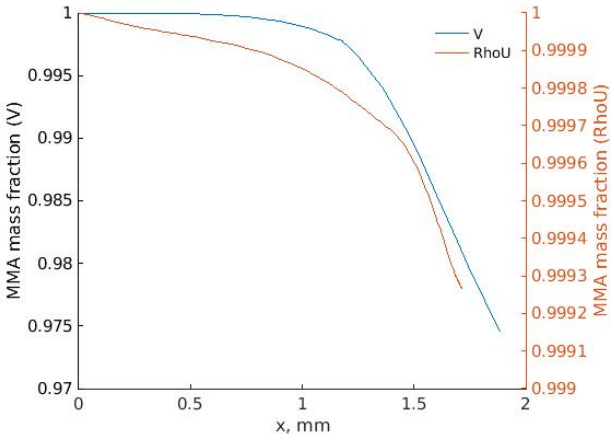

(d) MMA in Foam Layer

Fig. 8 Comparison of two models inside a foam layer with heat flux of 17.38 kW of heat flux applied to surface

The foam region and counterflow flame regions were solved independently. A fixed point iteration method was used to find the foam depth and surface temperature as well as species concentrations and velocities at the gas interface when provided with a given heat flux to the foam surface. This provided a table of values with surface heat fluxes and corresponding fuel inlet conditions for the counterflow simulation which greatly increased run times in comparison

to a fully integrated case. The curves being fitted are the backbone of the integration of the foam model in the LES computations, which are described in Section III.III.E below, and are shown in figure 9. The trends previously discussed in 8(d) still hold at other values of heat flux, or qgas in this case. That is, the MMA mass fraction output is much lower, the temperature is higher, and the thickness is greater for the "V" model at the exit when compared to the "RhoU" model.

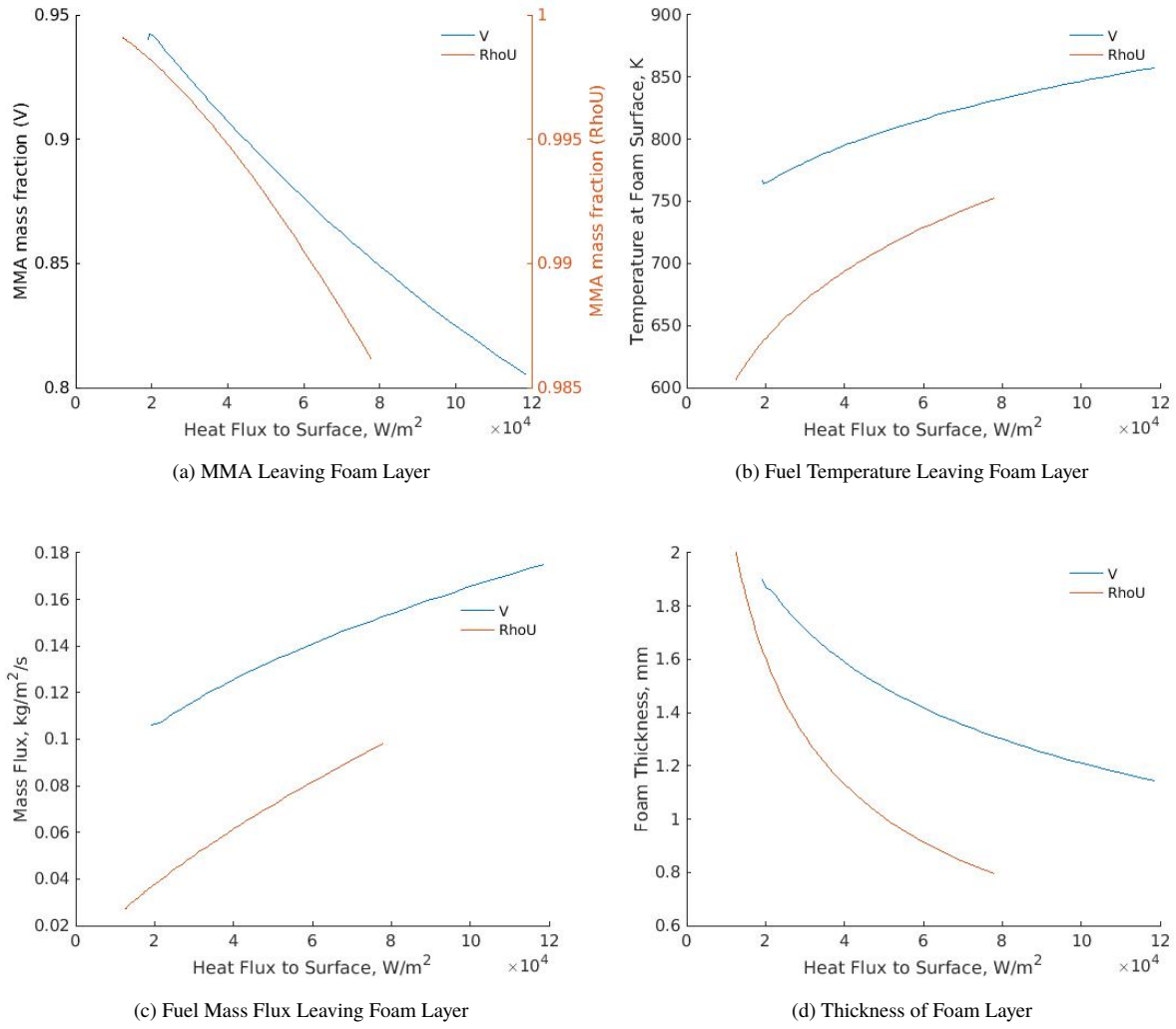

(a) MMA Leaving Foam Layer

(b) Fuel Temperature Leaving Foam Layer

(c) Fuel Mass Flux Leaving Foam Layer

(d) Thickness of Foam Layer

Fig. 9 Fuel inlet conditions as a function of mass flux

1. Effect of Foam parameters on Regression Rate

Because the values of n can vary greatly in MMA due to multiple factors [28], and since the exact value is not well understood for the operating conditions observed in this work, it was assumed to be a constant value throughout the foam. The sticking coefficient s is another parameter that will be set as a constant within the foam layer. This coefficient is the ratio probability of a molecule colliding and sticking to a surface and can thus range from 0-1. A range

of reasonable values were explored for n and s in the counterflow simulations.

Sticking coefficients generally range from 0.1 to 0.5. The true value of the sticking coefficient, like the true momentum transfer within the foam layer, likely lies between these two values. Nucleation density, n, is commonly studied in polymers due to the unique material properties that can be obtained at high void fractions, ϕ_f. Unfortunately, because large void fractions are ideal for these studies and the nucleation density tends to increase with pressure, most research focuses on producing nanocellular bubbles at high pressure and CO_2 air composition [29]. Strong correlation between the pressure and bubble density was found by Wanga et al. [30]; however, the pressure data only extended to pressures ranging from $5.17 - 34.48$ MPa which far exceeds the atmospheric 0.101 MPa produced by the experiment. Nucleation density increases with pressure, and a 6 MPa pressure was shown to correlate to a cell density of roughly 10^6 cells/cm^3, so it can be assumed the nucleation density in the counterflow experiment discussed herein would not exceed this value. An attempt was made using a power law function to estimate the nucleation density at 0.101 MPa, but this predicted a bubble density on the order of 10^{-4} cells/cm^3 which was clearly not the case in this experiment due to the observation of multiple bubbles a foam layer smaller than a cubic centimeter at any given time. Thus, due to the vastly different foaming conditions in the present experiment in comparison to past studies, the nucleation density was estimated using an optical camera to analyze high-speed frames and determine the number of visible bubbles in the foam layer. The high-resolution image analysis leads to a conservative approximation of 2×10^3 cells/cm^3, but due to the location of the diffusion flame and resolution of the camera, a large uncertainty was assumed ranging from $10^3 - 10^5$ cells/cm^3 and sensitivity analysis preformed.

The effect of the variation in regression rate versus the bubble density and the sticking coefficient is shown in figure 10 using the baseline conditions and a volumetric flow rate of air $\dot{Q}$ equal to 2 liters per minute. Note, the diameter of the air feeding tube is 9.41 mm, so the relation between the area-averaged velocity and $\dot{Q}$, expressed in liter per minutes, is $\bar{V} = 0.2397 \times \dot{Q}$ m/s. Laminar plug flow conditions are then applied to evaluate the center-line velocity, which is used in the similarity analysis of the flame-foam system.

Important observations about these plots are that the presence of the foam increases the regression rates, that the sticking coefficient has a stronger effect on the regression rate that the bubble density, and that the high momentum transfer model "V" supports generally higher regression rates than the low transfer counterpart, because of the increase in fuel residence time in the thermal wave.

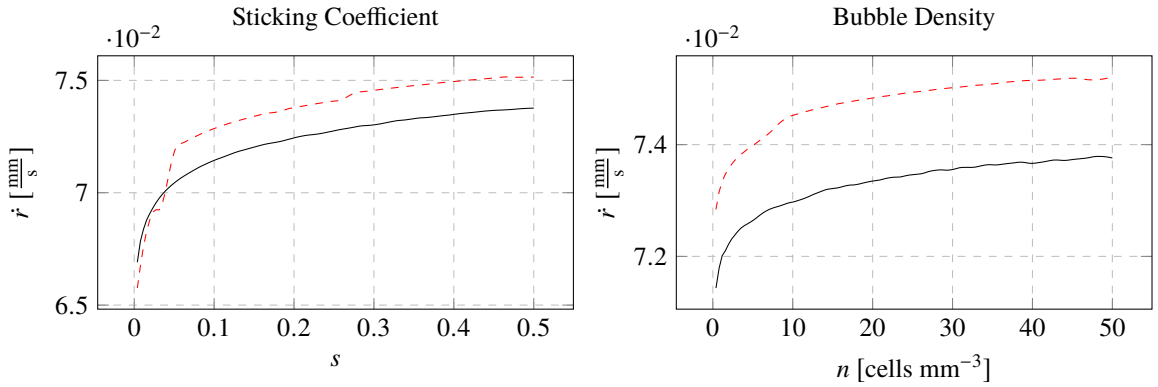

Fig. 10 Effect of foam parameters on the burn rate in nominal counter flow conditions. The left plots has $n = 50\text{mm}^{-3}$, the right plot has $s = 0.5$; legend: ── "RhoU"; - - - "V".

2. Comparison of Regression Rate and Standoff Distance versus Experiments

The foam parameters introduced in the previous section are fixed to $s = 1/2$ and $n = 50$ cells mm^{-3}. The "V" model is used in all computation reported in the following sections. The difference between the two models are small, yet the large momentum transfer model outperforms the low momentum counterpart in all the comparisons investigated, thus it is selected as baseline.

The original and modified mechanism are compared in figure 11. The flame standoff distance is evaluated in the computations as the location of the maximum chemical heat release. The modfied mechanism does a good job in reproducing both experimental data.

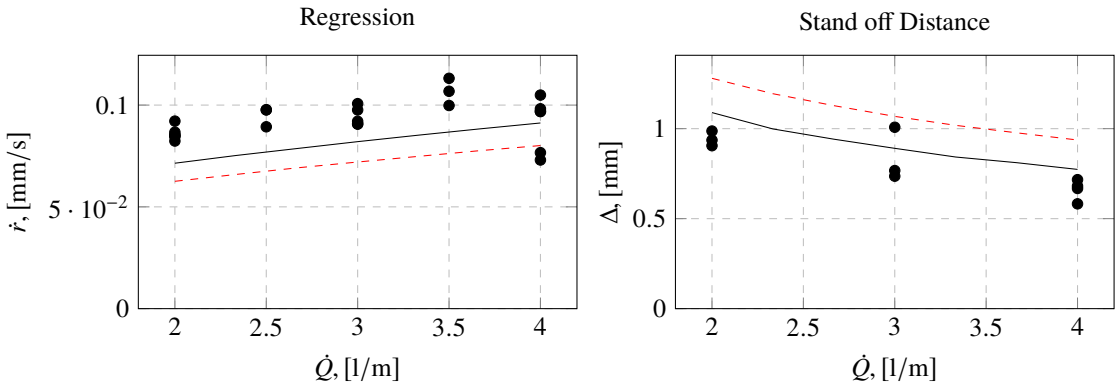

Fig. 11 Validation of mechanism comparing the regression rate and flame standoff distance versus experiments. Legend: ── Modified; - - - Original, (●) Measurements.

The size of the foam-layer thickness is plotted in figure 12. The computations over-predict the experiments by a significant amount, yet the trend vs the air flow is correct. The rationale for the over-prediction is that a metal wire maintains the PMMA sample on the support used in the experiment to push the fuel pellet against the air flow thus

imposing steady burning conditions. The thickness of the foam is measured by analyzing images of the burning sample and selecting the wire position as the solid location (i.e., the glass transition temperature). As the metal dips into the material the size of the foam layer is over-estimated in the experiments. Yet, this figure is important to provide an order of magnitude of the relative size of the foam layer and the flame standoff distance. The foam layer is generally thicker than the flame standoff both in the experiments and the computations. Finally the "V" model supports thicker foam layers and thus agrees with the measurements better than the "RhoU" model.

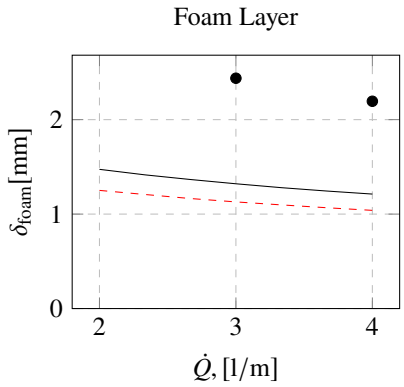

Fig. 12 Effect of air flow rate on measured and computed foam layer thickness. Legend: ── "V"; - - - "RhoU", (●) Measurements.

Finally, the extinction strain rates for different air temperatures are shown in figure 13. As the air temperature increases, the strain rate required to extinguish the flame increases. A high strain rate is representative of a low residence time of the reactants. The increase in air temperature leads to an increase in the reaction kinetics within the system. This reduces the residence time required for the fuel to react, leading to the increase in extinction strain rate with temperature. The values predicted by the model follow the same trend as the experimental data; however, unlike the burn rate and the standoff distance, the predicted values differ from the experimental. The error between experiments and predicted values is likely due to energy losses in the experimental set up. The fuel pellet was held in place by a metal wire that passed over the fuel pellet surface and would have allowed conduction away from the pyrolyzing surface.

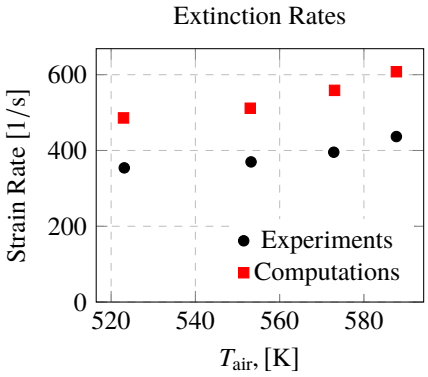

Fig. 13 Experimental vs. numerical results for the extinction rate.

C. Discontinuous Galerkin Model

A novel Discontinuous Galerkin Navier Stokes solver has been implemented to handle complex regressing geometries with coupled heat conduction. The solver is built on top of the SU2 framework [31].

The main drawback of flamelet and progress variable models in high-order discontinuous Galerkin methods is that unphysical pressure oscillations [32] can lead to elevate temperatures because temperature-induced dissociation is not included in flamelet mixing models. This is particularly important in ramjets where the injector/nozzle throat are near/at choked conditions , so the shear layer over the recirculation region is in the compressible regime. Spurious pressure oscillations can become large enough and alter the acoustic field in the ramjet. Thus we develop below a formulation that explicitly includes the heat release and recast it in a weak-form so to discretize it over the discontinuous Galerkin finite element bases. Furthermore, we introduce a caloric equation of state with properties that depends on the flamelet tabulated temperature rather than the local thermodynamic one, to linearize the equation of state.

Momentum and mass continuity are identical to the unreactive case, which can be found (for example) in the work of Pierce and Moin [33]. The energy equation is discretized starting from a conservative formulation in terms of the sensible energy and enthalpy written under the assumption of thermally perfect gases [34],

$$e_{sk} \equiv \sum_{k=1}^{n_s} Y_k \int_0^T c_{v,k}(\tau)\, d\tau + \frac{1}{2}\boldsymbol{u}\cdot\boldsymbol{u} = e_s + e_k. \tag{16}$$

The thermal equation state for the mixture is written in terms of the mass fractions Y and the molar masses W using the ideal gas and Dalton laws

$$p = \rho RT \sum_{k=1}^{n_s} \frac{Y_k}{W_k}, \tag{17}$$

where $R = 8.3145$ J/mole − K is the universal gas constant. The specific gas constant, $R_g \equiv R\sum_{k=1}^{n_s}\frac{Y_k}{W_k}$, is also introduced for future developments.

LES averaging of the energy equation yields

$$\frac{\partial \bar{\rho} e_{sk}}{\partial t} + \boldsymbol{\nabla} \cdot \left(\left(\bar{\rho} e_{sk} + \bar{p} \right) \boldsymbol{u} - \left(\bar{\lambda} + \lambda_t \right) \boldsymbol{\nabla} T + \bar{\rho} \sum_{k=1}^{n_s} Y_k V_k h_{s,k} \right) - \boldsymbol{\nabla} \cdot \left(\bar{\sigma} \cdot \boldsymbol{u} \right) - \bar{\rho} \dot{\omega}_T = 0, \tag{18}$$

where the dissipative stress tensor has components $\bar{\sigma}_{ij} = 2\bar{\mu} S_{ij} + \tau_{ij}$, where $\overline{\overline{\boldsymbol{S}}} = 1/2 \left(\boldsymbol{\nabla} u + \boldsymbol{\nabla} u^T \right) - 1/3 \boldsymbol{\nabla} \cdot \boldsymbol{u} \overline{\overline{\boldsymbol{I}}}$. The subgrid scale tensor is evaluated using an eddy viscosity approach

$$\overline{\overline{\boldsymbol{\tau}}} = 2\mu_t \overline{\overline{\boldsymbol{S}}} - 1/3 \bar{\rho} q_t^2 \overline{\overline{\boldsymbol{I}}}. \tag{19}$$

The parameters of the eddy viscosity model (μ_t and q_t) are evaluated using either Smagorinsky's or WALE approaches. All variables are Favre-averaged but those marked with a bar overhead, to which Reynolds averaging is applied [35]. The heat release term in eq (18) is the product of the net volumetric production rates $\dot{\omega}_k$ and the heats of formation,

$$\dot{\omega}_T \equiv - \sum_{k=1}^{n_s} \dot{\omega}_k \Delta H_{fk}^0. \tag{20}$$

All variables dependent on the chemical state are evaluated using mixture rules where the chemical state is parameterized by scalars transported by the flow Ψ_i, $i = 1, \ldots, N_s$. They are the (Bilger) mixture fraction $\Psi_1 = Z$ [36], the progress variable $\Psi_2 = Y_{\mathrm{CO}_2}$, and the scalar dissipation $\Psi_3 = Z''$. More details on the choice of the progress variable Ψ_2 are provided below in Section III.III.D. The variance is approximated by the LES scaling law $\bar{\rho} Z'' \approx C_V \bar{\rho} \boldsymbol{\nabla} Z \cdot \boldsymbol{\nabla} Z$, with $C_V = 0.5$ [37]. The pressure is not included in the set of independent scalars as suggested, for example, by Nguyen and Sirignano [38] because we find it to be non-important. The rationale is that the probability density function (PDF) underlying the Favre-averaged equations is defined per unit density and the steady counterflow flame features an approximately linear variation of the mass rate of CO_2 production with the density (see Section III.III.D.III.D.1 for details). As a result of this approximation, the main thermo-acoustic feedback contribution in the present non-premixed flame is the heat released by the increased mixing due to the interaction of the pressure with the shear layer, as discussed in the results section (Section IV).

The differential equations for the evolution of the scalars are

$$\frac{\partial \bar{\rho} \Psi_i}{\partial t} + \boldsymbol{\nabla} \cdot \left(\bar{\rho} \boldsymbol{u} \Psi_i \right) - \boldsymbol{\nabla} \cdot \left(\left(\bar{\rho} D_{\Psi_i} + D_t \right) \boldsymbol{\nabla} \Psi_i \right) - \bar{\rho} \dot{\omega}_i = 0, \tag{21}$$

where the turbulent mass diffusivity coefficients are approximated with a constant Schmidt number $\bar{\rho} D_t = \mu_t / Sc_t$, $Sc_t = 1$.

In the flamelet and progress variable approach there are two sources of heating of the gas phase, which are expressed here as $\dot{\omega}_T = \dot{\omega}_P + \dot{\omega}_Z$. The first contribution is due to the progress and it is given here in terms of the net mass

production rate of CO_2 $\dot{\omega}_{CO_2}$ in the mixture,

$$\dot{\omega}_P = -\frac{RT_0}{\rho}\dot{\omega}_{CO_2}\sum_{k=1}^{n_s}\left(\frac{h_k}{RT_0}-1\right)\frac{\partial Y_k}{\partial \Psi_2}/\frac{\partial Y_{CO_2}}{\partial \Psi_2}. \tag{22}$$

The second contribution, the heat release due to a change in mixture fraction, is recast in terms of the second derivative of the scalars. Then using integration by parts we obtain the following source term for the volumetric residual of the DG weak form

$$\dot{\omega}_Z = -\sum_{i=1}^{N_s}\left(D_t + D_{\Psi_i}\right)\left\{\sum_{k=1}^{n_s} RT_0\left(\frac{h_k}{RT_0}-1\right)\frac{\partial^2 Y_k}{\partial {\Psi_i}^2}\right\}\nabla\Psi_i\cdot\nabla\Psi_i, \tag{23}$$

where Ψ_i are the scalars that parameterize the chemistry manifold and D are the diffusivities. The temperature dependency is added to this heat release term by imposing, at first order, that it has the same sign as the difference between the flamelet temperature and the local thermodynamic temperature $T_{\text{flamelet}} - T$. At higher order the dependency on the temperature can be tabulated in a secondary two-dimensional table spanned by the mixture fraction and the temperature deviation $T_{\text{flamelet}} - T$.

A second issue with reactive high order DG methods is that the convergence of the enthalpy to temperature polynomial inversion is typically slow when the temperature exceeds the bounds of validity of the mixture averaged polynomials. We have implemented a variable γ approach that allows to perform flamelet computations in approximately the same computational time as the cold flow, leading to the possibility of analyzing acoustics in full-scale geometries. We define the specific heat ratio based on the flamelet solution as,

$$\gamma(\Psi) = 1 + \frac{1}{R_g(\Psi)}\frac{e_{\text{flamelet}}(\Psi, T_{\text{flamelet}}) - e_0(\Psi)}{T_{\text{flamelet}}(\Psi) - T_0}; \tag{24}$$

thus, we impose that the specific heats are function of the composition and the flamelet temperature. This approach supports a linear variation of the sensible energy with the thermodynamic temperature,

$$e_s \approx \frac{T - T_0}{T_{\text{flamelet}} - T_0}\sum_{k=1}^{n_s} Y_k \int_{T_0}^{T_{\text{flamelet}}} c_{v,k}(\tau)\, d\tau = (\gamma - 1)\left(\frac{p}{\rho} - R_g T_0\right). \tag{25}$$

We find that this approach yields fewer oscillations and is as accurate as the one in which the specific heats are functions of the thermodynamic temperature.

Several test cases have been performed to validate the propose DG-flamelet approach. Simulations were performed using both the Smagorinsky and Wall Adapting Local Eddy Viscosity (WALE) sub-grid scale models. Both two-dimensional and three-dimensional cavity geometries were analyzed.

All equations were converted to the weak integral form before democratizing them on the FEM mesh. The scalar

conservation equation, for example, eq (21) is written below

$$\int_\Omega w\left\{\frac{\partial\overline{\rho}\Psi_i}{\partial t}-\overline{\dot{\omega}}_b\right\}\,d\Omega+\int_\Gamma w\,[\overline{\rho}\vec{u}\Psi_i]\cdot\vec{n}\,d\Gamma-\int_\Omega\nabla w\cdot[\overline{\rho}\vec{u}\Psi_i]\,d\Omega$$
$$-\int_\Gamma w\left[\left(\overline{\rho}D+\frac{\mu_t}{Sc_t}\right)\nabla\Psi_i\right]\cdot\vec{n}\,d\Gamma+\int_\Omega\nabla w\cdot\left[\left(\overline{\rho}D+\frac{\mu_t}{Sc_t}\right)\nabla\Psi_i\right]\,d\Omega=0, \quad (26)$$

where Ω is the volume of a domain (element), Γ is its surface, w is a weighting function b is a general scalar, $\dot{\omega}_b$ is its source rate, D is the diffusivity of the scalar,μ_t is the eddy viscosity, and Sc_t is the turbulent Schmidt number. All terms in this equation are present for progress variable since it is a non-conserved variable. However, as a conserved variable, mixture fraction has a source rate of zero.

Numerical model parameters, such as the viscosity μ and the thermal conductivity λ, are evaluated using mixture rules, thus are functions of the scalar variables. The mixture average transport Wilke's formula [39] has been implemented. The thermal conductivity is evaluated using the following average that considers combination of parallel and serial heat transfers through layers of gas particles [40]

$$\bar{\lambda}=\frac{1}{2}\left(\sum_{k=1}^{n_s}X_k\lambda_k+\frac{1}{\sum_k X_k/\lambda_k}\right). \quad (27)$$

D. Flamelet Library

The flamelet model is integrated into the discontinuous Galerkin method by adding the additional progress variable and mixture fraction terms using a tabulation approach based on third order Bspline basis very similar to that used in the well known Sierra code [41]. Because it is not practical to solve a complete set of equations involving all species and reactions at every point within the domain, a single progress variable, C, is used to track the progress of the flame. In order to obtain a full range of flame values, the counterflow flame was run from adiabatic temperature to the extinction point by varying the distance, L, between the fuel and oxidizer inlets. As this distance was increased, the flame approached the adiabatic temperature, and the flame became extinguished due to strain when inlets became to close together. C in accompaniment with the mixture fraction can be used as independent variables to describe all thermochemical properties, ψ, inside the steady, laminar diffusion flame such that $\psi=\psi(Z,C)$. Many values can be chosen as the progress variable with the main requirement being a monotonic function over all states of the flame from adiabatic to extinction points. As one can see in Figure 14, this work chooses the CO_2 mass fraction, Y_{CO_2}, at flame location because it satisfies the above condition.

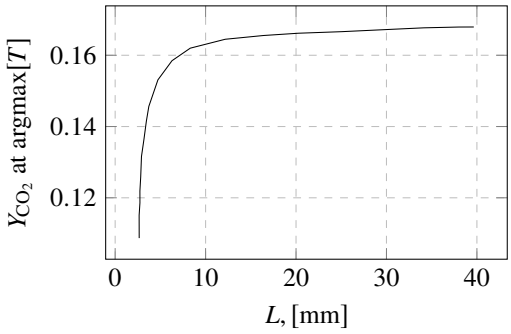

Fig. 14 CO_2 mass fraction at maximum temperature vs distance between inlets, L.

In order to obtain a mapping of the unsteady, extinct values of the 1D flame, the open source code SpitFire [42] was used to evaluate the flamelet values from the extinction point all the way to a totally extinct solution using an unsteady integration method. This is an approximate method of reproducing the unsteady S-curve branch of a flamelet solution that still accounts for a residence time of reacting species and ignition delay time. The extinguished values accounted for approximately 70% of the total progress variable domain.

Once the progress variable was chosen and the tables extended to include extinction values, the temperature, progress variable dissipation, and remainder of the species could be mapped as a function of the mixture fraction, Z, and progress variable, C. C was scaled from $0-1$ using $C = \frac{C-min(C}{max(C)-min(C)}$ such that the independent variables of the library both spanned $0-1$. A visualization of the temperature and scalar dissipation can be found in Figure 15.

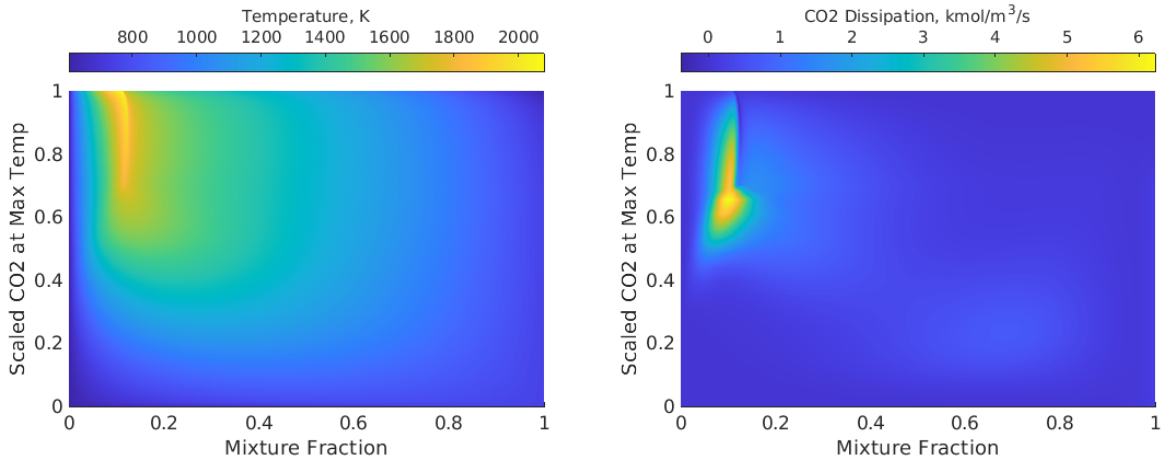

(a) Temperature as a function of (Z, C)

(b) Scalar dissipation as a function of (Z, C)

Fig. 15 Laminar library storage of temperature and CO2 dissipation

In order to account for subgrid fluctuations within the ramjet simulation, a probability distribution function was used inside the LES code. This was extrapolated from the flamelet libraries using SpitFire's library compilation functions. Clipped Gaussian and beta PDFs were explored; however, the distinction between the two was shown to

be negligible inside the full ramjet simulations. Because Z and C are independent of one another the PDF becomes $P(Z,C) = P(Z)P(C)$ which allows one to introduce the mean mixture fraction, $\bar{Z}$, and the mixture fraction variance, $\bar{Z}''^2$, such that the averaged thermochemical properties, $\bar{\psi}$, are a funciton of $\bar{\psi}(\bar{Z}, C, \bar{Z}''^2)$. An example of a Clipped Gaussian distribution is shown in Figure 16 for the readers benefit where the thermochemical properties temperature and CO_2 dissipation were taken as functions of the three independent variables.

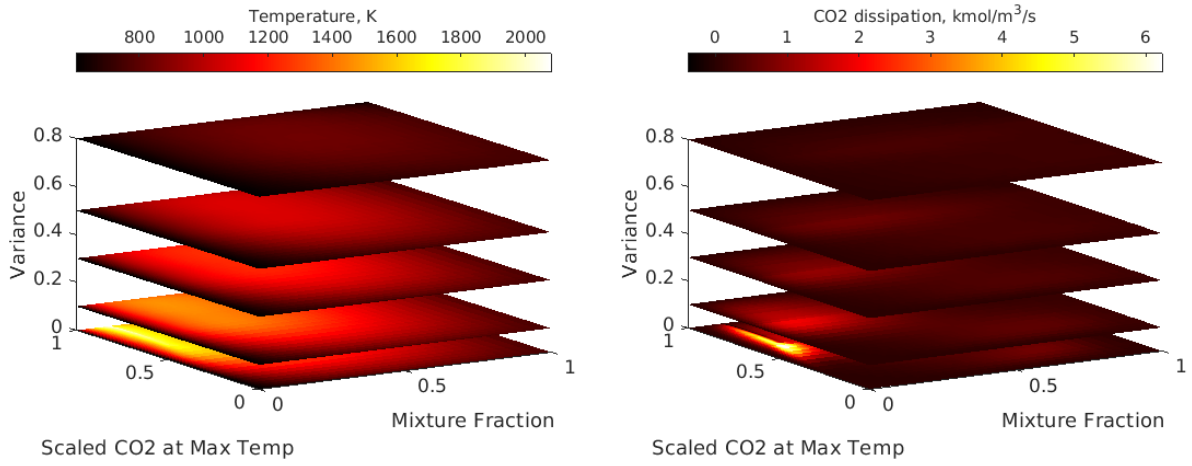

(a) Temperature as a function of $(\bar{Z}, C, \bar{Z}''^2)$

(b) Scalar dissipation as a function of $(\bar{Z}, C, \bar{Z}''^2)$

Fig. 16 Turbulent library storage of temperature and CO2 dissipation

1. Pressure Dependence

The assumption that pressure variation can be incorporated in the linear density factor introduced by the Favre averaging is supported by figure 17, which displays the ratio of the laminar net mass production rate of CO_2 at two pressures divided by the respective densities. The $\frac{\dot{\omega}}{\rho}$ term was evaluated at both one atmosphere and two atmosphere at zero variance using the counter-flow setup. The variable $\frac{\dot{\omega}}{\rho}_{1\text{atm}} / \frac{\dot{\omega}}{\rho}_{2\text{atm}}$ is such that a value of one is obtained if there is no difference between the one atmosphere and two atmosphere libraries. If pressure had no effect at all on the library's contribution to the flamelet simulation, one would expect to see a value of one at all locations; however, it can be seen that this is not the case. A large portion of the domain displays values close to one, but the domain associated with extinction/ignition as well as the region very close to the fuel grain displays discrepancies. In the current study, this ratio was assumed to be one everywhere such that the pressure had not effect on the scaled mass production $\frac{\dot{\omega}}{\rho}$ term. However, future work will explore the incorporation of an additional dimension to the manifold governed by the independent variable pressure, p.

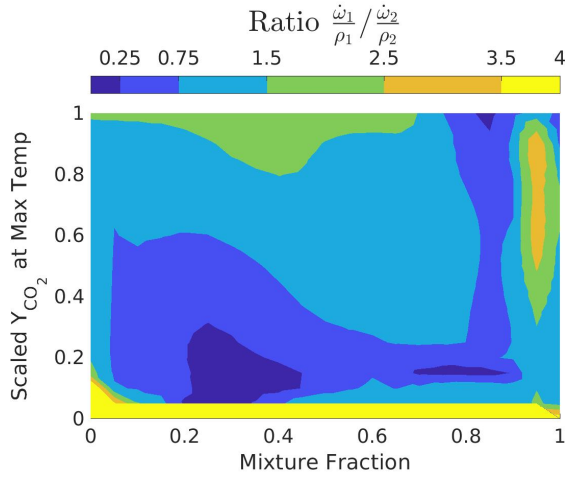

Fig. 17 Ratio of mass production to density at zero variance in the PMMA-LES flamelet model.

E. Burning Boundary Conditions

Burning boundary conditions in the LES at the fuel walls are derived from the counterflow diffusion flame model by matching both diffusive and convective fluxes against the foam layer counterparts. A fully coupled approach is described based on the assumptions of steady one-dimensional thermal field in the foam layer.

Conservation of both the convective and diffusive fluxes at the burning interface and the assumption that species diffusion is not important in the foam layer [43] lead to expressing the regression rate, the mass and energy flux at the interface in terms of the conductive heat flux $q \equiv -\lambda \partial T / \partial n$ evaluated at the boundaries of the simulation domain (the normal $\vec{n}$ points outside the fluid domain). The wall regression model is clearly non-linear due to the variation of the surface temperature with the regression rate. The relationship between heat flux, regression rate, and surface temperature at the foam-gas interface is plotted in figure 18.

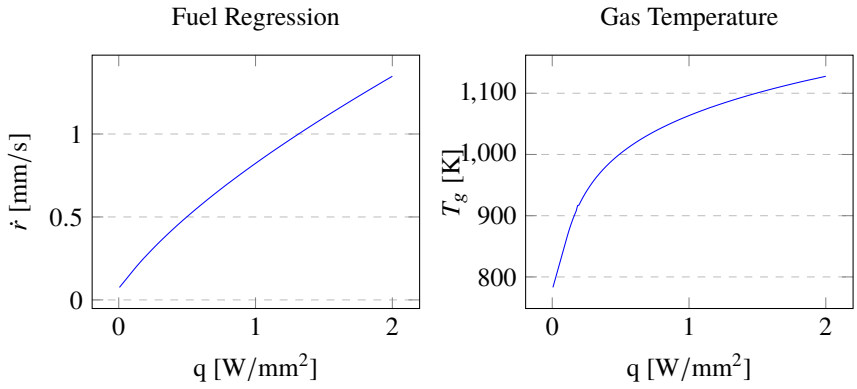

Fig. 18 Foam layer solid decomposition model.

IV. Results and Discussion

A comparison of the predicted cavity regression rates against the experiments suggests that the present model compares well with the experiments for the shallow cavities analyzed by Gallegos and Young [5]. Such a comparison has been discussed previously by Pace [44] and Gallegos et al. [6] and it is not shown here for brevity sake. Therefore, only acoustic results are discussed in this section.

The grid and boundary conditions for the ramjet simulation are summarized in figure 19.

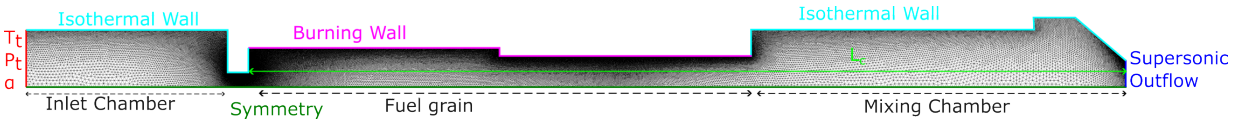

Fig. 19 Schematic of the boundary conditions for the Ramjet simulations.

The cavity lengths investigated are 51 mm (2 in), 152 mm (6 in) and no cavity. The deep cavity configuration analyzed in the experiments [5] is considered. Total conditions of $P_t = 0.47$ MPa, $T_t = 548$K, $\alpha = 0$ (AOA) were imposed at the inlet, and the exit was specified as an exhaust with atmospheric back-pressure. The flow is choked in burning conditions so the value of the back pressure is unimportant and the outflow boundary is marked as supersonic outflow. Isothermal walls with prescribed temperature equal to $T_w = 300$K were used for the non-burning boundaries. Insignificant differences were evaluated when using adiabatic boundaries in this research. For improved accuracy at a given resolution, 3rd order finite element grids were used, constructed using the python API of GMSH [45], leading to a fourth-order accurate DG solution. For each 2D geometry three meshes with progressively smaller spacing were analyzed. The corresponding element numbers are 31,497, 90,450, and 141,155, respectively. All elements are 10 nodes triangles, Triangle-10. All computations discussed here were obtained with the finest grid. The number of degrees of freedom on the finest grid is 1,411,550. The numerical error assessment was performed in a companion study [6] and it is not repeated here.

A. Cold Flow Analysis

1. Spectra

The experimental cold flow spectrum for the 152 mm (6-in) cavity case is shown in figure 20, which is evaluated at a location on the axis of the ramjet and distance $x_0 = 0.55$ m from the left wall of the inlet chamber as shown in figure 3. The other cavity cases have similar features [5], with a low peak around three times the acoustic fundamental frequency $f_0 \equiv \frac{\sqrt{\gamma R T_t}}{2L_c}$ and higher frequency peaks at 10 f_0, 15 f_0 and multiples of 10 of the fundamental frequency. Here, the chamber length L_c is evaluated as the sum of the grain and mixing chamber axial extensions.

The main focus of the cold flow computational analysis has been to understand the gap between the low frequency peaks $f/f_0 = 2-5$ and the higher frequency peaks $f/f_0 = 15-30$ and why they do not change with the cavity shape.

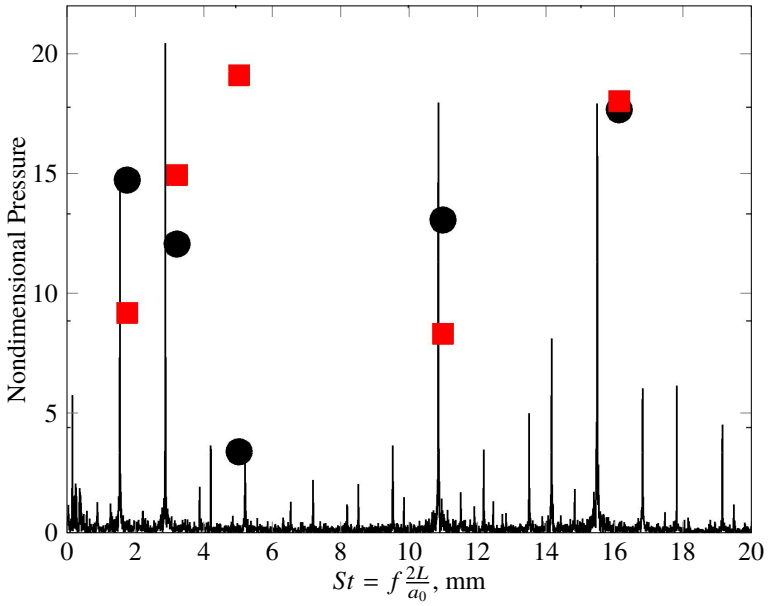

Fig. 20 Comparison of power spectra of cold flow LES simulations against measurements for the 152 mm cavity ramjet. Smagorinsky (●), WALE (■), experiments (——).

Both the Smagorinsky and WALE subgrid scale models were able to reproduce the dominant acoustic frequencies found in the ramjet experimental data in both the magnitude of the perturbation and their associated frequency, with the exception of the peak around 10 f_0. In general, the cold flow analysis showed that Smagorinsky's model leads to a better agreement versus the experiments, and it has been used in the combustion analysis.

A comparison of the pressure spectra for the three ramjet configurations (152 mm, 51 mm, and no cavity) is shown in figure 21. There are two main modes in cold flow that closely resemble the experimental ones, ($St \equiv f/f_0 = \{3, 18\}$) and their frequency appears to be invariant to the cavity configuration.

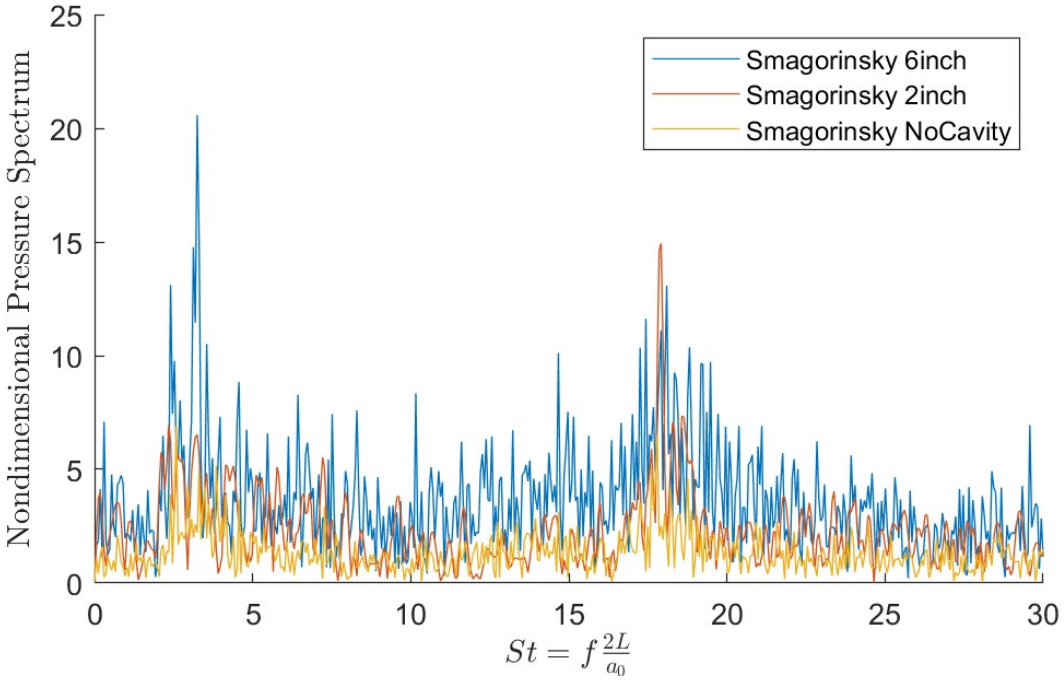

Fig. 21 Comparison of acoustic energy spectra for different cavity lengths using cold flow LES.

2. SPOD Analysis

To determine the origins of the acoustic signals observed in the PSD plots, Spectral Proper Orthogonal Decomposition (SPOD) is used. SPOD extracts structures (modes) in a flow that are coherent in space and time. Each mode is an eigenvector λ of a Cross-Spectral-Density (CSD) at each frequency [46]. Unlike the original SPOD code, the SPOD code in this report scales the modes by the time window over which they were calculated, allowing the modes to be determined in terms of signal power instead of energy. The signal used for SPOD is p/p_0 where p is the pressure at a given point in the cavity and p_0 is the inlet total pressure. The mode acoustic energy and its spatial distribution $\hat{p}_m(x, r)$ are subject to the integral constraint

$$\int_\Omega r\hat{p}_m(x, r)\,\mathrm{d}x\,\mathrm{d}r = 1, \tag{28}$$

with Ω a two-dimensional slice of the fluid domain with fixed azimuthal angle.

The SPOD modes corresponding to the peaks of the power spectrum are shown in figure 22. The first peak corresponds to a longitudinal mode associated to the chamber fundamental harmonic (with length scale L_c). The second is characterized with radial fluctuations in the mixing chamber and features the maximum radius of the ramjet as its scaling length. Therefore, the SPOD was successful in explaining the split between high and low frequency pressure perturbations in the mixing chamber observed in the experiments, by attributing to a split between axial and radial acoustic modes. Intermediate frequency peaks appear to be from cavity modes which have both longitudinal and radial

components. The SPOD analysis thus identify a complex mechanism of excitation of the acoustic in the cold flow analysis, with the horizontal modes bouncing off the mixing-chamber inclined aft wall and reflecting in a combination of radial and longitudinal modes.

The addition of the flamelet model (combustion simulations) appeared to shift SPOD modes to higher frequencies. This can be attributed to the increased temperature within the combustion chamber, which in turn increases the speed of sound. These modifications will be discussed in more details in Section IV.IV.B.

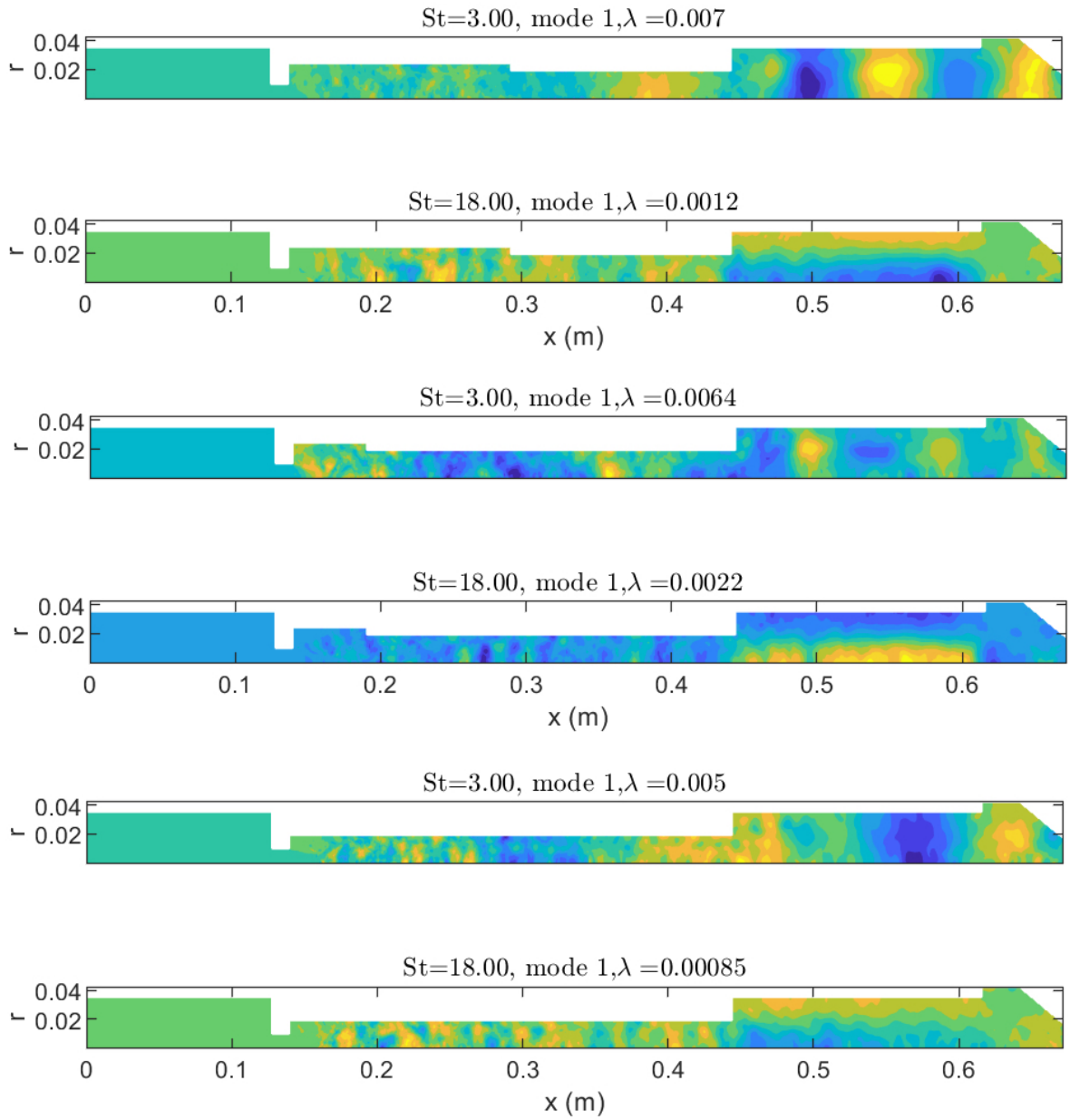

Fig. 22 Cold flow SPOD modes for Smagorinsky and 3 cavity lengths: 152 mm, 51 mm, and no cavity.

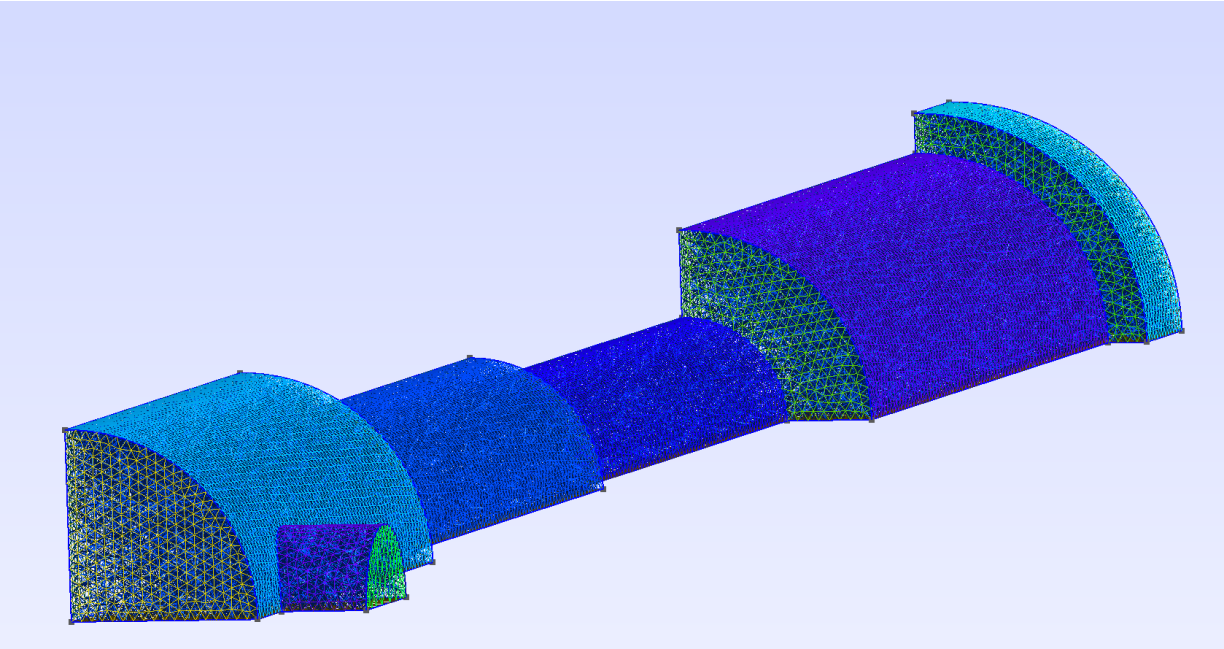

Fig. 23 Three dimensional grid

A comparison between the WALE (not shown) and Smagorinsky models revealed that the SPOD modes are very similar in both distribution and intensity. The WALE model had lower dissipation, which makes the SPOD contours more sharp, however it was also more susceptible to numerical instability due to the shocks at the injector in the cold flow analysis. As a result, less data was collected with the WALE model than with the Smagorinsky model.

3. Three dimensional Effects

Three-dimensional effects are associated with two contributions. First the intakes in the inlet chamber seen on the left side of the computational model in figure 23, second the compressible shear layer is affected by non-axisymmetric, azimuthal instability modes. A three-dimensional view of the quarter-space grid used in the cold flow LES is shown in figure 23, which clearly shows the intake ports in the left. To assess the significance of swirl modes in the 3D simulation, an azimuthal Fourier transform was used. To calculate this, pressure data from the 3D grid was interpolated to a regular x-r grid at θ increments of 2°. The Fast Fourier Transform algorithm was then applied along the θ dimension to produce a single FFT at each point on a 2D x-r grid. AFFTs (azimuthal Fast Fourier Transform) of snapshots across a range of approximately 20 ms have been collected thus far. The results are plotted below in figure 24. As expected, the magnitude of the 0 rev^{-1} mode, which is analogous to the mean, has p/p_t values close to 1. The maximum value in higher ref^{-1} modes quickly decays, with just 0.04 at $1rev^{-1}$ and 0.001 at $3rev^{-1}$.

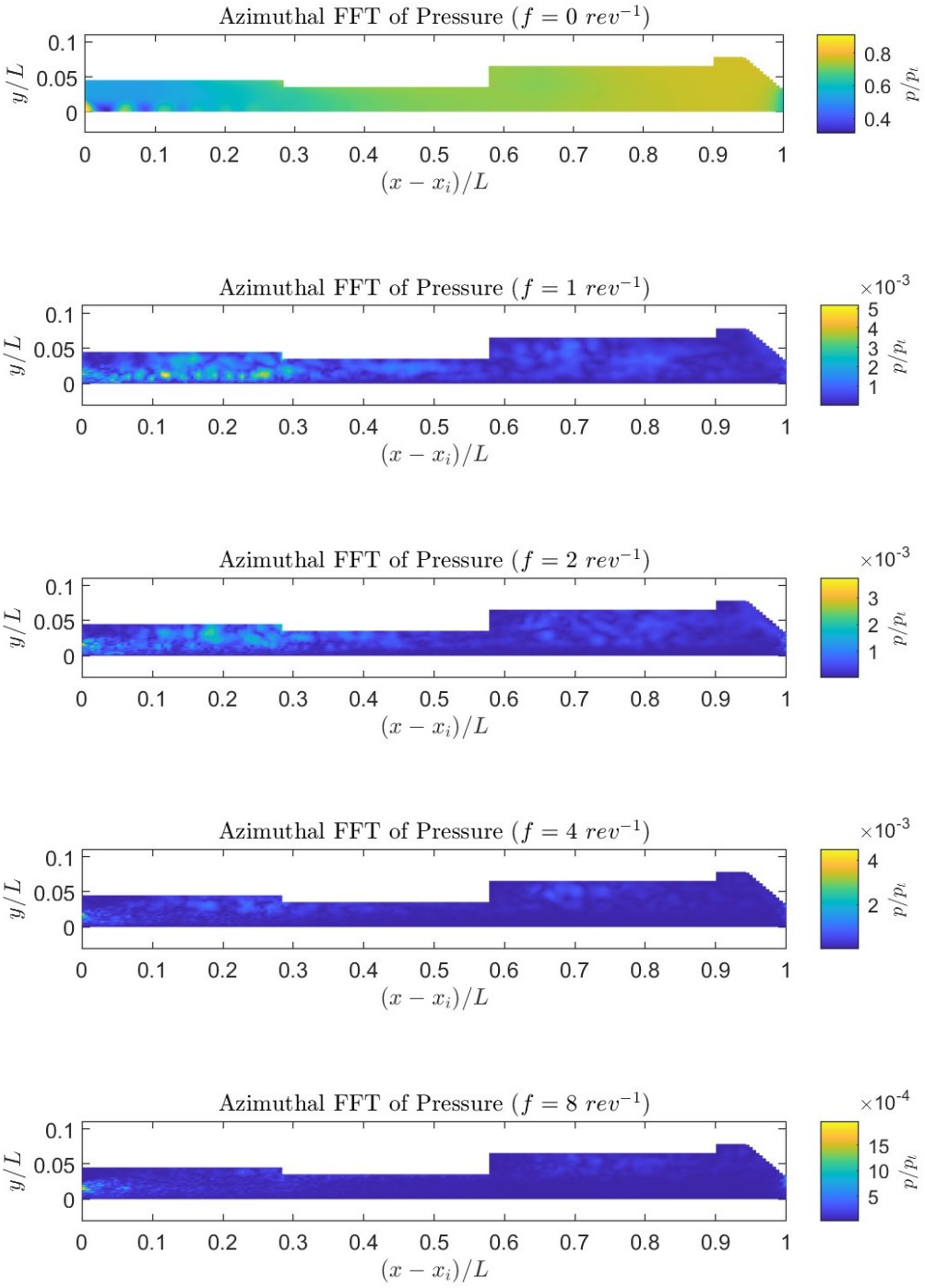

Fig. 24 Azimuthal Fourier Transform of Pressure in Cavity for Cold Flow Ramjet.

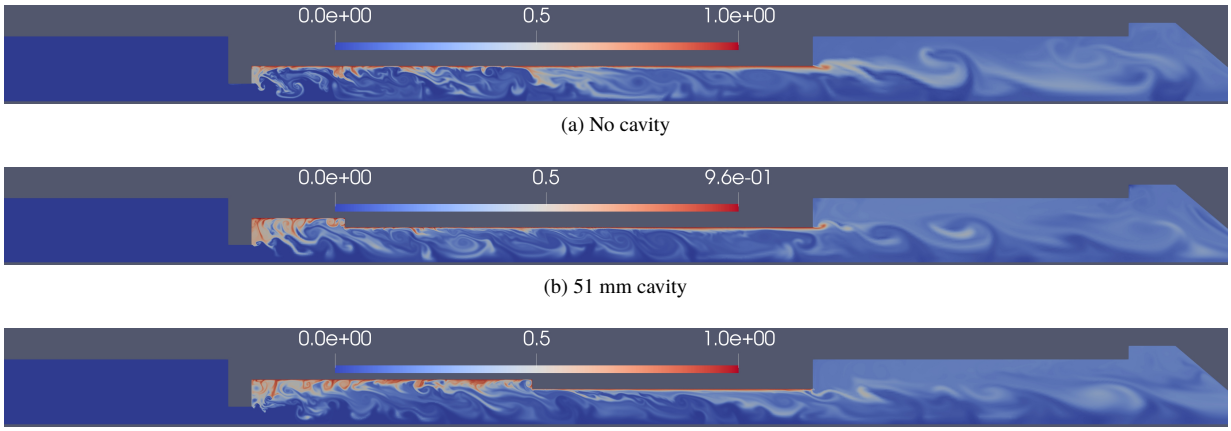

(a) No cavity

(b) 51 mm cavity

(c) 152 mm cavity

Fig. 25 Mixture fraction in the LES simulations at an instant in time during the statistically stationary evolution.

B. Hot Flow Analysis

Based on the cold flow analysis it was determined that three-dimensional effects contribute marginally to the acoustic field and that the Smagorinsky subgrid model performs better than the WALE model in matching experimental data. Thus, the hot flow simulations were performed with the Smagorinsky subgrid model and with a two dimensional axial symmetry, with the implicit assumption that coherent azimuthal modes have a week effect on mixing and combustion.

A snapshot of the mixture fraction for the three configuration under investigation no-cavity, 51-mm (2−inches), and 152−mm (6−inches) cavity is shown in figure 25. The cavity increases the recirculation region and supports a low speed mixing region near the fuel surface.

1. Validation

The mean chamber pressure sharply increases during hot runs (with combustion) reducing significantly the injector Mach number and lowering the shear layer convective Mach number. These phenomena affect the fluid dynamics and acoustics in the mixing chamber. The mean pressure in the ramjet is compared to the experiments in figure 26. The computations agree well with the experiments. The experiments cannot support ignition without a cavity, while the computations can, mostly because of the well known shortcomings of the progress variable model near extinction point [47]. The computations predict a strong decrease of the chamber pressure without cavity, but the computations are highly unstable and extinction was obtained when initializing the simulations directly from the cold flow. The instability manifests itself with higher values of harmonic modes of the fundamental near the inlet, which will be discussed in the next section.

The power spectral density of the signal at the same location as the cold flow (see Section IV.IV.A.IV.A.1) is plotted in figure 27 as validation of the unsteady pressure coupling. The simulations reproduce the main fundamental peak well,

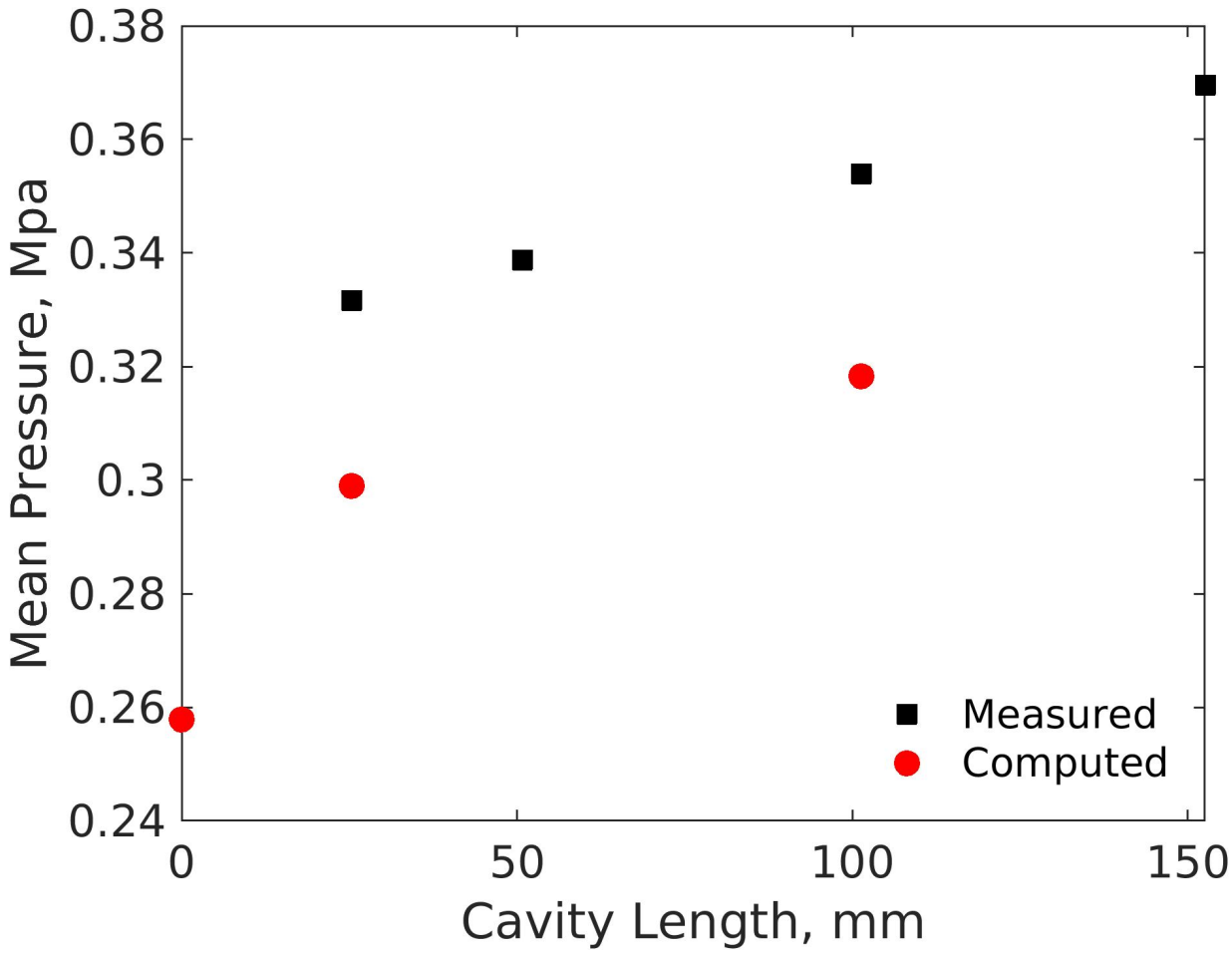

Fig. 26 LES mean pressure compared to the experiments

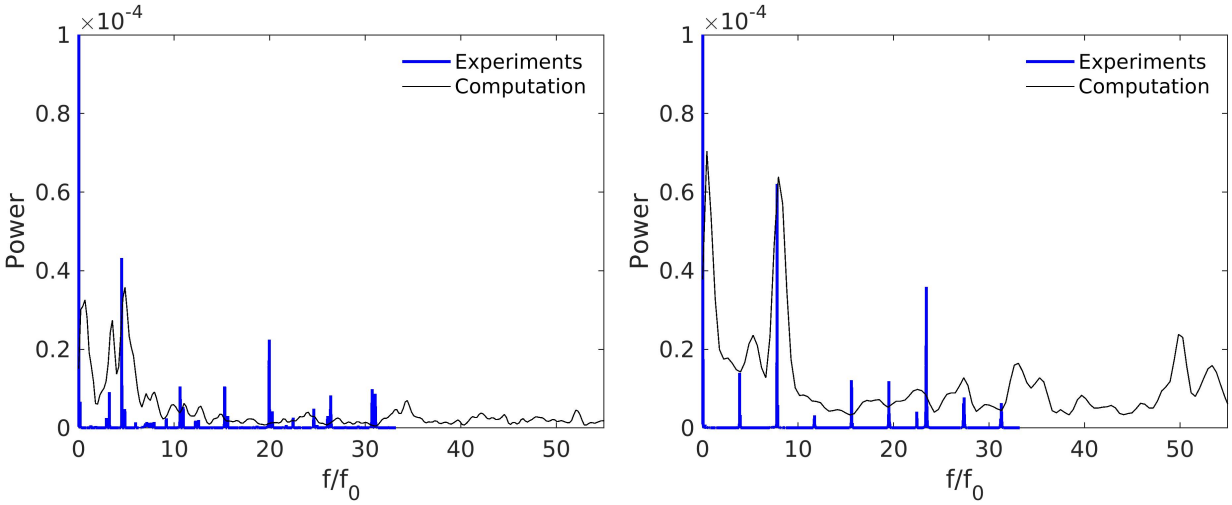

(a) 51 mm cavity

(b) 152 mm cavity

Fig. 27 Power Spectrum for hot flow simulation of the ramjet for two cavity configurations.

which has shifted to a higher frequency ($f \approx 5f_0$) than in the cold flow case because of the increased value of the speed of sound with the increased gas temperature. The simulations perform poorly in reproducing the high-frequency modes, which, instead, were well predicted in the cold flow simulations. These modes with $f/f_0 \approx 20$ represent radial waves induced by the angled aft wall of the mixing chamber. The increased frequency of the acoustic modes for the 152 mm cavity is a consequence of the higher fuel flow rate, which increases the temperature near the axis where the pressure probe is located.

2. Modal Analysis (SPOD)

The experimental work noticed that the cavity supports isolated low frequency modes as shown in figure 28. Larger cavities support a modes split while smaller cavity support a single mode. The main objective of this section is to investigate these modes and determine if they are important to flame holding.

The non-dimensional SPOD modal energy Λ is plotted for the three cases in figure 29. There are two main differences between the burning and non-burning modal distributions. First, the cavity cases show the presence of low frequency modes, which are indeed similar to what was observed in the experimental campaign. Second the no-cavity case supports significantly higher energy at higher frequency with distinct peaks that have frequencies equal to 3/2 the fundamental. A more in depth investigation of the modes at low frequencies is shown in a set of figures depicting the modal energy distribution (the absolute value of the SPOD modes) in figures 30-32. Here the distribution is plotted for the peak frequencies in the spectral energy norm Λ. The last two modes (bottom panels) in each of the figures are clearly acoustic modes based on the interaction between the nozzle and the shear layer in the middle and the scaling between wavenumber and frequency which indicates a constant propagation speed. They are expected to scale with the

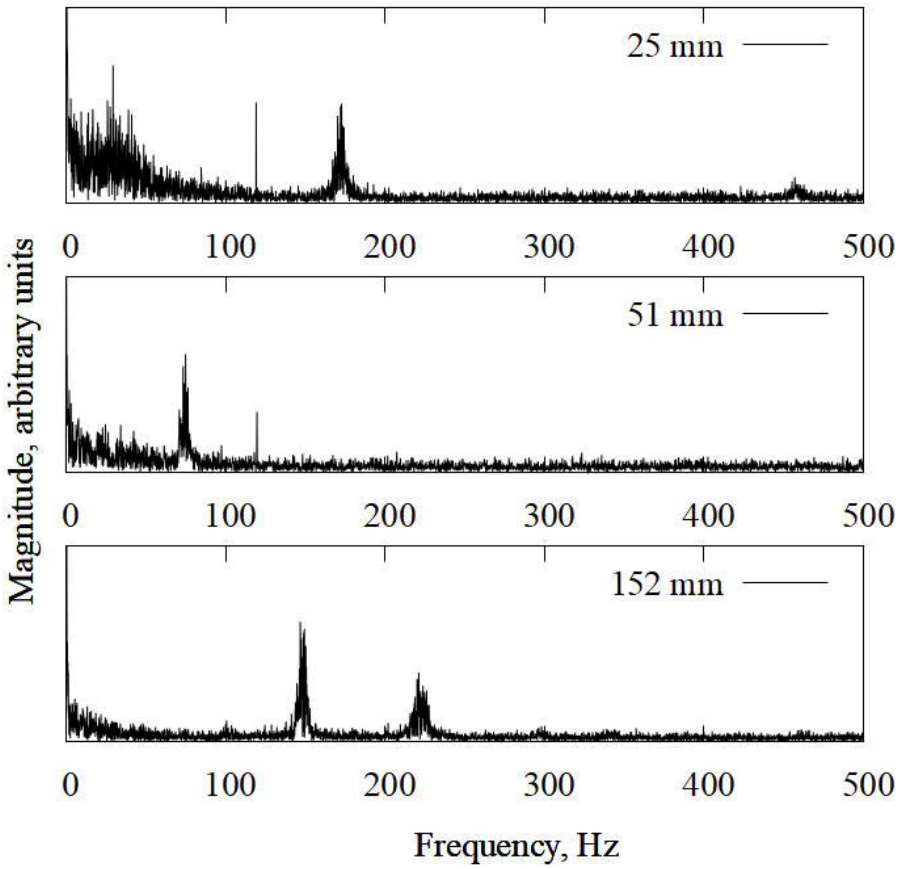

Fig. 28 Measured dominant pressure modes in deep cavity ramjet combustion, energy spectrum.

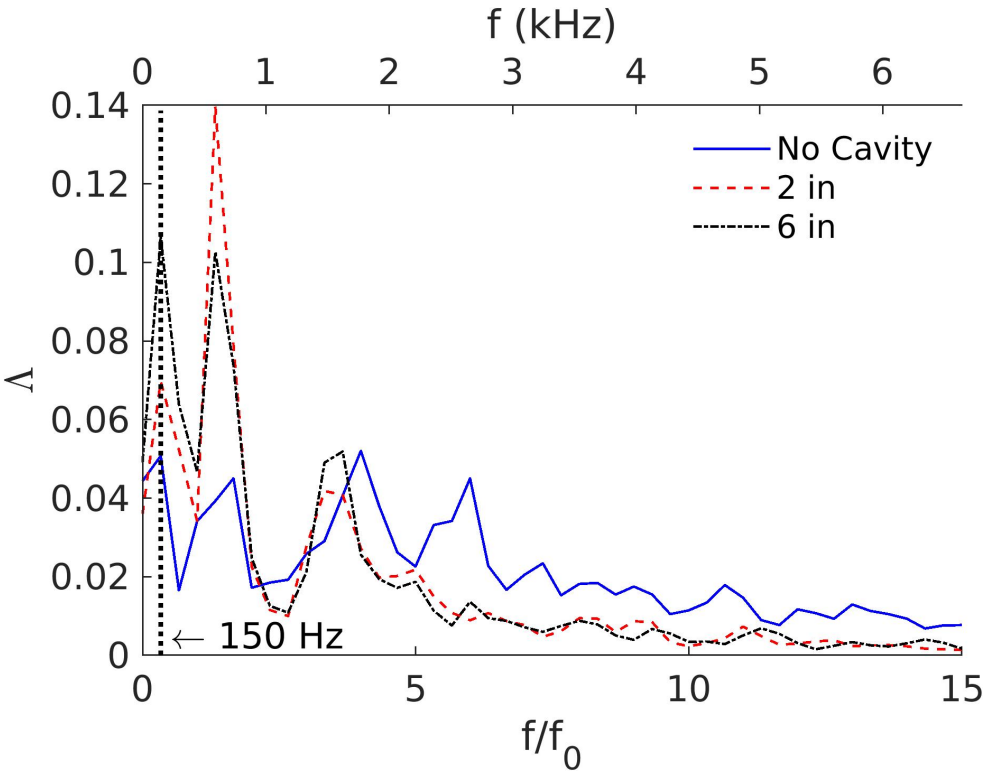

Fig. 29 SPOD modal energy Λ from the LES simulations.

chamber length L_c. The energy distribution of these modes also indicates that interaction between the shear layer region and the downstream nozzle in considerably smaller in the 152-mm (6−in) and slightly smaller in the 51-mm (2−in) case when compared to the no-cavity baseline. Multidimensionality in the cavity appears to remove energy from the acoustic interaction between nozzle and shear layer.

The first two modes, the low frequency peaks in figure 29, are not supported by an interaction with the nozzle, based on the mode energy distribution; they are sub-harmonics of the fundamental, and are concentrated near the injector throat area. In the cavity cases, the low frequency modes are supported by the interaction between the cavity and the injector, which leads to the slow vortical pressure fluctuations of the injector flows. Figure 33 shows the formation of strong compression waves due to the slow movement of the recirculation region shown in figure 34, where the axial momentum $\rho \boldsymbol{u} \cdot \hat{i}$ is plotted near the injector throat region.

The magnified pressure fluctuations at this location are due to the fact the Mach number is almost one at the injector throat (for quasi 1 D isentropic flow $dp/p = \gamma dA/A \frac{M^2}{1-M^2}$), and a weak shock is evident in the lower part of figure. Therefore, the low frequency pressure fluctuations are focused in the injector region. Moreover, the presence of the cavity augment self-excited pressure oscillations that emanate from the upstream wall of the injector and have a vortical wavemaker in the recirculation zone.

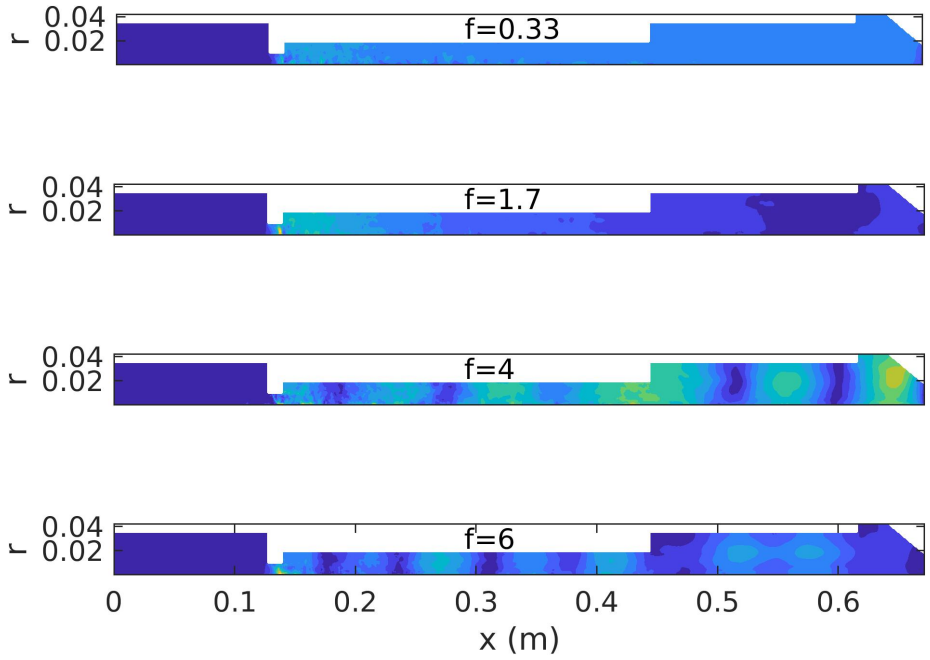

Fig. 30 SPOD energy distribution for the no-cavity LES simulation.

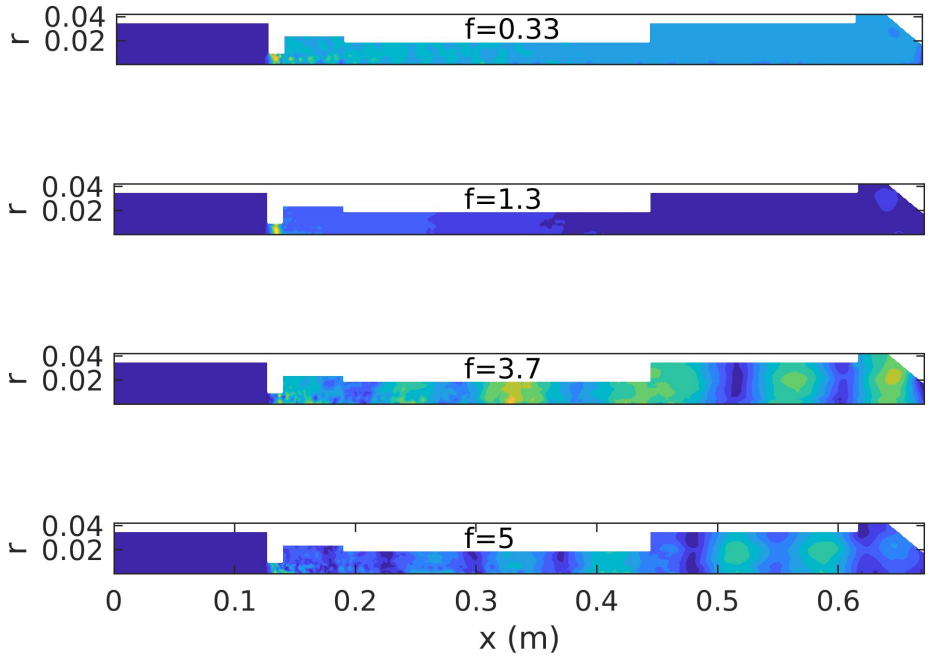

Fig. 31 SPOD energy distribution for the 51 mm (2−in) LES simulation.

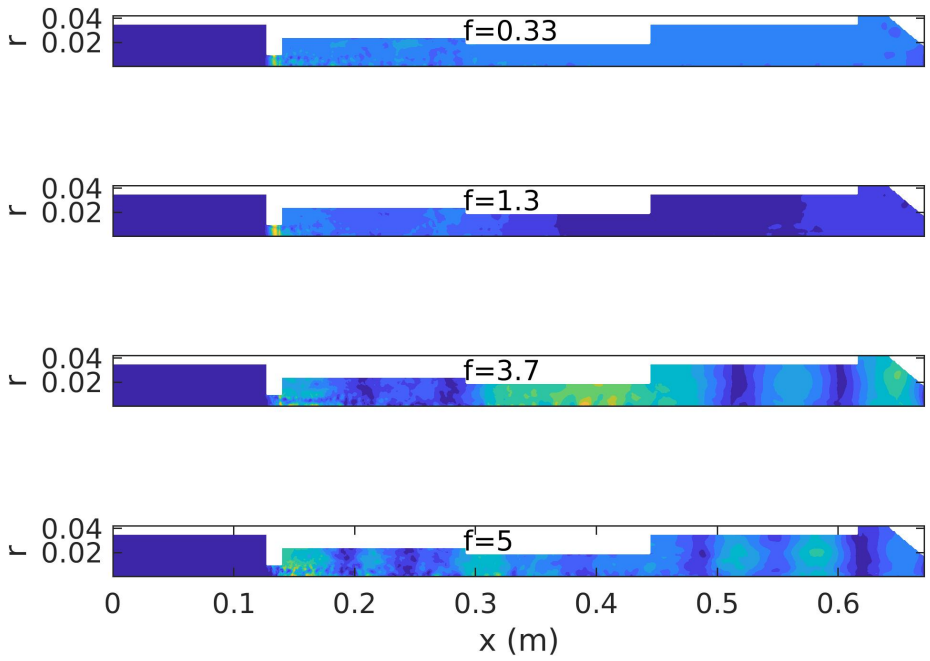

Fig. 32 SPOD energy distribution for the 152 mm (6–in) LES simulation.

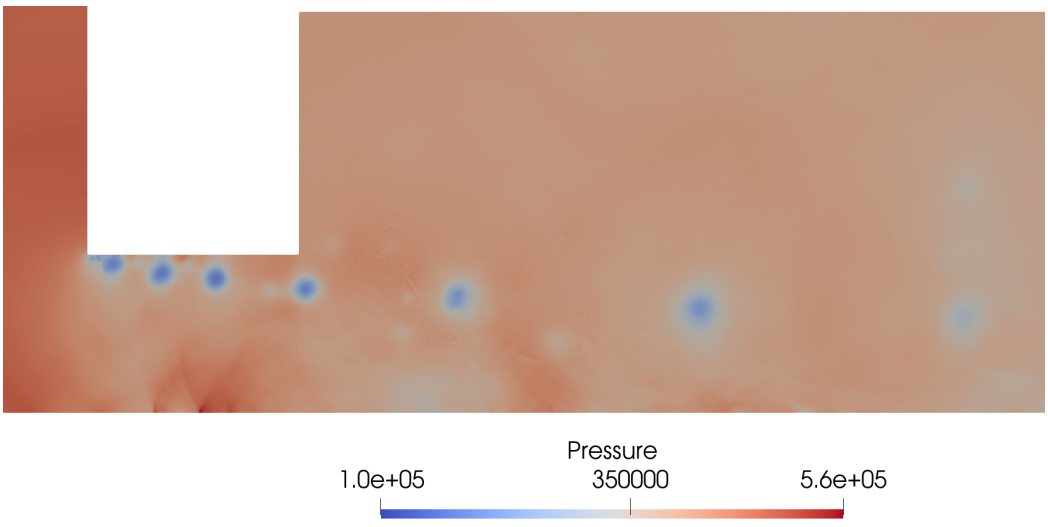

Fig. 33 Vortical pressure fluctuation at the injector of the 152-mm (6–in) LES simulation.

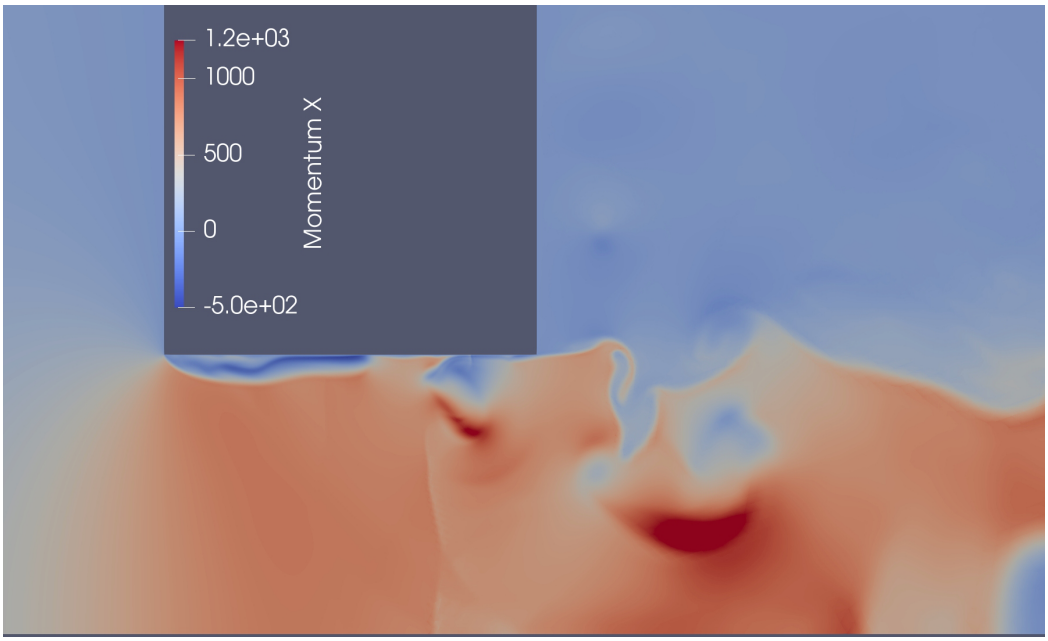

Fig. 34 Recirculation region near the injector (throat) of the 152-mm (6−in) LES simulation. Note this figure has a narrower view than the pressure analog figure 33.

3. Discussion

The important issues that should be addressed are: i) if the increase in the chamber fundamental and 3/2 harmonic mode affects (negatively) the no-cavity burning and ii) if the contribution of the sub-harmonic modes affects (positively) the combustion in the two cavity cases. The increase in the chamber harmonics leads to a non-linear interaction of the pressure waves and frequency doubling terms as its consequence, which explains the larger magnitude of the high-order harmonics in figure 29 for the no-cavity case. Based on the analysis of the power spectra in near the injector, we conclude that the non-linear interaction leads to a disruptive instability that limits the operational range of the solid fuel ramjets. Regarding the second point, the simulations indicate that the low frequency mode do not have a positive effect on the cavity burning because the magnitude of the low frequency pressure oscillation modes in the cavity is small. The pressure power spectrum at a fixed point on the burning fuel wall at the distance of 25 mm from the throat is plotted for the three cases in figure 35. It can be noticed in this figure that the pressure oscillation for the non-cavity case are significantly larger than in the cavity cases. The both the second and the third harmonics are significantly stronger than in the cavity cases indicating non-linear interaction. Instead harmonics of the low frequency (vortical) mode do not appear to be as important.

V. Conclusion

The present combined numerical and experimental study makes two contributions to the understanding of combustion in solid fuel ramjets: i) the validation of a new model for PMMA combustion and its coupling to high-order LES

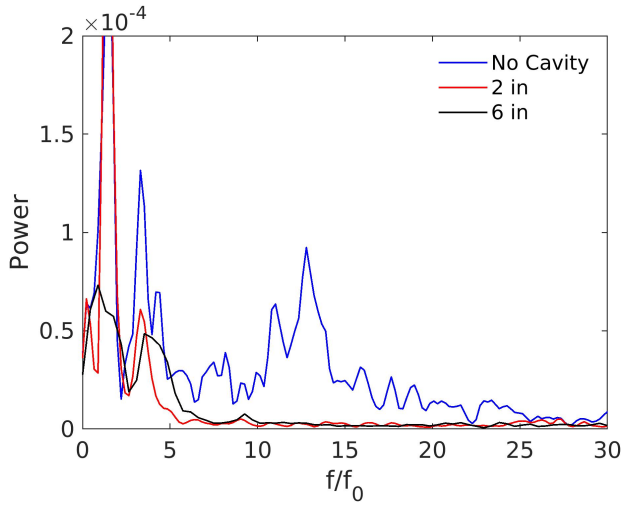

Fig. 35 Comparison of pressure power spectrum at a point on the propellant wall at 25 mm from the injector.

simulations, and ii) the determination of how flow modifications supported by non-standard (cavity) geometries affect acoustics and flame-holding. The validation study compares the combustion of PMMA under laminar counter-flow conditions to a numerical model of combustion for a self-similar stagnation flow. The numerical model includes a melting foam layer model for the PMMA that allows fuel evaporation and decomposition through the presence of bubbles observed experimentally. This decomposition prior to the fuel reaching the oxidizer hastens the regression process. The simulations were able to accurately predict the fuel regression rates, and it was found that the model predicts the maximum flame temperature with reasonable agreement. The simulations predict accurately the effects of mass flux on flame standoff distance and to a less extent the extinction rates. The combustion and foam model demonstrates high fidelity in comparison to experimental work whereas latent heat solid model (without foam) failed to capture the significance of the diffusion flame in a counterflow burner with a stagnation point very close to one of the inlets. The comparison of experiments and computations identifies the effect of momentum transfer between bubble and condensed phases on the burning rate using a simple argument. The melt layer contributes to combustion by increasing residence time of the gas in the thermal wave, which accelerates the thermal decomposition of the MMA fuel. The melt layer thickness is of the same order as the flame stand off distance and decreases with the heat flux while being substantially unaffected by changes of pressure.

The combustion developed in one dimension was applied to the prediction of the cavity acoustics in a asymmetric model of the ramjet with burning but not regressing walls. Cold-flow LES simulations show that there are two dominant acoustic modes ($St \equiv f/f_0 = \{3, 18\}$) in the ramjet and their frequency appears to be invariant to the cavity configuration. The first peak corresponds to a longitudinal mode associated to the chamber fundamental oscillations (with length scale L_c). The second is characterized with radial fluctuations in the mixing chamber and features the maximum chamber radius of the ramjet as its scaling length. Mixed (radial and axial) modes in the intermediate frequency range reveal the

effect of a slanted aft wall on the acoustics. Three-dimensional cold flow simulations predicted weak non-symmetric (azimuthal) modes.

Hot-flow simulations show a substantial increase in the mean chamber pressure with the addition of the cavity, indicating that it enhances flame-holding in solid-fuel ramjets, in agreement with the experiments. The analysis of the ramjet acoustic modes shows the emergence of low frequency modes in the cavity cases, in agreement with the experiments. Using SPOD, these modes were associated with low frequency breathing of the recirculation region at the nozzle throat. Perturbations are localized in the throat region because of the Mach number pressure scaling. These modes do not seem to affect the pressure fluctuation and thus combustion in the chamber. Together with the emergence of low frequency vortical modes, the cavity supports a decrease in the high-wave number harmonics of the ramjet chamber acoustic mode. These fluctuations are supported by non-linear amplification of the fundamental mode, which is enhanced by the thermo-acoustic coupling. We conclude that the increased thermo-acoustic interaction causes the no-cavity case not to support stable combustion in the experiments and a reduced value of the chamber pressure in the computations.

Acknowledgments

The authors are grateful for the support of the Office of Naval Research and Program Officer Dr. Eric Marineau under Grant No. N00014-21-1-2299 and the support of Program Officer Dr. Chad Stoltz under Grant No. N00014-20-1-2316.

References

[1] Avery, W., "Twenty-Five Years of Ramjet Development," *Jet Propulsion*, 1955, pp. 604–614.

[2] Zvuloni, R., Levy, Y., and Gany, A., "Investigation of a Small Solid Fuel Ramjet Combustor," *Journal of Propulsion and Power*, Vol. 5, No. 3, 1989, pp. 269–275. https://doi.org/10.2514/3.23148.

[3] Zvuloni, R., Gany, A., and Levy, Y., "Geometric Effects on the Combustion in Solid Fuel Ramjets," *Journal of Propulsion and Power*, Vol. 5, No. 1, 1989, pp. 32–37. https://doi.org/10.2514/3.23111.

[4] Netzer, A., and Gany, A., "Burning and Flameholding Characteristics of a Miniature Solid Fuel Ramjet Combustor," *Journal of Propulsion and Power*, Vol. 7, No. 3, 1991, pp. 357–363. https://doi.org/10.2514/3.23334.

[5] Gallegos, D., and Young, G., "Utilizing Unique Fuel Geometries to Increase Performance in Solid Fuel Ramjets," *AIAA Scitech 2022 Forum*, 2022, p. 2363.

[6] Gallegos, D., Pace, H., Arnold, C., Massa, L., and Young, G., "Regression and Flame Structure in Flameholding Solid Fuel Ramjet Fuel Grains," *Journal of Propulsion and Power (under consideration)*, 2022.

[7] Chauhan, M., and Massa, L., "LES of supersonic jet-noise with discontinuous Galerkin method," *AIAA Journal*, in press.

[8] Marxman, G., and Gilbert, M., "Turbulent Boundary Layer Combustion in the Hybrid Rocket," *Symposium (International) on Combustion*, Vol. 9, 1963, pp. 371–383.

[9] Gany, A., "Accomplishments and Challenges in Solid Fuel Ramjets and Scramjets," *International Journal of Energetic Materials and Chemical Propulsion*, 2009, pp. 421–446.

[10] Lautenberger, C., and Fernandez-Pello, A., "Pyrolysis modeling, thermal decomposition, and transport processes in combustible solids," *Transport phenomena in fires*, Vol. 20, 2008, p. 209.

[11] De Wilde, J., "The heat of gasification of polyethylene and polymethylmethacrylate," *Delft University of Technology, Faculty of Aerospace Engineering, memorandum m-593*, 1988.

[12] Geipel, C. M., Bojko, B. T., Pfützner, C. J., Fisher, B. T., and Johnson, R. F., "Regression of solid polymer fuel strands in opposed-flow combustion with gaseous oxidizer," *Proceedings of the Combustion Institute*, 2022.

[13] Seshadri, K., and Williams, F. A., "Structure and extinction of counterflow diffusion flames above condensed fuels: Comparison between poly(methyl methacrylate) and its liquid monomer, both burning in nitrogen–air mixtures," *Journal of Polymer Science: Polymer Chemistry Edition*, Vol. 16, No. 7, 1978, pp. 1755–1778. https://doi.org/https://doi.org/10.1002/pol.1978.170160726.

[14] Nardozzo, P. K., Connell Jr., T. L., Boyer, J. E., Yetter, R. A., and Young, G., "Diffusion Flame Studies of Solid Fuels with Nitrous Oxide," *International Journal of Energetic Materials and Chemical Propulsion*, Vol. 19, 2020, pp. 73–93.

[15] Young, G., Hromisin, S., Loeffler, S., and Connell, T., "Effect of Oxidizer Type on Solid Fuel Combustion," *Journal of Propulsion and Power*, Vol. 36, 2020, pp. 248–255.

[16] Densmore, J., Biss, M., McNesby, K., and Homan, B., "High-Speed Digital Color Imaging Pyrometry," *Applied Optics*, 2011, pp. 2659–2665.

[17] Dakshnamurthy, S., Knyazkov, D. A., Dmitriev, A. M., Korobeinichev, O. P., Nilsson, E. J., Konnov, A. A., and Narayanaswamy, K., "Experimental study and a short kinetic model for high-temperature oxidation of methyl methacrylate," *Combustion Science and Technology*, Vol. 191, No. 10, 2019, pp. 1789–1814.

[18] Goodwin, D. G., Moffat, H. K., and Speth, R. L., "Cantera: An Object-oriented Software Toolkit for Chemical Kinetics, Thermodynamics, and Transport Processes," http://www.cantera.org, 2017. https://doi.org/10.5281/zenodo.170284, version 2.3.0.

[19] Sun, W., Zhao, Q., Curran, H. J., Deng, F., Zhao, N., Zheng, H., Kang, S., Zhou, X., Kang, Y., Deng, Y., et al., "Further insights into the core mechanism of H2/CO/NOx reaction system," *Combustion and Flame*, Vol. 245, 2022, p. 112308.

[20] Seshadri, K., and Williams, F., "Structure and extinction of counterflow diffusion flames above condensed fuels: comparison between poly (methyl methacrylate) and its liquid monomer, both burning in nitrogen–air mixtures," *Journal of Polymer Science: Polymer Chemistry Edition*, Vol. 16, No. 7, 1978, pp. 1755–1778.

[21] Ali, U., Karim, K. J. B. A., and Buang, N. A., "A review of the properties and applications of poly (methyl methacrylate)(PMMA)," *Polymer Reviews*, Vol. 55, No. 4, 2015, pp. 678–705.

[22] Arisawa, H., and Brill, T., "Kinetics and mechanisms of flash pyrolysis of poly (methyl methacrylate)(PMMA)," *Combustion and Flame*, Vol. 109, No. 3, 1997, pp. 415–426.

[23] Beckstead, M. W., Puduppakkam, K., Thakre, P., and Yang, V., "Modeling of combustion and ignition of solid-propellant ingredients," *Progress in Energy and Combustion Science*, Vol. 33, 2007, pp. 497–551.

[24] McAlevy III, R. F., Lee, S. Y., and Smith, W. H., "Linear pyrolysis of polymethylmethacrylate during combustion." *AIAA Journal*, Vol. 6, No. 6, 1968, pp. 1137–1142.

[25] Korobeinichev, O., Paletsky, A., Gonchikzhapov, M., Glaznev, R., Gerasimov, I., Naganovsky, Y., Shundrina, I., Snegirev, A. Y., and Vinu, R., "Kinetics of thermal decomposition of PMMA at different heating rates and in a wide temperature range," *Thermochimica Acta*, Vol. 671, 2019, pp. 17–25.

[26] Steinhaus, T., "Evaluation of the thermophysical properties of poly (methylmethacrylate): a reference material for the development of a flammability test for micro-gravity environments," Ph.D. thesis, The University of Maryland, 1999.

[27] Brockhaus, V. A., and Jenckel, E., "Über die kinetik des thermischen abbaues von polymethacrylsäuremethylester." *Die Makromolekulare Chemie: Macromolecular Chemistry and Physics*, Vol. 18, No. 1, 1956, pp. 262–293.

[28] Rende, D., Schadler, L. S., and Ozisik, R., "Controlling Foam Morphology of Poly(methyl methacrylate) via Surface Chemistry and Concentration of Silica Nanoparticles and Supercritical Carbon Dioxide Process Parameters," *Journal of Chemistry*, Vol. 2013, 2013. Article ID 864926.

[29] de León J, M., V, B., and MA, R.-P., "Nanocellular Polymers: The Challenge of Creating Cells in the Nanoscale," *Materials (Basel)*, Vol. 12(5), 2019, p. 797.

[30] Wanga, G., Zhaob, J., Wang, G., Mark, L. H., Park, C. B., and Zhao, G., "Low-density and Structure-tunable Microcellular PMMA Foams with Improved Thermal-insulation and Compressive Mechanical Properties," *European Polymer Journal*, Vol. 95, 2017, pp. 382–393.

[31] Economon, M., Palacios, F., Copeland, S. R., Lukaczyk, T., and Alonso, J. J., "SU2: An Open-Source Suite for Multiphysics Simulation and Design," *AIAA Journal*, Vol. 54, No. 3, 2016, pp. 828–846.

[32] Johnson, R. F., and Kercher, A. D., "A conservative discontinuous Galerkin discretization for the chemically reacting Navier-Stokes equations," *Journal of Computational Physics*, Vol. 423, 2020, p. 109826.

[33] Pierce, C. D., and Moin, P., "Progress-variable approach for large-eddy simulation of non-premixed turbulent combustion," *Journal of Fluid Mechanics*, Vol. 504, 2004, pp. 73–97.

[34] Poinsot, T., and Veynante, D., *Theoretical and numerical combustion*, RT Edwards, Inc., 2005.

[35] Bilger, R., "A note on Favre averaging in variable density flows," *Combustion Science and Technology*, Vol. 11, No. 5-6, 1975, pp. 215–217.

[36] Bilger, R., Stårner, S., and Kee, R., "On reduced mechanisms for methane-air combustion in nonpremixed flames," *Combustion and Flame*, Vol. 80, No. 2, 1990, pp. 135–149.

[37] Pierce, C. D., and Moin, P., "A dynamic model for subgrid-scale variance and dissipation rate of a conserved scalar," *Physics of Fluids*, Vol. 10, No. 12, 1998, pp. 3041–3044.

[38] Nguyen, T. M., and Sirignano, W. A., "Spontaneous and triggered longitudinal combustion instability in a single-injector liquid-rocket combustor," *AIAA Journal*, Vol. 57, No. 12, 2019, pp. 5351–5364.

[39] Kee, R. J., Coltrin, M. E., and Glarborg, P., *Chemically reacting flow: theory and practice*, John Wiley & Sons, 2005.

[40] Chen, M., Buckmaster, J., Jackson, T., and Massa, L., "Homogenization Issues and the Combustion of Heterogeneous Solid Propellants," *Proceedings of the Combustion Institute*, Vol. 29, No. 2, 2002, pp. 2923–2929. https://doi.org/10.1016/S1540-7489(02)80357-1.

[41] Domino, S., Moen, C., Burns, S., and Evans, G., "SIERRA/Fuego: A multi-mechanics fire environment simulation tool," *41st Aerospace Sciences Meeting and Exhibit*, 2003, p. 149.

[42] Hubbard, J. A., Hansen, M. A., Kirsch, J. R., Hewson, J. C., and Domino, S. P., "Medium-Scale Methanol Pool Fire Model Validation," *Journal of Heat Transfer*, Vol. 144, No. 6, 2022, p. 061303.

[43] Beckstead, M. W., Puduppakkam, K., Thakre, P., and Yang, V., "Modeling of combustion and ignition of solid-propellant ingredients," *Progress in Energy and Combustion Science*, Vol. 33, No. 6, 2007, pp. 497–551.

[44] Pace, H., "Analysis of Acoustic Modes in Solid Fuel Ramjet Cavities," *Bulletin of the American Physical Society*, 2022.

[45] Geuzaine, C., and Remacle, J.-F., "Gmsh: A 3-D finite element mesh generator with built-in pre-and post-processing facilities," *International journal for numerical methods in engineering*, Vol. 79, No. 11, 2009, pp. 1309–1331.

[46] Schmidt, O. T., and Colonius, T., "Guide to spectral proper orthogonal decomposition," *AIAA Journal*, Vol. 58, No. 3, 2020, pp. 1023–1033.

[47] Ihme, M., and See, Y. C., "Prediction of autoignition in a lifted methane/air flame using an unsteady flamelet/progress variable model," *Combustion and Flame*, Vol. 157, No. 10, 2010, pp. 1850–1862.

Chapter 6

Three-dimensional Effects in Solid Fuel Ramjets

6.1 Introduction

Three dimensional effects can be important in solid fuel ramjets when the injector convective Mach number is large enough to support rotating instability waves. The resulting azimuthal modes can support changes of the mixing rate at the shear layer when compared to the axisymmetric flow that was analyzed in the previous chapters. Analyzing the contribution of azimuthal modes can lead to the improved design of non-circular ramjet cavity geometries that can further strengthen the flame-holding capability of the non-standard ramjet combustion chambers analyzed here.

In order to analyze three-dimensional effect I have extended the LES code to three-dimensions. Because of the large number of basis coefficients in the discontinuous Galerkin formulation, the performance of the parallel solver is paramount. The large amount of work performed by the reactive LES in the table-look up routines deteriorates the scaling because such computations are replicated over the ghost (not owned) elements. A sectioning strategy was developed where the grid is separated in connected lists of similar elements that are processed together, thus taking advantage of neighboring points having similar characteristics.

6.2 Scaling

Parallel scaling was investigated on Tinkecliffs, the flagship HPC computer at Virginia Tech at the time this research was conducted. Tinkecliffs features 42,000 cores and over 93 TB of RAM; the nodes chips are 128-cores Cray AMD EPYC 7702 and have a boost frequency of 3.35 GHz. Parallel performance are degraded when full nodes are used, because of the particular internal structure of the nodes. The present test is performed on a grid with 17.27×10^6 degrees of freedom (i.e., the number of the coefficients of the discontinuous Galerkin basis) and was advanced of a time of 10^{-7} seconds with a constant $\Delta T = 10^{-9}$ seconds, which corresponds to a CFL number of 1/10 on the hot simulations. The computations discussed in the modal analysis described in the following sections have been performed with a higher CFL, approximately 0.4 for both reactive and unreactive cases. Scaling results are presented in Figure 6.1, which shows an almost linear scaling when full nodes are used (top row) and the number of cores varies as $P = 128 \times N$ with the number of nodes N. On the other hand using just a fraction of a node can significantly improve performance and the scaling in the bottom row $P <= 128$ is highly non-linear. Moreover, the connected list strategy used in this work appears to support a good scaling for the new LES combustion algorithm (i.e., reactive) I have developed. Finally, notice that the ratio of reactive to non-reactive clock times is approximately 3.5, which is acceptable given the much more complex set of equations used by the reactive analysis.

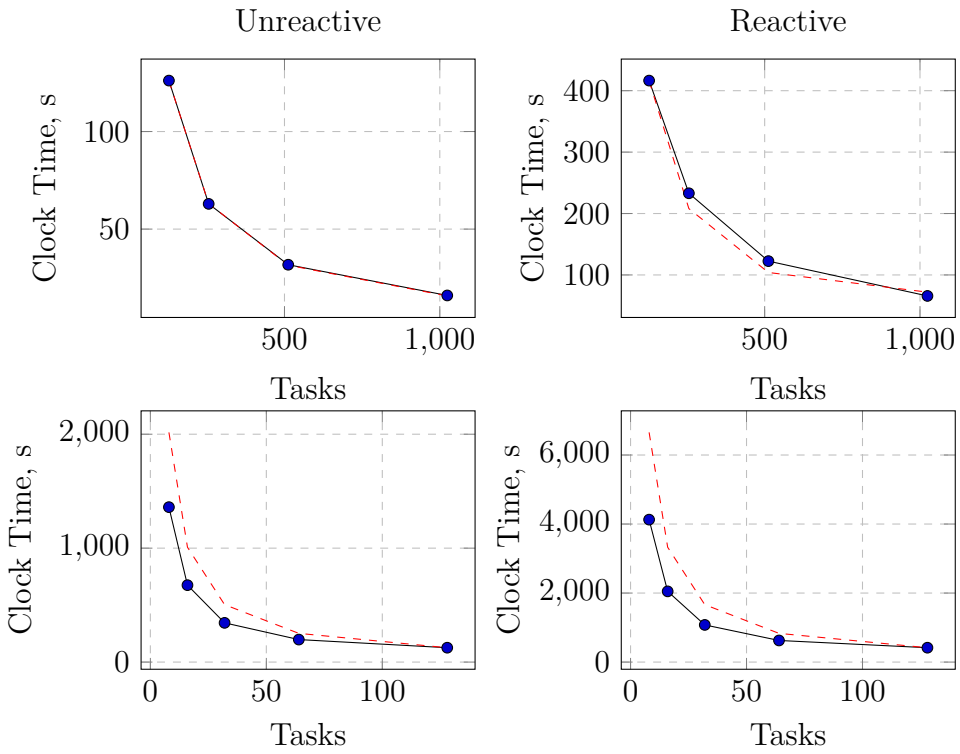

Figure 6.1: Parallel Scaling. Legend: — Actual; - - - Expected.

6.3 Geometry and Grid

Two different pieces of software were used for the purpose of generating grids for the simulations performed in this thesis. The most extensively used software was Gmsh, which is an open-source grid generation program. Gmsh provided the useful ability to interface with code through a Python API, which allowed the reliable generation of unstructured 2D and 3D grids. One example 2D unstructured grid is depicted in Figure 6.2, where it can be seen that the grid grows progressively more refined near the walls. Gmsh also provided the ability to elevate the polynomial order of the finite element grid, which for continuous regions of flow can considerably increase detail for a given number of elements. The significance of solution order is discussed earlier in this thesis in section 4.1.1. Further details on the 2D

grids are discussed at the start of the Results and Discussion section of the earlier attached paper "Acoustics in Flameholding Solid Fuel Ramjet Fuel Grains," and will not be repeated here. One alternative program used for grid generation was Fidelity Pointwise, which is a commercial software. Pointwise, while unable to produce higher-order elements, allowed for the generation of hybrid structured-unstructured grids in a more reliable manner than Gmsh. This feature which was particularly useful for later 3D hot flow simulations which required a well-refined boundary layer to determine behavior near the fuel grain walls and benefited from the use of structured boundary layer elements when calculating heat flux. A grid generated in Pointwise can be seen in Figure 6.3 and example 3D momentum results are shown in Figure 6.4.

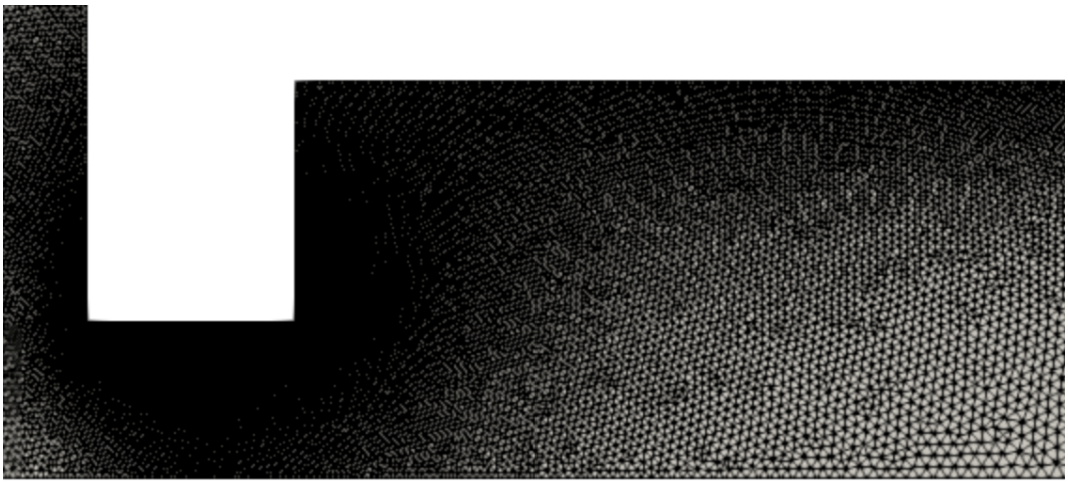

Figure 6.2: Closeup of injector of early 2D grid

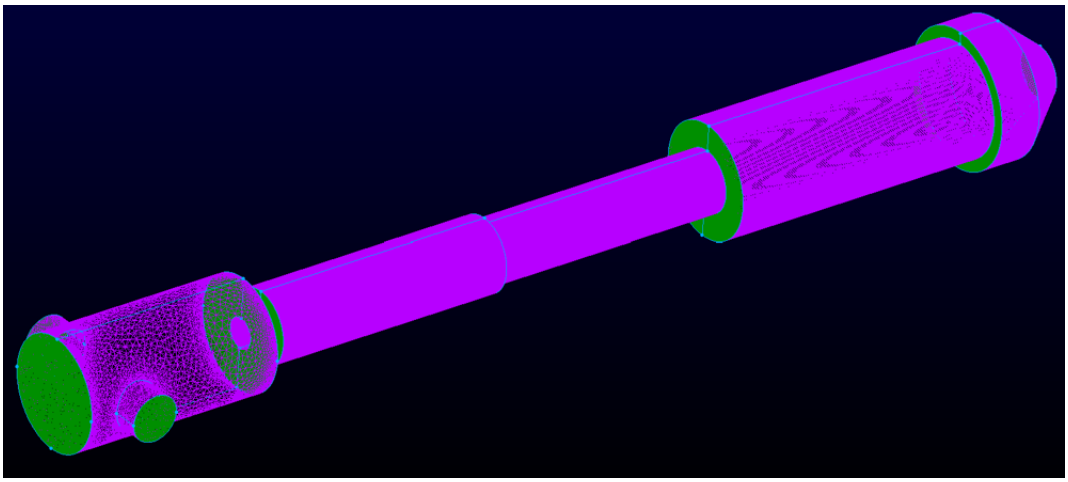

Figure 6.3: 3D grid generated with Pointwise

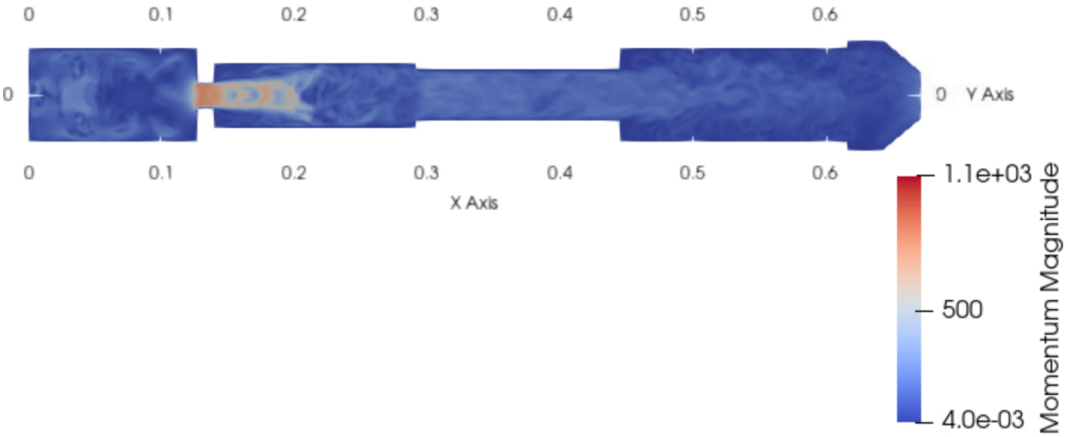

Figure 6.4: Ramjet Cavity

6.4 Turbulent Kinetic Energy Spectra

In turbulent flows, there is a cascade of energy from large scales in which inertial forces dominate down to the very small Kolmogorov microscales where viscosity dominates and the turbulent kinetic energy of eddies is transformed into thermal energy. In-between these two extremes there is a range of scales significantly affected by both inertial and viscous forces,

termed the Inertial Sub-range. For a LES computation to be accurate, it should resolve the flow down into this inertial sub-range. This can be checked by observing spectra of the Turbulent Kinetic Energy (TKE), a quantity which can be defined as

$$TKE = \frac{1}{2}\sqrt{\overline{(u')^2} + \overline{(v')^2} + \overline{(w')^2}} \tag{6.1}$$

where "′" denotes that these refer to the fluctuating components of velocity and the bars denote a time-averaging operation. In the inertial sub-range, the energy has been empirically found to follow a -5/3 power law with respect to wavenumber, therefore if the TKE spectra from LES data appears to follow this power law, it is a good indication the simulation has adequate resolution. TKE spectra from different probe points within the cold flow simulations can be seen below in figures 6.5 and 6.6. As can be seen, the spectra approximately follow the expected -5/3 power law (linear in log scale) above 400 Hz. Similar spectra within the hot flow simulations are depicted in 6.7 and 6.8. The hot flow spectra appear to follow the expected slope between approximately 300 Hz and 5000 Hz, but above this frequency appear to lose energy. This decrease in the TKE specra at high frequency/wavenumber in the reacting flows may be due to increased viscosity at high temperature, however further investigation is required. The location labelled as 0.571 m corresponds to the pressure probe used in the experiment, while the location labelled as 0.2 m corresponds to a point the cavity for the 6-inch cavity geometry. It may be noted that for the hot flow, the spectrum at the 0.5714 m probe position follows slightly closer to the -5/3 power law than that at the 0.2 m position. Present analysis indicates this is due the development of turbulence as the flow moves down the length of the ramjet.

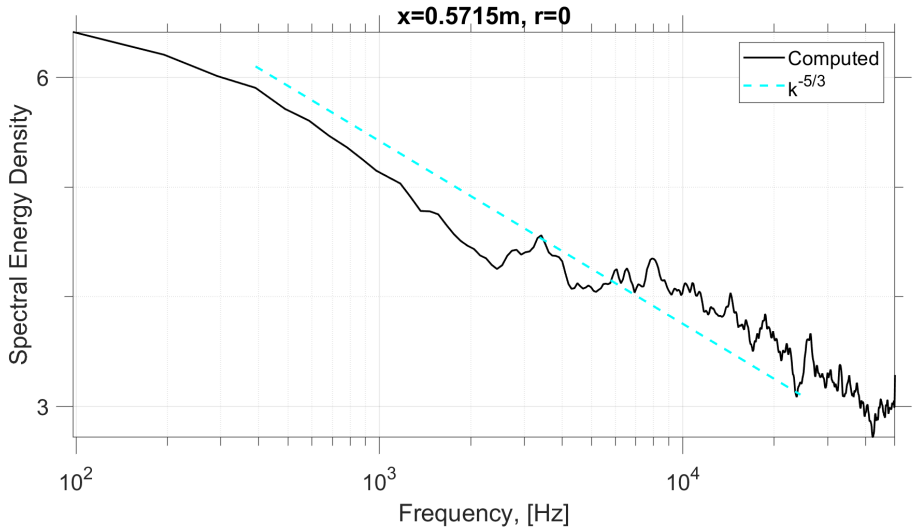

Figure 6.5: Cold Flow TKE Spectrum

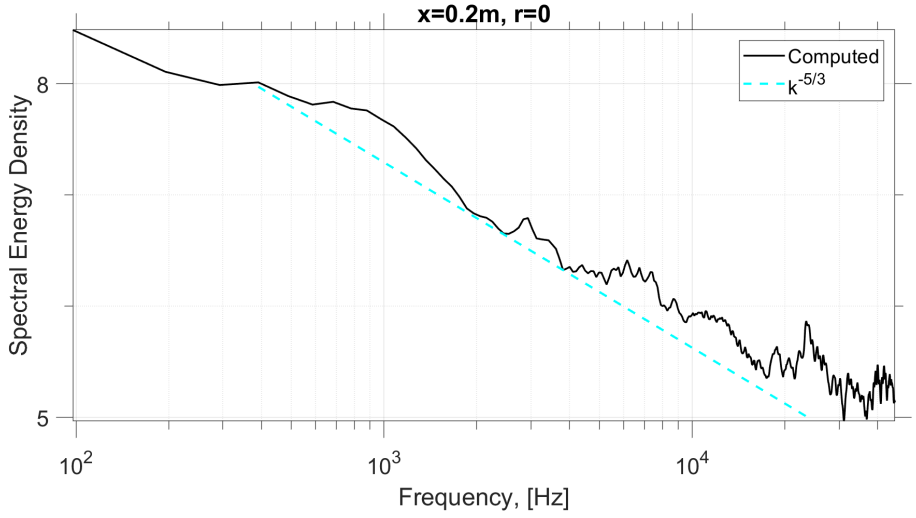

Figure 6.6: Cold Flow TKE Spectrum

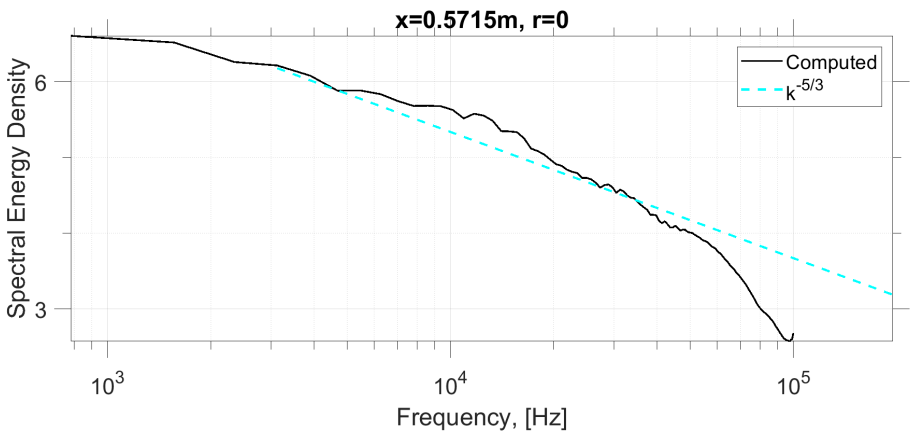

Figure 6.7: Hot Flow TKE Spectrum

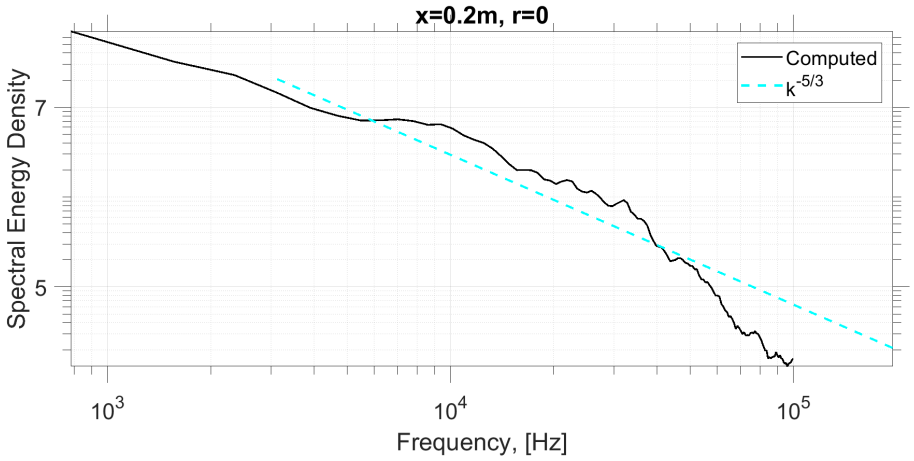

Figure 6.8: Hot Flow TKE Spectrum

6.5 Modal Analysis

Snapshots of the mixture fraction from the hot flow analysis are shown in Figures 6.9 and 6.10 with longitudinal and cross sectional view of the field. It can be noticed the thin layer of fuel next to the walls that leads to estimating flame stand-off distance of the order of one millimeter. The hot flow simulations differently from the cold flow ones show no azimuthal modes and the azimuthal variation of the mixture fraction profile is very weak. Also the

top and bottom of Figure 6.9 appear very symmetrical. This confirms the idea that the shear layer is not affected by rotating instability waves when the convective Mach number is strongly decreased by combustion and pressurization in the chamber.

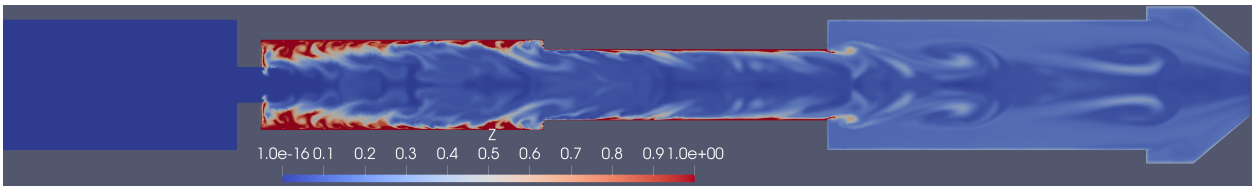

Figure 6.9: Three-Dimensional simulation of the 152-mm Ramjet cavity with reactive flow: mixture fraction field on a plane parallel to the axis.

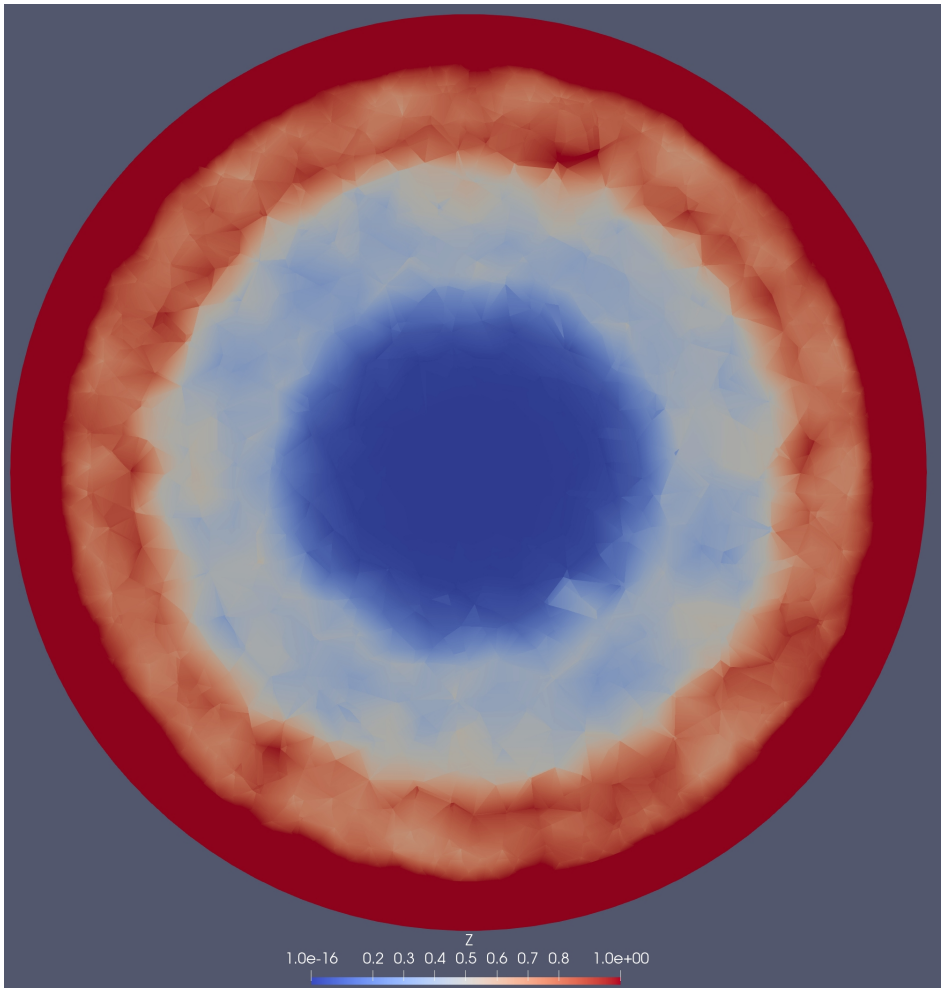

Figure 6.10: Three-Dimensional simulation of the 152-mm Ramjet cavity with reactive flow, $x = 0.25$ m.

Chapter 7

Future Work

This section describes work in progress that was not completed as part of this Master thesis and will be included in forthcoming presentations and paper submissions. We have performed and exploratory investigation into dynamic calibration of the turbulent Schmidt number, anisotropic mesh adaptation, and hybrid-order grids for Discontinous Galerkin formulations.

7.1 Schmidt Number Effects

As noted earlier, the simulations used to produce the results in this thesis used a constant Schmidt number $\bar{\rho}D_t = \mu_t/Sc_t$, $Sc_t = 1$. This simple turbulent Schmidt number was selected as it is common assumption in other studies of compressible turbulent flow [23][24]. It is sometimes argued that a dynamic Germano's procedure can represent the variability of the Sc_t in turbulent combustion, but this assumption has not been proven to be reliable in the literature [25]. In the present research the contribution of the turbulent Schmidt number is modest because the eddy viscosity is small at the wall and the heat released by the diffusion flame is strongest in the near-wall region. Future research will focus on implementations of the Germano's identity to determine the value of the Turbulent Schmidt number by matching the filtered equations with various filter size.

7.2 Anisotropic Adaptive Grids

Future work sill also include the use of pyAMG, an Adaptive Mesh Generation suite developed by Inria for use with SU2 using a Python wrapper. This software allows the anisotropic refinement of existing elements in regions of high gradient, such shocks, walls, and shear layers. Anisotropic grid refinement could allow for a 100-fold improvement in the computation time for a given level of accuracy (include citation). This grid type would also make it easier to include the sideport inlets while maintaining a well-refined boundary layer [26].

7.3 Hybrid Order Grids and Solutions

Further future work may include the use of hybrid-order grids, as found in hp-FEM. During work with the ramjet, the author found there to be a strong trade-off between stability with lower-order schemes and accuracy with higher-order schemes. Hybrid-order grids would allow the use of low-order elements in high-gradient regions such as where shocks are present and high-order elements in other regions where variables behave more smoothly. [27]

Chapter 8

Conclusion

The principal conclusion of my thesis work is that high-order discontinuous Galerkin methods coupled with flamelet mandifold combustion approximations allow for the resolution of thermoacoustic coupling supported by large complex chemical mechanism with over 600 reactions and complex melt layer conditions at the solid boundaries. This high-fidelity Navier-Stokes solver can be used to optimize the design of fuel grain cavities and thus maximize flameholding and minimize the acoustic feedback in ramjets. The investigations of the resulting combustion and acoustic fields supported by solid fuel ramjet have led me to the validation of the proposed numerical approach and new findings on the physics of kinetics-acoustic interactions.

The validation study compares the combustion of PMMA under laminar counter-flow conditions to a numerical model of combustion for a self-similar stagnation flow. The numerical model includes a melting foam layer model for the PMMA that allows fuel evaporation and decomposition through the presence of bubbles observed experimentally. This decomposition prior to the fuel reaching the oxidizer hastens the regression process. The simulations were able to accurately predict the fuel regression rates, and it was found that the model predicts the maximum flame temperature with reasonable agreement. The simulations predict accurately the effects of mass flux on flame standoff distance and to a lesser extent the extinction rates. The combustion and foam model demonstrated high fidelity in comparison to experimental work whereas latent heat solid model (without foam) failed to capture the

significance of the diffusion flame in a counterflow burner with a stagnation point very close to one of the inlets. The comparison of experiments and computations identifies the effect of momentum transfer between bubble and condensed phases on the burning rate using a simple argument. The melt layer contributes to combustion by increasing residence time of the gas in the thermal wave, which accelerates the thermal decomposition of the PMMA fuel. The melt layer thickness is of the same order as the flame stand off distance and decreases with the heat flux while being substantially unaffected by changes of pressure.

The introduction of a cavity flameholder into solid fuel ramjet fuel grains improved the flameholding limits of the combustor by creating a recirculation region that allows sustained combustion at increased fuel loading. Presented regression patterns demonstrate that the presence of the cavity flameholder affects the reattachment points downstream location and location of maximum regression. The analysis revealed that the average regression rate in the port region of the fuel grain was seen to have significantly higher regression than that of the cavity. Despite insensitivity to changes in combustion efficiency, chamber pressure was observed to increase with increasing cavity length. Increasing the cavity length to half the length of a representative center perforated grain allows a higher in chamber pressure above that which would be seen with the center perforated fuel grain.

Numerical investigations of the flameholding fuel grains demonstrated that the introduction of a cavity flame holder increased the heat feedback in the recirculation region and contributed to global hydrodynamic instabilities in the combustor. Calculated regression patterns agree well with experimental results and the resulting computed heat flux support the conclusion of increased heat transfer as the dominant mechanism of increased flameholding.

The combustion model developed in one dimension was applied to the prediction of cavity acoustics in an axisymmetric model of a solid-fueled ramjet with stationary burning walls.

Cold-flow LES simulations show that there are two dominant acoustic modes ($St \equiv f/f_0 = \{3, 18\}$) in the ramjet and their frequencies appear to be invariant with respect to the cavity configuration. The first peak corresponds to a longitudinal mode associated to the chamber fundamental oscillations (with length scale L_c). The second is characterized with radial fluctuations in the mixing chamber and features the maximum chamber radius of the ramjet as its scaling length. Mixed (radial and axial) modes in the intermediate frequency range reveal the effect of a slanted aft wall on the acoustics. Three-dimensional cold flow simulations predicted weak non-symmetric (azimuthal) modes.

Hot-flow simulations show a substantial increase in the mean chamber pressure with the addition of the cavity, indicating that it enhances flame-holding in solid-fuel ramjets, in agreement with the experiments. The analysis of the ramjet acoustic modes shows the emergence of low frequency modes in the cavity cases, in agreement with the experiments. Using SPOD, these modes were seen to be associated with low-frequency breathing of the recirculation region at the nozzle throat. Perturbations are localized in the throat region because of the Mach number pressure scaling. These modes do not appear to affect the pressure fluctuations and thus combustion in the chamber. Together with the emergence of low-frequency vortical modes, the cavity supports a decrease in the high-wave number harmonics of the ramjet chamber acoustic mode. These fluctuations are supported by nonlinear amplification of the fundamental mode resulting from thermoacoustic coupling. We conclude that the increased thermoacoustic interaction causes the no-cavity case not to support stable combustion in the experiments and result in a reduced value of chamber pressure in the computations.

Appendices

Appendix A

MATLAB Codes

Azimuthal Fast Fourier Transform code

```
%Script written by Charles Arnold to perform azimuthal fast fourier transform
    on Ramjet

%Clear workspace

function out = ramjet_AFFT_fun(root, type)

%*************************************************************************
%
if ~exist('type','var') || isempty(type)
    type = 'hot';
end

%Scaling factors
bar = 1e5;
pscale = 4.7*bar; %Scale pressure by total pressure

if strcmp(type,'hot')
    folderpath = ['~/SU2_B/RAMJETII_',root];
    dateStart='12-Sep-2022';
    fnames = 'restart*0.csv';
    isCSV = 1;
```

```
22 else
23     folderpath = ['/projects/scramjetcombustion/SU2_MASTER/TestCases/CAVITY/',
           root,'/rev2'];
24     %All Charles' files are good
25     dateStart='1-Jan-2021';
26     fnames = '*restart_flow*.dat';
27     isCSV = 0; %Adjusted to account for having re-output vtu files into csv
           files from paraview
28 end
29
30 T0=548.0; %Total temp at inlet (K)
31 gamma = 7/5; %ratio spec heats
32 R = 287.052874247; %Spec gas constant for air (J/kg-K)
33 a0 = sqrt(gamma*R*T0); %Speed of sound at inlet conds (m/s)
34 L = 0.53; %Ramjet cavity length
35 f_spod=a0/2/L;
36
37 %Frequency, time, and grid settings
38 %tbnds_spod = [0.001,0.1];
39 grid_x = linspace(0,0.67192324664412,round(811));
40 grid_y = linspace(1e-6,0.042164,round(51));
41
42 [spod_X,spod_Y] = meshgrid(spod_x,spod_y);
43 spod_grid.x = spod_X;
44 spod_grid.y = spod_Y;
45
46 tdata_filepath = 'tdata.mat'; %time vs. iteration file data path
47 load_tdata = false;
48 vid_filepath = root; %filepath for video of frames
49
50 %parameters of the SPOD solver
```

```
opts.savefft    = true;             % save FFT blocks insteasd of keeping them
    in memory
opts.deletefft  = false;            % keep FFT blocks in this example for
    demonstration purposes
opts.savedir    = ['ramjetResults_',root];        % save results to '
    ramjetResults_v1' folder in the current directory
opts.savefreqs  = [2,3,4,5];          % save modes frequencies of indices [10
    15 20]
opts.nsave      = 3;                % save the 3 most energetic modes

DT = 1 / f_spod/(2*(max(opts.savefreqs)-1));%time interval between
    interpolated snapshots
nDFT=1/(DT*f_spod);

%%%%%%%%%%%%%%%%%%%%%%%%%%%%%%%%%%%%%%%%%%%%%%%%%%%%%%%%%%%%%%%%%%%%%%%%%%%%

allFiles = dir([folderpath '/',fnames]);
thedates = arrayfun(@(x) datetime(x.date), allFiles);
recent = allFiles(thedates >= datetime(dateStart));
datFiles = recent;
nDat = length(datFiles);
datFilenames = {datFiles.name}';
if isCSV
    iterMatches = regexp(datFilenames,'(?<=_)\d+(?=\.csv)','match');
else
    iterMatches = regexp(datFilenames,'(?<=_)\d+(?=\.dat)','match');
end
iter = uint32(str2double([iterMatches{:}])); %Iter across all dat files
[iter,isrt]=sort(iter);
datFiles = datFiles(isrt);
steady_mask = iter > uint32(500); %Get rid of transient
```

```
77 iter = iter(steady_mask);
78 datFiles = datFiles(steady_mask);
79 datFilenames = {datFiles.name}';
80 datFilepaths = strcat({datFiles.folder}', '/', datFilenames); %paths to .dat
       files
81 h=regexp(fileread([folderpath,'/','LES_NS_CF.cfg']), 'TIME_STEP *= *(?<delt>\w
       *\.*\w+)','names');delt=str2num(h.delt);
82 % myPat = strjoin([iterMatches{:}],'|') ')\|\s+[^\.\|]+(?=\|) '];
83 %time = double(iter-iter(1))*double(delt);
84 %tbnds_spod = [tbnds_spod(1),time(end)];
85 %tbnds_spod(2) = tbnds_spod(1) + floor((tbnds_spod(2)-tbnds_spod(1))/DT)*DT;
86 %t_spod = tbnds_spod(1):DT:tbnds_spod(2);
87 %opts.nt = length(t_spod);
88
89 mask = getMask2(spod_grid);
90 %allFrames = loadAll2(spod_grid,datFilepaths,'Pressure',0);
91
92 %Charles to implement the paprallel code you should replace the
93 %loadAll3CSV call with the 4 lines below
94 nw=16;
95 [mch,kpts,ipts,Ppts,myPool] = parallelSetup(datFilepaths,nw, [],[],[], [], [],
       1);
96 mn = zeros(mch,1);
97 parfor (jth=1:mch,nw)
98     %if (isCSV)
99     %     Ppts{jth} = loadAll3CSV(spod_grid, kpts{jth}, 'Pressure', mask) /
           pscale;
100    %else
101    %     Ppts{jth} = loadAll3(spod_grid, kpts{jth}, 'Pressure', mask) / pscale
           ;
102    %end
```

```
103     %mn = mean(Ppts{jth},'all');
104     T = loadData(kpts{jth};
105
106 end
107 %mn = mean(mn,'all');
108 %parfor (jth=1:mch,nw)
109 %     Ppts{jth} = Ppts{jth} - mn;
110 %end
111 [~,~,~,~,~,allFrames] = parallelSetup([],[], mch,kpts,ipts, Ppts,myPool, 2);
112 %allFrames = loadAll3CSV(spod_grid, datFilepaths, 'Pressure', mask, isCSV) /
        pscale;
113
114 nanAndZeros = nan(size(mask));
115 nanAndZeros(mask) = 0;
116 maskfun = @(Frame) Frame + nanAndZeros;
117
118 %xfun = @(i) squeeze(interp1(time,allFrames,t_spod(i),'linear'));
119
120 %opts.mean = squeeze(mean(allFrames,1));
121 %figure;surf(spod_grid.x,spod_grid.y,opts.mean)
122 %set(gca,'FontSize',16);
123 %set(gca,'FontSize',16);
124
125 xfun = @(i) squeeze(interp1(time,allFrames,t_spod(i),'linear'));
126
127 opts.mean = squeeze(mean(allFrames,1));
128 %if doMovie
129 %     v = VideoWriter(vid_filepath);
130 %     open(v);
131 %     for k = 1:numel(t_spod)
132 %         disp(["doing frame (%):",num2str(k/numel(t_spod)*100)])
```

```
133 %           clf;cla
134 %           surf(spod_grid.x,spod_grid.y,maskfun(xfun(k) - opts.mean))
135 %           caxis([-0.1,0.1]);
136 %           view(2);shading flat;axis image
137 %           frame = getframe(gcf);
138 %           writeVideo(v,frame);
139 %       end
140 %       close(v);
141 %end
142
143 %xfun = @(i) getRamjetFrame(t_spod(i),spod_grid,time,datFilepaths,'Pressure');
144
145 %[L,P,F] = spodlm(xfun,nDFT,[],[],DT,opts);
146 %
147 %figure
148 %count = 0;
149 %MI=1:1;
150 %nrows=numel(opts.savefreqs)*numel(MI);
151 %for fi = opts.savefreqs
152 %       for mi = MI
153 %           count = count + 1;
154 %           subplot(nrows,1,count)
155 %           get(gca,'Position')
156 %           out=P(fi,mi);
157 %           contourf(spod_grid.x,spod_grid.y,maskfun(real(squeeze(out))),11,'
        edgecolor','none'),
158 %          %axis equal tight, caxis(max(abs(caxis))*[-1 1]);
159 %           axis equal tight, caxis('auto');
160 %           if count < nrows
161 %               set(gca,'XTick',[]);
162 %           else
```

```
163 %             xlabel('x (m)');
164 %         end
165 %         ylabel('r'), title(['f=' num2str(F(fi),'%.2f') 'Hz, mode ' num2str(mi
    ) ', \lambda=' num2str(L(fi,mi),'%.2g')])
166 %         %xlim([0 10]); ylim([0 2])
167 %     end
168 %end
169 %print (gcf,'-dpng', ['cavityModes',root,'.png']);
170 %out = gcf;
171
172 end
173
174 %%%%%%%%%%%%%%%%%%%%%%%%%%%%%%%%%%%%%%%%%%%%%%%%%%%%%%%%%%%%%%%%%%%%%%%%%%%
175
176 function time = fixTime(time) %#ok<DEFNU>
177     nanMask = isnan(time);
178     if (sum(nanMask) > 0.1*length(time))
179         error('unwrapTSV: > 10% of time values are NaN!');
180     end
181
182     %Fix NaN values
183     N = 3;
184
185     if (nanMask(1))
186         time(1) = 0;
187     else
188         time = time-time(1);
189     end
190     nt = length(time);
191     indNextNaN = find(isnan(time),1,'first');
192     while (~isempty(indNextNaN))
```

```
193         indNextNonNaN = find(~isnan(time(indNextNaN:nt)),1,'first') +
                indNextNaN-1;
194         if (isempty(indNextNonNaN))
195             dt = mean(time((indNextNaN-N):(indNextNaN-1))); %FIX
196             time(indNextNaN:nt) = time(indNextNan-1) + dt*1:(nt-indNextNaN-1);
197         elseif (indNextNonNaN == nt)
198             time(indNextNaN:nt) = linspace(time(indNextNaN-1),time(
                    indNextNonNaN),2+indNextNonNaN-indNextNan);
199         else
200             testTime = linspace(time(indNextNaN-1),time(indNextNonNaN),2+
                    indNextNonNaN-indNextNan); %#ok<NASGU>
201         end
202     end
203 end
204
205 function time = unwrapTime(time)
206     time = time-time(1);
207     nt = length(time);
208     for i = 3:nt
209         if (time(i) <= time(i-1))
210             if (time(i) == 0 || i == nt)
211                 time(i:nt) = time(i:nt) + time(i-1) + (time(i-1)-time(i-2));
212             else
213                 time(i:nt) = (time(i:nt)-time(i)) + time(i-1) + (time(i+1)-
                        time(i));
214             end
215         end
216     end
217 end
218
219 function interpolateData(outputFilepath, inputFilepath, timeIterData, options)
```

```
    %#ok<INUSL,DEFNU>
220     if (~exist('options','var'))
221         options = struct();
222     end
223     if (~isfield(options, 'timeInterpMethod') || ~any(options.timeInterpMethod
        ,{'linear','nearest'}))
224         options.timeInterpMethod = 'linear';
225     end
226     if (~isfield(options, 'spaceInterpMethod') || ~any(options.
        spaceInterpMethod,{'linear','nearest'}))
227         options.spaceInterpMethod = 'linear';
228     end
229     if (~isfield(options,'targetGrid'))
230         generateTargetGrid = true;
231     else
232         if (~isfield(options.targetGrid))
233             %
234         else
235             %
236         end
237         if (~isfield(options.targetGrid))
238             %
239         else
240             %
241         end
242     end
243
244 end
245
246 function simFrame = getRamjetFrame(tq,gridq,time,datFilepaths,variable)
247     if (tq == time(1)) %First sample time, no temporal interpolation needed
```

```
248         T = readData(datFilepaths{1});
249         Var_unstruct = T.(variable);
250     else %Any other time, use linear temporal interpolation
251         iFs_lo = sum(time < tq);
252         c_hi = (tq - time(iFs_lo)) / (time(iFs_lo+1)-time(iFs_lo));
253         c_lo = 1 - c_hi;
254 
255         T = readData(datFilepaths{iFs_lo});
256         Var_unstruct = (T.(variable))*c_lo;
257         T = readData(datFilepaths{iFs_hi});
258         Var_unstruct = Var_unstruct + (T.(variable))*c_hi;
259     end
260 
261     if (isfield(gridq,'z'))
262         F = scatteredInterpolant(T.x,T.y,T.z,Var_unstruct,'ExtrapolationMethod
                ','none');
263         simFrame = F(gridq.x,gridq.y,gridq.z);
264     else
265         F = scatteredInterpolant(T.x,T.y,Var_unstruct,'ExtrapolationMethod','
                none');
266         simFrame = F(gridq.x,gridq.y);
267     end
268 
269     nanMask = isnan(simFrame);
270     simFrame(nanMask) = mean(simFrame(~nanMask),'all');
271 end
272 
273 %Temporary function simplification, just gets mean value over last dat file
274 function varMean = getRamjetFrameMean(datFilepaths,variable)
275     varMean = mean(readData(datFilepaths{end}).(variable),'all');
276     t = 1; %just here for debug
```

```
277 end
```

Spectral Proper Orthogonal Decomposition code

Appendix B

C++ Codes

Code snippet in DG Euler Solver for calculation of inviscid fluxes (supplementary to viscous fluxes in NS solver) with flamelet variables.

```
1    case 3: {
2
3      /* Three dimensional simulation. Loop over the number of faces treated
4      simultaneously. */
5      for(unsigned short l=0; l<nFaceSimul; ++l) {
6
7        /* Easier storage for some variables of this face. */
8        const su2double *normals   = normalsFace[l];
9        const su2double *gridVels  = gridVelsFace[l];
10       const unsigned short lNVar = l*nVar;
11
12       /* Loop over the number of points for this face. */
13       for(unsigned long i=0; i<nPoints; ++i) {
14
15         /* Easier storage of the left and right solution, the face normals,
16         the grid velocities and the flux vector for this point. */
17         const unsigned long offPointer = i*NPad + lNVar;
18         unsigned long iScalWork = l*nPoints + i;
19
20         const su2double *UL      = solL + offPointer;
21         const su2double *UR      = solR + offPointer;
```

```
22            const su2double *norm    = normals + i*(nDim+1);
23            const su2double *gridVel = gridVels + i*nDim;
24            su2double       *flux    = fluxes + offPointer;
25
26            const su2double *scalarsL = UL + nVarF;
27            const su2double *scalarsR = UR + nVarF;
28
29            const su2double nx = norm[0], ny = norm[1], nz = norm[2], halfArea =
                  0.5*norm[3];
30
31            /* Compute the normal grid velocity. */
32            const su2double gridVelNorm = gridVel[0]*nx + gridVel[1]*ny +
                 gridVel[2]*nz;
33
34            /*--- Compute the primitive variables of the left and right state.
                 ---*/
35            const su2double invRhoL = 1.0/UL[0];
36            const su2double vxL = invRhoL*UL[1];
37            const su2double vyL = invRhoL*UL[2];
38            const su2double vzL = invRhoL*UL[3];
39
40            const su2double invRhoR = 1.0/UR[0];
41            const su2double vxR = invRhoR*UR[1];
42            const su2double vyR = invRhoR*UR[2];
43            const su2double vzR = invRhoR*UR[3];
44
45            /*--- Compute the difference of the conservative mean flow variables
                 . ---*/
46            const su2double dr  = UR[0] - UL[0];
47            const su2double dru = UR[1] - UL[1];
48            const su2double drv = UR[2] - UL[2];
```

```
49            const su2double drw = UR[3] - UL[3];
50            const su2double drE = UR[4] - UL[4];
51
52            /*--- Compute the Roe average state. ---*/
53            const su2double zL = sqrt(UL[0]);
54            const su2double zR = sqrt(UR[0]);
55            const su2double zI= 1.0/(zL + zR);
56
57            pL= UL[3] - 0.5*(vxL*UL[1] + vyL*UL[2] + vzL*UL[3]); // internal
                  energy density rho eint
58            pR= UR[3] - 0.5*(vxR*UR[1] + vyR*UR[2] + vzR*UR[3]);
59            if(!flamelet) {
60              pL*=gm1;
61              pR*=gm1;
62              rHL = UL[3] + pL;
63              rHR = UR[3] + pR;
64              gm1Z = gm1;
65            }
66            else {
67              if(computeWorkArrays) {
68                pL=pLVec[iScalWork];
69                pR=pRVec[iScalWork];
70                rHL = UL[nDim+1] + pL;
71                rHR = UR[nDim+1] + pR;
72                gm1L = a2LVec[iScalWork]*UL[0]/pL -1.0;
73                gm1R = a2RVec[iScalWork]*UR[0]/pR -1.0;
74                gm1Z =gm1Roe[iScalWork];//max(gm1LVec[iScalWork], gm1RVec[
                      iScalWork]);
75                gm1 = min(gm1L, gm1R);
76              }
77              else {
```

```
78              rHL = UL[0];//density
79              rHR = UR[0];
80              pL/=rHL;//specific internal energy
81              pR/=rHR;
82              tie(gm1, gm1Z) =getLeftRightPressureEnthalpy(pL,rHL,scalarsL, pR
                    ,rHR,scalarsR,  &pL,&rHL,&a2L, &pR,&rHR,&a2R);
83            }
84            rHL+= 0.5*(vxL*UL[1] + vyL*UL[2] + vzL*UL[3]);//+= rho u^2
85            rHR+= 0.5*(vxR*UR[1] + vyR*UR[2] + vzR*UR[3]);
86          }
87
88          const su2double drE_pg = rHR - rHL - pR + pL;
89
90          const su2double uAvg = zI*(zL*vxL + zR*vxR);
91          const su2double vAvg = zI*(zL*vyL + zR*vyR);
92          const su2double wAvg = zI*(zL*vzL + zR*vzR);
93          const su2double HAvg = zI*(rHL/zL + rHR/zR);
94
95          /*--- Compute from the Roe average state some variables, which occur
96            quite often in the matrix vector product to be computed. ---*/
97          const su2double alphaAvg = 0.5*(uAvg*uAvg + vAvg*vAvg + wAvg*wAvg);
98          su2double tmp            = gm1*(HAvg - alphaAvg);
99          const su2double a2Avg    = fabs(tmp);
100         const su2double aAvg     = sqrt(a2Avg);
101         const su2double vnAvg    = uAvg*nx + vAvg*ny + wAvg*nz;
102         const su2double unAvg    = vnAvg - gridVelNorm;
103         const su2double ovaAvg   = 1.0/aAvg;
104         const su2double ova2Avg  = 1.0/a2Avg;
105
106         /*--- Compute the absolute values of the three eigenvalues and
107           apply the entropy correction. ---*/
```

```
108           su2double lam1 = fabs(unAvg + aAvg);
109           su2double lam2 = fabs(unAvg - aAvg);
110           su2double lam3 = fabs(unAvg);
111
112           tmp  = Delta*max(lam1, lam2);
113           lam1 = max(lam1, tmp);
114           lam2 = max(lam2, tmp);
115           lam3 = max(lam3, tmp);
116
117           /*--- Some abbreviations, which occur quite often in the dissipation
                  terms. ---*/
118           const su2double abv1 = 0.5*(lam1 + lam2);
119           const su2double abv2 = 0.5*(lam1 - lam2);
120           const su2double abv3 = abv1 - lam3;
121
122           const su2double abv4 = gm1Z*(alphaAvg*dr - uAvg*dru - vAvg*drv -wAvg
                 *drw + drE_pg);
123           const su2double abv5 = nx*dru + ny*drv + nz*drw - vnAvg*dr;
124           const su2double abv6 = abv3*abv4*ova2Avg + abv2*abv5*ovaAvg;
125           const su2double abv7 = abv2*abv4*ovaAvg  + abv3*abv5;
126
127           /*--- Compute the Roe flux vector, which is 0.5*(FL + FR - |A|(UR-UL
                 )). ---*/
128           const su2double vnL = vxL*nx + vyL*ny + vzL*nz;
129           const su2double vnR = vxR*nx + vyR*ny + vzR*nz;
130           const su2double unL = vnL - gridVelNorm;
131           const su2double unR = vnR - gridVelNorm;
132           const su2double pa  = pL + pR;
133
134           flux[0] = halfArea*(UL[0]*unL + UR[0]*unR - (lam3*dr + abv6));
135           flux[1] = halfArea*(UL[1]*unL + UR[1]*unR + pa*nx
```

```
136             -            (lam3*dru + uAvg*abv6 + nx*abv7));
137           flux[2] = halfArea*(UL[2]*unL + UR[2]*unR + pa*ny
138             -            (lam3*drv + vAvg*abv6 + ny*abv7));
139           flux[3] = halfArea*(UL[3]*unL + UR[3]*unR + pa*nz
140             -            (lam3*drw + wAvg*abv6 + nz*abv7));
141           flux[4] = halfArea*(UL[4]*unL + UR[4]*unR + pL*vnL + pR*vnR
142             -            (lam3*drE + HAvg*abv6 + vnAvg*abv7));
143
144           //add scalar fluxes
145           if(flamelet)
146             for(unsigned short izz=nVarF; izz<nVarC; ++izz) {
147               const su2double ZL = UL[izz]/UL[0];
148               const su2double ZR = UR[izz]/UR[0];
149               su2double ZAvg =zI*(zL*ZL + zR*ZR);
150               const su2double drZ = UR[izz] - UL[izz];
151               const double dissZ= -(a2Avg*(abv1 - abv3)*drZ + abv3*gm1Z*(
                      alphaAvg*dr + drE_pg - dru*uAvg - drv*vAvg - drw*wAvg)*ZAvg
                      + aAvg*abv2*(dru*nx + drv*ny + drw*nz - dr*vnAvg)*ZAvg)/
                      a2Avg;
152               flux[izz] = halfArea*(UL[izz]*unL + UR[izz]*unR + dissZ);
153             }
154             for(unsigned short izz=nVarC; izz<nVar; ++izz) flux[izz] =  0.0;
155         }//for(unsigned long i=0; i<nPoints; ++i)
156       }//for(unsigned short l=0; l<nFaceSimul; ++l)
157
158       break;
159     }
```

Code snippet in DG Navier Stokes Solver for calculation of viscous fluxes with flamelet variables.

```
1     case 3: {
2
3         /* 3D simulation. Loop over the chunk of elements and loop over the
4            integration points of the elements to compute the fluxes. */
5         for(unsigned short ll=0; ll<llEnd; ++ll) {
6           const unsigned short llNVar = ll*nVar;
7           const unsigned long  lInd   = l + ll;
8
9           for(unsigned short i=0; i<nInt; ++i) {
10            const unsigned short iNPad = i*NPad;
11
12            /* Easier storage of the metric terms and grid velocities in this
13               integration point and compute the inverse of the Jacobian. */
14            const su2double *metricTerms = volElem[lInd].metricTerms.data()
15                                         + i*nMetricPerPoint;
16            const su2double *gridVel     = volElem[lInd].gridVelocities.data()
                  + i*nDim;
17            const su2double Jac          = metricTerms[0];
18            const su2double JacInv       = 1.0/Jac;
19
20            /* Compute the true metric terms in this integration point. */
21            const su2double drdx = JacInv*metricTerms[1];
22            const su2double drdy = JacInv*metricTerms[2];
23            const su2double drdz = JacInv*metricTerms[3];
24
25            const su2double dsdx = JacInv*metricTerms[4];
26            const su2double dsdy = JacInv*metricTerms[5];
27            const su2double dsdz = JacInv*metricTerms[6];
28
29            const su2double dtdx = JacInv*metricTerms[7];
30            const su2double dtdy = JacInv*metricTerms[8];
```

```
31            const su2double dtdz = JacInv*metricTerms[9];
32
33            /* Compute the metric terms multiplied by minus the integration
                 weight.
34               The minus sign comes from the integration by parts in the weak
35               formulation. */
36            const su2double wDrdx = -weights[i]*metricTerms[1];
37            const su2double wDrdy = -weights[i]*metricTerms[2];
38            const su2double wDrdz = -weights[i]*metricTerms[3];
39
40            const su2double wDsdx = -weights[i]*metricTerms[4];
41            const su2double wDsdy = -weights[i]*metricTerms[5];
42            const su2double wDsdz = -weights[i]*metricTerms[6];
43
44            const su2double wDtdx = -weights[i]*metricTerms[7];
45            const su2double wDtdy = -weights[i]*metricTerms[8];
46            const su2double wDtdz = -weights[i]*metricTerms[9];
47
48            /* Easier storage of the location where the solution data of this
49               integration point starts. */
50            const su2double *sol    = solAndGradInt + iNPad + llNVar;
51            const su2double *dSolDr = sol    + offDeriv;
52            const su2double *dSolDs = dSolDr + offDeriv;
53            const su2double *dSolDt = dSolDs + offDeriv;
54            const su2double *scalars = sol + nVarF;
55            const su2double *dScalarsDr = dSolDr + nVarF;
56            const su2double *dScalarsDs = dSolDs + nVarF;
57            const su2double *dScalarsDt = dSolDt + nVarF;
58
59            /*--- Compute the Cartesian gradients of the independent solution
60                  variables from the gradients in parametric coordinates and
```

```
                the
61              metric terms in this integration point. ---*/
62          const su2double dRhoDx  = dSolDr[0]*drdx + dSolDs[0]*dsdx + dSolDt
                [0]*dtdx;
63          const su2double dRhoUDx = dSolDr[1]*drdx + dSolDs[1]*dsdx + dSolDt
                [1]*dtdx;
64          const su2double dRhoVDx = dSolDr[2]*drdx + dSolDs[2]*dsdx + dSolDt
                [2]*dtdx;
65          const su2double dRhoWDx = dSolDr[3]*drdx + dSolDs[3]*dsdx + dSolDt
                [3]*dtdx;
66          const su2double dTempDx = dSolDr[J]*drdx + dSolDs[J]*dsdx + dSolDt
                [J]*dtdx;
67
68          const su2double dRhoDy  = dSolDr[0]*drdy + dSolDs[0]*dsdy + dSolDt
                [0]*dtdy;
69          const su2double dRhoUDy = dSolDr[1]*drdy + dSolDs[1]*dsdy + dSolDt
                [1]*dtdy;
70          const su2double dRhoVDy = dSolDr[2]*drdy + dSolDs[2]*dsdy + dSolDt
                [2]*dtdy;
71          const su2double dRhoWDy = dSolDr[3]*drdy + dSolDs[3]*dsdy + dSolDt
                [3]*dtdy;
72          const su2double dTempDy = dSolDr[J]*drdy + dSolDs[J]*dsdy + dSolDt
                [J]*dtdy;
73
74          const su2double dRhoDz  = dSolDr[0]*drdz + dSolDs[0]*dsdz + dSolDt
                [0]*dtdz;
75          const su2double dRhoUDz = dSolDr[1]*drdz + dSolDs[1]*dsdz + dSolDt
                [1]*dtdz;
76          const su2double dRhoVDz = dSolDr[2]*drdz + dSolDs[2]*dsdz + dSolDt
                [2]*dtdz;
77          const su2double dRhoWDz = dSolDr[3]*drdz + dSolDs[3]*dsdz + dSolDt
```

```
                [3]*dtdz;
78              const su2double dTempDz = dSolDr[J]*drdz + dSolDs[J]*dsdz + dSolDt
                    [J]*dtdz;
79
80              /*--- Compute the velocities and static energy in this integration
                     point. ---*/
81              const su2double rhoInv       = 1.0/sol[0];
82              const su2double u            = sol[1]*rhoInv;
83              const su2double v            = sol[2]*rhoInv;
84              const su2double w            = sol[3]*rhoInv;
85              const su2double TotalEnergy  = sol[4]*rhoInv;
86              const su2double StaticEnergy = TotalEnergy - 0.5*(u*u + v*v + w*w)
                    ;
87
88              /*--- Compute the Cartesian gradients of the velocities and static
                     energy
89                in this integration point and also the divergence of the
                         velocity. ---*/
90              const su2double dudx = rhoInv*(dRhoUDx - u*dRhoDx);
91              const su2double dudy = rhoInv*(dRhoUDy - u*dRhoDy);
92              const su2double dudz = rhoInv*(dRhoUDz - u*dRhoDz);
93
94              const su2double dvdx = rhoInv*(dRhoVDx - v*dRhoDx);
95              const su2double dvdy = rhoInv*(dRhoVDy - v*dRhoDy);
96              const su2double dvdz = rhoInv*(dRhoVDz - v*dRhoDz);
97
98              const su2double dwdx = rhoInv*(dRhoWDx - w*dRhoDx);
99              const su2double dwdy = rhoInv*(dRhoWDy - w*dRhoDy);
100             const su2double dwdz = rhoInv*(dRhoWDz - w*dRhoDz);
101
102             const su2double divVel = dudx + dvdy + dwdz;
```

```
103
104             /*--- If an SGS model is used the eddy viscosity must be computed.
                    ---*/
105             su2double ViscosityTurb = 0.0;
106             if( SGSModelUsed ) {
107               const su2double lenScale = volElem[lInd].lenScale/nPoly;
108               ViscosityTurb = SGSModel->ComputeEddyViscosity_3D(sol[0], dudx,
                      dudy, dudz, dvdx, dvdy, dvdz, dwdx, dwdy, dwdz, lenScale,
                      volElem[lInd].wallDistance[i]);
109             }
110
111             unsigned long iScalWork = ll*nInt + i;
112             /* Set TDstate and fetch properties of the fluid*/
113             //assuming has scalars,
114             //FluidModel->SetTDState_rhoe(sol[0], StaticEnergy, scalars, true,
                    true);// Volume_Residual
115             //const su2double Pressure = FluidModel->GetPressure();
116             //const su2double Temperature = FluidModel->GetTemperature();
117             //su2double ViscosityLam = FluidModel->GetLaminarViscosity();
118             //if(flameletActive) rhoDkHkSumVec = FluidModel->GetSumRhoDkHk();
119             su2double Pressure     = pVec    [iScalWork];
120             su2double Temperature  = TVec    [iScalWork];
121             su2double energySourceZ= eZVec   [iScalWork];
122             su2double energySourceP= ePVec   [iScalWork];
123             su2double ViscosityLam = muVec   [iScalWork];
124             su2double ConductivityLam=condVec[iScalWork];
125             su2double CP           = cpVec[iScalWork];
126             su2double rhoDlam = VdVec[iScalWork];
127             for(unsigned short iz=0; iz<nScal; ++iz) rhoDkHkSumVec[iz] =
                    scalarWorkArrays[index_rhoDkHkSumVec+iz][iScalWork];
128             for(unsigned short iz=0; iz<nScal; ++iz) DviscosityVec[iz] =
```

```
            scalarWorkArrays[index_DviscosityVec+iz][iScalWork];//
            derivaitve of the viscosity wrt to the scalars
129
130         su2double *source = sources + iNPad + llNVar;
131         std::fill_n(source, nVar, 0.0);
132
133         //Progress source
134         su2double *sourceF = source + nVarF; //Pointer to array of sources
             for scalars
135         for(unsigned short iz=0; iz<nSrc; ++iz) sourceF[iz+1] = max(min(
            sol[0],5.0),1e-1)*sources_aux[iz][iScalWork];
136         //if(sources_aux[0][iScalWork] > 1e3) cout << Zmx[iScalWork] << "
            in NS " << sources_aux[0][iScalWork] << sourceF[1] << endl;
137
138         //if(Zpr[iScalWork] > 0.98 || scalars[1]/sol[0] > 1000) sourceF[1]
             = copysign(sourceF[1],-1.0);
139
140         //weigh and bring to LHS
141         const su2double weightJac = weights[i]*Jac;
142         for (unsigned short iScalar = 0; iScalar < nScal; ++iScalar)
            sourceF[iScalar] = -sourceF[iScalar]*weightJac;
143         source[nDim+1] = -max(min(sol[0],2.5),1e-2)*energySourceP*
            weightJac;
144         //source[nDim+1] = -energySourceP*weightJac;
145
146         //LM_AOE6114_2022Proj
147         ViscosityLam += volElem[lInd].shockArtificialViscosity; //Add the
            ArtificialViscosity
148
149         /* Compute the total viscosity and heat conductivity. Note that
            the heat
```

```
150             conductivity is divided by the Cv, because gradients of
                    internal energy
151             are computed and not temperature. */
152           const su2double Viscosity = ViscosityLam + ViscosityTurb;
153           const su2double Conductivity = ConductivityLam + CP*ViscosityTurb*
                  factHeatFlux_Turb;
154
155           /*--- Set the value of the second viscosity and compute the
                  divergence
156                term in the viscous normal stresses. ---*/
157           const su2double lambda     = -TWO3*Viscosity;
158           const su2double lamDivTerm =  lambda*divVel;
159
160           /*--- Compute the viscous stress tensor and minus the heatflux
                  vector. ---*/
161           const su2double tauxx = 2.0*Viscosity*dudx + lamDivTerm;
162           const su2double tauyy = 2.0*Viscosity*dvdy + lamDivTerm;
163           const su2double tauzz = 2.0*Viscosity*dwdz + lamDivTerm;
164
165           const su2double tauxy = Viscosity*(dudy + dvdx);
166           const su2double tauxz = Viscosity*(dudz + dwdx);
167           const su2double tauyz = Viscosity*(dvdz + dwdy);
168
169           const su2double qx = Conductivity*dTempDx;
170           const su2double qy = Conductivity*dTempDy;
171           const su2double qz = Conductivity*dTempDz;
172
173           /* Compute the relative velocities w.r.t. the grid. */
174           const su2double uRel = u - gridVel[0];
175           const su2double vRel = v - gridVel[1];
176           const su2double wRel = w - gridVel[2];
```

```
177
178             /* Compute the viscous normal stress minus the pressure. */
179             const su2double tauxxMP = tauxx - Pressure;
180             const su2double tauyyMP = tauyy - Pressure;
181             const su2double tauzzMP = tauzz - Pressure;
182
183             /* Set the pointer for the fluxes in this integration point. */
184             su2double *flux = fluxes + nDim*iNPad + llNVar;
185             vector<su2double*> fluxE; // the energy flux that must be
                    corrrected for the species derivatives
186
187             /*--- Fluxes in r-direction. */
188             su2double *fluxFr = flux + nVarF;
189             fluxE.push_back(flux+nDim+1);
190             const su2double Ur = uRel*wDrdx + vRel*wDrdy + wRel*wDrdz;
191
192             flux[0] = sol[0]*Ur;
193             flux[1] = sol[1]*Ur - tauxxMP*wDrdx - tauxy*wDrdy - tauxz*wDrdz;
194             flux[2] = sol[2]*Ur - tauxy*wDrdx - tauyyMP*wDrdy - tauyz*wDrdz;
195             flux[3] = sol[3]*Ur - tauxz*wDrdx - tauyz*wDrdy - tauzzMP*wDrdz;
196             flux[4] = sol[4]*Ur - (u*tauxxMP + v*tauxy + w*tauxz + qx)*wDrdx
197                                 - (u*tauxy + v*tauyyMP + w*tauyz + qy)*wDrdy
198                                 - (u*tauxz + v*tauyz + w*tauzzMP + qz)*wDrdz;
199
200             /*--- Fluxes in s-direction. */
201             flux = flux + NPad;
202             su2double* fluxFs = flux + nVarF; //CAedit
203             fluxE.push_back(flux+nDim+1);
204             const su2double Us = uRel*wDsdx + vRel*wDsdy + wRel*wDsdz;
205
206             flux[0] = sol[0]*Us;
```

```
207             flux[1] = sol[1]*Us - tauxxMP*wDsdx - tauxy*wDsdy - tauxz*wDsdz;
208             flux[2] = sol[2]*Us - tauxy*wDsdx - tauyyMP*wDsdy - tauyz*wDsdz;
209             flux[3] = sol[3]*Us - tauxz*wDsdx - tauyz*wDsdy - tauzzMP*wDsdz;
210             flux[4] = sol[4]*Us - (u*tauxxMP + v*tauxy + w*tauxz + qx)*wDsdx
211                                 - (u*tauxy + v*tauyyMP + w*tauyz + qy)*wDsdy
212                                 - (u*tauxz + v*tauyz + w*tauzzMP + qz)*wDsdz;
213
214             /*--- Fluxes in t-direction. */
215             flux = flux + NPad;
216             su2double* fluxFt = flux + nVarF;
217             fluxE.push_back(flux+nDim+1);
218             const su2double Ut = uRel*wDtdx + vRel*wDtdy + wRel*wDtdz;
219
220             flux[0] = sol[0]*Ut;
221             flux[1] = sol[1]*Ut - tauxxMP*wDtdx - tauxy*wDtdy - tauxz*wDtdz;
222             flux[2] = sol[2]*Ut - tauxy*wDtdx - tauyyMP*wDtdy - tauyz*wDtdz;
223             flux[3] = sol[3]*Ut - tauxz*wDtdx - tauyz*wDtdy - tauzzMP*wDtdz;
224             flux[4] = sol[4]*Ut - (u*tauxxMP + v*tauxy + w*tauxz + qx)*wDtdx
225                                 - (u*tauxy + v*tauyyMP + w*tauyz + qy)*wDtdy
226                                 - (u*tauxz + v*tauyz + w*tauzzMP + qz)*wDtdz;
227
228             //CAedit
229             const su2double rhoDturb = ViscosityTurb*SchmidtTurbInv;
230             const su2double rhoDtot = max(rhoDlam,0.0) + rhoDturb;
231
232             for(unsigned short iz=0; iz<nScal; ++iz) rhoDkHkSumVec[iz] *=
                    rhoDlam*rhoInv;
233
234             su2double rhoDsrc = rhoDtot;
235
236             /*--- Calculate scalar fluxes ---*/ //CAedit start
```

```
237             su2double dScalarDx, dScalarDy, dScalarDz;
238             su2double dViscLamdx = 0;
239             su2double dViscLamdy = 0;
240             su2double dViscLamdz = 0;
241             for (unsigned short iScalar = 0; iScalar < nScal; ++iScalar) {
242
243               dScalarDx = dScalarsDr[iScalar] * drdx + dScalarsDs[iScalar] *
                      dsdx + dScalarsDt[iScalar]*dtdx;
244               dScalarDy = dScalarsDr[iScalar] * drdy + dScalarsDs[iScalar] *
                      dsdy + dScalarsDt[iScalar]*dtdy;
245               dScalarDz = dScalarsDr[iScalar] * drdz + dScalarsDs[iScalar] *
                      dsdz + dScalarsDt[iScalar]*dtdz;
246
247               //LMadd: scalars are actually rho*scalars, sorry for the
                      confusion
248               const su2double scalar_rho = scalars[iScalar] * rhoInv;
249               dScalarDx = rhoInv * (dScalarDx - scalar_rho * dRhoDx);
250               dScalarDy = rhoInv * (dScalarDy - scalar_rho * dRhoDy);
251               dScalarDz = rhoInv * (dScalarDz - scalar_rho * dRhoDz);
252
253               gradScalar[iScalar * nDim] = dScalarDx;
254               gradScalar[iScalar * nDim + 1] = dScalarDy;
255               gradScalar[iScalar * nDim + 2] = dScalarDy;
256
257               su2double drTerm = dScalarDx * wDrdx + dScalarDy * wDrdy +
                      dScalarDz*wDrdz;
258               su2double dsTerm = dScalarDx * wDsdx + dScalarDy * wDsdy +
                      dScalarDz*wDsdz;
259               su2double dtTerm = dScalarDx * wDtdx + dScalarDy * wDtdy +
                      dScalarDz*wDtdz;
260
```

```
261             /*--- fluxes in r-direction. ---*/
262             fluxFr[iScalar] = scalars[iScalar] * Ur - rhoDtot * drTerm;
263             *(fluxE[0]) -= rhoDkHkSumVec[iScalar] * drTerm;//add to the
                    energy flux
264
265             /*--- Fluxes in s-direction. ---*/
266             fluxFs[iScalar] = scalars[iScalar] * Us - rhoDtot * dsTerm;
267             *(fluxE[1]) -= rhoDkHkSumVec[iScalar] * dsTerm;//add to the
                    energy flux
268
269             /*--- Fluxes in t-direction. ---*/
270             fluxFt[iScalar] = scalars[iScalar] * Ut - rhoDtot * dtTerm;
271             *(fluxE[2]) -= rhoDkHkSumVec[iScalar] * dtTerm;//add to the
                    energy flux
272         }
273         //Sensible energy Source
274         unsigned short iScalar = 0;
275         source[nDim + 1] -= rhoDsrc * energySourceZ * weightJac * (
                gradScalar[iScalar * nDim] * gradScalar[iScalar * nDim] +
                gradScalar[iScalar * nDim + 1] * gradScalar[iScalar * nDim +
                1] + gradScalar[iScalar * nDim + 2] * gradScalar[iScalar *
                nDim + 2]);
276         //source[nDim + 1] = max(min(source[nDim + 1], 8e11 * weightJac),
                -8e11 * weightJac);
277         //CAedit end
278
279         /*--- If needed, compute the body forces in this integration point
                .
280             Note that the source terms are multiplied with minus the
281             integration weight in order to be consistent with the
282             formulation of the residual. Note that for the energy source
```

```
283                 term the absolute velocity must be taken and not the
284                 relative. ---*/
285             if( body_force ) {
286               su2double *source         = sources + iNPad + llNVar;
287               const su2double weightJac = weights[i]*Jac;
288
289               source[0] =  0.0;
290               source[1] = -weightJac*body_force_vector[0];
291               source[2] = -weightJac*body_force_vector[1];
292               source[3] = -weightJac*body_force_vector[2];
293               source[4] = -weightJac*(u*body_force_vector[0] + v*
                      body_force_vector[1]
294                           +             w*body_force_vector[2]);
295             }
296           }
297         }
298
299         break;
300       }
```

Bibliography

[1] M. Durali, S. Alemohammed, and A. Alasty, "Propulsion control of a solid fuel ramjet using a robust adaptive neural controller," *Proceedings of 2005 IEEE Conference on Control Applications*, pp. 879–884, 2005.

[2] S. Rahskovskii, Y. Milekhin, A. Fedorychev, and S. Yakush, "Mechanism of stabilization of the combustion in the duct of the solid fuel grain of a solid fuel ramjet," *Doklady Physical Chemistry*, vol. 490, pp. 9–13, 2020.

[3] G. Lunkun, C. Xiong, M. Omer, Y. Haitao, and Z. Changsheng, "Numerical and experimental investigation of the effect of geometry on combustion characteristics of solid-fuel ramjet," *Acta Astronautica*, 2017.

[4] O. Musa, X. Chen, Y. Li, W. Li, and W. Liao, "Unsteady simulation of ignition of turbulent reactive swirling flow of novel design of solid-fuel ramjet motor," *energies*, vol. 12, 2019.

[5] S. Kshav, A. Armaan, and S. G, "Material failure analysis and engine combustion instabilities of both air and non-air breathing engines," *Materials Today*, 2020.

[6] L. Tong-Miin, H. Po-Wen, L. Yi-Chen, and C. Chia-Yen, "Flame stability analysis of turbulent non-premixed reacting flow in a simulated solid-fuel ramjet combustor," *Journal of Mechanics*, 2002.

[7] C. Pierce and P. Moin, "Progress-variable approach for large-eddy simulation of non-premixed turbulent combustion," *Journal of Fluid Mechanics*, vol. 504, pp. 73–97, 2004.

[8] S. Moritz, P. Oliver, and O. Kilian, "Spectral proper orthogonal decomposition," *Journal of Fluid Mechanics*, 2016.

[9] L. Weixuan, Z. Dan, Z. Linqing, and C. Xiong, "Proper orthogonal and dynamic mode decomposition analyses of nonlinear combustion instabilities in a solid-fuel ramjet combustor," *Thermal Science and Engineering Progress*, 2022.

[10] D. Gallegos, H. Pace, C. Arnold, L. Massa, and G. Young, "Regression and flame structure in cavity flameholding solid fuel ramjet fuel grains," American Institute of Aeronautics and Astronautics, 2022.

[11] B.-C. Wang and D. Bergstrom, "A general optimal formulation for the dynamic smagorinsky subgrid-scale stress model," *International Journal for Numerical Methods in Fluids*, vol. 49, pp. 1259–1389, 2005.

[12] M. Chauhan and L. Massa, "Les of supersonic jet-noise with discontinuous galerkin method," *AIAA Journal*, 2022.

[13] C. Geuzaine and J.-F. Remacle, "Gmsh: A three-dimensional finite element mesh generator with built-in pre- and post-processing facilities," *International Journal for Numerical Methods in Engineering*, pp. 1309–1331, 2009.

[14] O. Schmidt and T. Colonius, "Guide to spectral proper orthogonal decomposition," *AIAA Journal*, vol. 58, pp. 1–11, 01 2020.

[15] A. Towne, O. T. Schmidt, and T. Colonius, "Spectral proper orthogonal decomposition and its relationship to dynamic mode decomposition and resolvent analysis," *Journal of Fluid Mechanics*, vol. 847, pp. 821–867, 2018.

[16] O. T. Schmidt, A. Towne, G. Rigas, T. Colonius, and G. A. Brès, "Spectral analysis of jet turbulence," *Journal of Fluid Mechanics*, vol. 855, pp. 953–982, 2018.

[17] O. Schmidt, "Spectral proper orthogonal decomposition (spod)." https://github.com/SpectralPOD/spod_matlab. accessed 09/30/2022.

[18] J. A. Hubbard, M. A. Hansen, J. R. Kirsch, J. C. Hewson, and S. P. Domino, "Medium-scale methanol pool fire model validation," *Journal of Heat Transfer*, vol. 144, no. 6, p. 061303, 2022.

[19] D. C. Wilcox *et al.*, *Turbulence modeling for CFD*, vol. 2. DCW industries La Canada, CA, 1998.

[20] M. Germano, U. Piomelli, P. Moin, and W. H. Cabot, "A dynamic subgrid-scale eddy viscosity model," *Physics of Fluids A: Fluid Dynamics*, vol. 3, no. 7, pp. 1760–1765, 1991.

[21] A. Vreman, "An eddy-viscosity subgrid-scale model for turbulent shear flow: Algebraic theory and applications," *Physics of fluids*, vol. 16, no. 10, pp. 3670–3681, 2004.

[22] D. You and P. Moin, "A dynamic global-coefficient subgrid-scale eddy-viscosity model for large-eddy simulation in complex geometries," *Physics of Fluids*, vol. 19, no. 6, p. 065110, 2007.

[23] D. C. Haworth, "Progress in probability density function methods for turbulent reacting flows," *Progress in Energy and combustion Science*, vol. 36, no. 2, pp. 168–259, 2010.

[24] D. Zhou, H. Zhang, and S. Yang, "A robust reacting flow solver with computational diagnostics based on openfoam and cantera," *Aerospace*, vol. 102, no. 9, p. 1, 2022.

[25] V. Sankaran and C. Merkle, "Fundamental physics and model assumptions in turbulent combustion models for aerospace propulsion," in *50th AIAA/ASME/SAE/ASEE Joint Propulsion Conference*, p. 3941, 2014.

[26] F. Alauzet and A. Loseille, "A decade of progress on anisotropic mesh adaptation for computational fluid dynamics," *Computer-Aided Design*, vol. 72, pp. 13–39, 2016.

[27] T. Barth and H. Deconinck, *High Order Methods for Computational Physics*. Springer Berlin, Heidelberg, 1999.

VIRGINIA TECH

Charles Arnold <charlesa18@vt.edu>

Thesis

Dominic Gallegos <dgallegos@vt.edu> Thu, Apr 27, 2023 at 12:10 PM
To: Charles Arnold <charlesa18@vt.edu>
Cc: Luca Massa <lmassa@vt.edu>, "Young, Gregory" <gyoung1199@vt.edu>

Charles,

It is fine with me if you include the journal article material. Congratulations on your defense and best of luck to you moving forward!

Thanks,
Dominic

On Wed, Apr 26, 2023 at 10:50 PM Charles Arnold <charlesa18@vt.edu> wrote:

> Hello Dr. Young and Dominic,
>
> Hope you are doing well. I am preparing to submit my thesis to the grad school after making some edits advised by my committee.
> In its current form, my thesis has attached journal papers I have taken part in writing, with sections of the thesis highlighting and elaborating on the numerical work contained within. Each has citations and recognizes the other authors' work. One of the included papers is the *Regression and Flame Structure in Cavity Flameholding Solid Fuel Ramjet Fuel Grains* article, for which Dominic is lead author.
>
> Dr. Young, as part of my committee, has seen this thesis before and therefore I expect is aware of the inclusion, but I wanted to double check with Dominic, and get a written yes (or no) on whether this is ok before submitting to the Grad School (or making any necessary edits).
>
> Kind Regards,
> Charles Arnold
>
> ---------- Forwarded message ---------
> From: **Charles Arnold** <charlesa18@vt.edu>
> Date: Tue, Apr 25, 2023 at 8:27 PM
> Subject: Re: Thesis
> To: Luca Massa <lmassa@vt.edu>, Young, Gregory <gyoung1199@vt.edu>, Christopher Roy <cjroy@vt.edu>
>
> Hello All,
>
> I have attached a copy of my thesis with revisions made based on your recommendations at the time of my defense. The thesis also has the two co-authored journal papers re-inserted since Brad showed me how to fix my problems with iThenticate.
>
> Kind Regards,
> Charles Arnold
>
> On Wed, Apr 5, 2023 at 12:05 AM Charles Arnold <charlesa18@vt.edu> wrote:
>
> > Hello All,
> >
> > The iThenticate report turned out to be far too large to submit with the online form file size limits, perhaps due to the attached papers that I co-authored earlier being flagged. I have attached it below instead.
> >
> > Kind Regards,

Charles Arnold

On Tue, Apr 4, 2023 at 11:59 PM Charles Arnold <charlesa18@vt.edu> wrote:

Hello All,

I have attached a pdf of my thesis on *Simulation of Flow in a Solid Fuel Ramjet Cavity.*
I am also submitting the online Final Exam (/defense) Request form for the purpose of sending in the iThenticate report to the grad school, although I'm not quite sure whether that form is completely necessary now that the defense date is planned. As far as I can tell, the only real items of note in the iThenticate report are places where I had intentionally attached papers I had authored/co-authored earlier during my research.

Kind Regards,
Charles

On Tue, Apr 4, 2023 at 4:32 PM Charles Arnold <charlesa18@vt.edu> wrote:

Hello All,

I'm not sure who did what exactly, but I was getting ready to call the front office as Dr. Massa recommended when I got an email from Rachel Banks about the thesis defense being scheduled in Randolph Conference Room 207 on Tuesday, April 18th at 3:30pm. Thanks whoever did this, it has saved me some trouble tonight as I finish off the thesis.

Kind Regards,
Charles Arnold

On Tue, Apr 4, 2023 at 4:23 PM Luca Massa <lmassa@vt.edu> wrote:

Hello Charles

I think Randolph Hall will work best for all. Can you ask the front office if any of the RH conference rooms is available?

Thank you

Luca Massa

On Apr 4, 2023, at 4:20 PM, Charles Arnold <charlesa18@vt.edu> wrote:

Hello All,

In relation to Dr. Roy's comment on the thesis defense not yet being formally scheduled with the grad school:
The submission of the thesis is required in the form for scheduling, so I'll be doing this later tonight. To complete this step, we also need to decide what building and room we want to do the defense in. I am fairly flexible on the location, but do any of you have preferences for this?
I apologize for not asking about this back when we had the round of emails for selecting date and time.

Kind Regards,
Charls Arnold

On Tue, Apr 4, 2023 at 3:59 PM Charles Arnold <charlesa18@vt.edu> wrote:

Hello Dr. Roy,

Thanks for alerting me to this. I'll fix that issue as soon as possible.

Kind Regards,
Charles Arnold

On Tue, Apr 4, 2023 at 3:52 PM Christopher Roy <cjroy@vt.edu> wrote:

Charles,

Make sure you formally schedule your thesis defense with the grad school. I don't see it in there yet.

Dr. Roy
==========

Professor Chris Roy
Kevin T. Crofton Department of Aerospace and Ocean Engineering (MC0203)
Randolph Hall, RM 215
Virginia Tech
460 Old Turner St
Blacksburg, VA 24061-0203
Voice: (540) 231-0080
FAX: (540) 231-9632
Email: cjroy@vt.edu
Web: www.aoe.vt.edu/people/faculty/roy.html

On Tue, Apr 4, 2023 at 2:29 PM Charles Arnold <charlesa18@vt.edu> wrote:

> Hello Dr. Young, Dr. Roy, and Dr. Massa,
>
> Hope you all are doing well. I wanted to let you know that my thesis on the Simulation of Flow in a Solid Fuel Ramjet Cavity is almost complete. I intend to send the document to you tonight in preparation for my defense on the 18th. There is a small chance some formatting and final work may delay this until tomorrow morning, but I don't expect this to be an issue.
>
> Kind Regards,
> Charles Arnold

--
Dominic Gallegos
Graduate Student
Virginia Tech: Kevin T. Crofton Aerospace and Ocean Engineering Dept.
PropEL: Propulsion and Energetics Laboratory

VIRGINIA TECH

Charles Arnold <charlesa18@vt.edu>

Journal articles in Thesis

Henry Pace <hrpace42@vt.edu> Fri, Apr 28, 2023 at 11:29 AM
To: Charles Arnold <charlesa18@vt.edu>

Yep, that's totally fine with me. Thanks for checking.

Sincerely,

Henry Pace
Virginia Tech GRA
Tel.: 931-539-5126
Email: hrpace42@vt.edu

From: Charles Arnold
Sent: Friday, April 28, 2023 11:23 AM
To: Henry Pace
Subject: Journal articles in Thesis

Hello Henry,

Hello Henry, hope you're doing well.

I'm getting ready to submit my thesis to the Graduate School. As you might know from our meetings with Dr. Massa, it includes journal articles I have taken part in writing. In particular, it contains "Acoustics in Flameholding Solid Fuel Ramjet Fuel Grains" and "Regression and Flame Structure in Flameholding Solid Fuel Grains," for which you are also an author. I just wanted to check that you are alright with this inclusion?

Kind Regards,

Charles Arnold